MICROSTRUCTURAL EVOLUTION OF SURFACE LAYERS DURING ELECTROLYTIC PLASMA PROCESSING

by

CRISTIAN CIONEA

Presented to the Faculty of the Graduate School of Materials Science and Engineering

The University of Texas at Arlington in Partial Fulfillment

of the Requirements

for the PhD Degree

DOCTOR OF PHILOSOPHY

THE UNIVERSITY OF TEXAS AT ARLINGTON

May 2010

ACKNOWLEDGEMENTS

I would like to express my gratitude to my advisor, Dr. Efstathios I. Meletis, for his support and guidance through the duration of this work. I would also like to thank to Dr. Choong-Un Kim, Dr. Krishnan Rajeshwar, Dr. Jian Yang and Dr. Yaowu. Hao, for serving in my dissertation committee and their constructive questioning. I own a great deal of appreciation Dr. Jiechao Jiang for his help with countless experiments, especially with TEM image analysis. A special thank goes to E.O. Daigle, P. Gupta and P. George from CAP Technologies LLC. for providing most of the samples and experimental process parameters. I appreciate the technical assistance of the colleagues in our group at the Surface and Nano Engineering Laboratory at UTA. Notes of gratitude go to the staff of Materials Science and Engineering Department at UTA. I also am grateful to the personnel of Hitachi in Dallas for the help provided with TEM sample preparation. The support from SERDP is also acknowledged.

April 16, 2010

ABSTRACT

MICROSTRUCTURAL EVOLUTION OF SURFACE LAYERS DURING ELECTROLYTIC PLASMA PROCESSING

Cristian D. Cionea, PhD

The University of Texas at Arlington, 2009

Supervising Professor: Efstathios I. Meletis

Electrolytic Plasma Processing is an emerging technology for surface modification. The EPP process is based on electrolysis of an aqueous electrolyte by application of an electrical potential between the workpiece and counter-electrode, and the production of plasma (micro-arc discharges on the workpiece surface). The plasma micro-arcs provide a heat source for surface modification via localized surface melting and rapid cooling (cleaning process) and, if desirable, enhance ion deposition on a given substrate (coating).

Three substrates (low carbon steel, pure Al and pure Ti) were “cleaned” by EPP and their near surface layer microstructure was studied. It was found that the uppermost layer for all three substrate materials was developing a “hill and valley” surface morphology, with individual characteristics influence by material’s properties such as melting point, undercooling and surface energy. The affected layer extends up to 2μm for all three substrates and the top layer was found to exhibit ultrafine grains. The EPP modified surface layer developed compressive residual stresses. The magnitude of the stress is correlated to the melting point which controls the annealing and grain growth kinetics, for each material.

Three coating materials, Zn, Ni and Mo, with a wide range of melting temperature were deposited by EPP on steel substrates. The topography exhibited by each coating was found to be influenced by its surface energy. Low surface energy coating material will present large nodules, high deposition rate and increased porosity. Medium surface energy coating materials were found to develop large nodules, lower deposition rates and low porosity. High surface energy coatings tend to present nodule coalescence and may exhibit crack formation, depending on the difference in T_M between the substrate and the coating material.

The microstructure at the coating/substrate interface was studied. Two controlling parameters were found regarding substrate/coating interface evolution. These are difference in melting point between substrate and coating material and the phase diagram characteristics. The extent of the interface was related to the difference in T_M between the coating and the substrate material. A low T_M coating material (Zn) interface will form intermetallics as predicted by the phase diagram. A coating with comparable T_M with the substrate (Ni) results in a liquid phase with both elements soluble and depending on the phase diagram characteristics, significant mixing can occur at the interface. The formation of the high melting temperature coating (Mo) was found to be dominated by its large T_M compared to the substrate. The continuous presence of a liquid phase of the substrate material was resulting in the extension of the interface far into the coating. Depending on the phase diagram, intermetallics may form at the interface.

The present findings show that a judicious selection of coating materials can be made by considering the coupling substrate – coating T_M and their binary phase diagram.

TABLE OF CONTENTS

LIST OF ILLUSTRATIONS

Figure Page

LIST OF TABLES

CHAPTER 1

INTRODUCTION AND MOTIVATION

The surface state of materials plays a critical role in their behavior [1–5]. Surface related properties can range from friction, wear [6, 7] corrosion and fatigue crack initiation [8, 9] to catalysis [9], adhesion [11] and biocompatibility [12]. Coatings are used extensively as a surface engineering technique to improve material performance in a wide field of applications.

In most applications, surface cleaning is an important step in any manufacturing process. It can be present as the finishing step or as precursor treatment for coating deposition. Especially for steel structures subjected to environmental interactions, cleaning is required prior to coating deposition. Surfaces, especially steel, are generally covered with a layer of contaminants, such as oil, grease and mill-scale layer oxide as a result of prior processing, some of which are intended as a temporary protective layer during in-process storage. Besides the need for removing those layers, surface preparation prior to deposition is required to enhance coating adhesion to the surface. A key to coating bonding strength and durability is the substrate surface roughness, which requires a particular morphology to provide good “anchor” for the coating [13]. Methods traditionally used for steel surface preparation prior to coating include: solvent cleaning, electrochemical polishing [12, 18 - 20], acid etching or pickling, and sand or grit blasting [14]. In practice, none of the cleaning processes mentioned above can be used effectively in a single-step and multistage procedures must be employed. These conventional methods have other disadvantages related to high energy consumption, environmentally-unfriendly, less desirable surface profile, etc. Electrolytic surface treatment techniques are well-known and used in some applications, but a major disadvantage is that they cannot remove mill-scale and heavy contaminants.

Coating deposition techniques presently accepted and used in industry, include ion sputter [15 – 17], electrodeposition [21, 22], plasma spray, Chemical Vapor Deposition (CVD),

Physical Vapor Deposition (PVD), etc. These techniques have their own drawbacks, among which are relatively low deposition rates, high energy consumption and/or use environmentally hazardous chemicals. Hot dipping and metal spraying have faster deposition rates but the resulting coatings have adhesion problems [23]. Thus, currently there is a need for new surface treatment methods, cost-effective, that are environmentally-friendly and can produce good quality and long-lasting surfaces.

A new technique for electrochemical surface treatment, known as Electrolytic Plasma Processing (EPP), has emerged in the last decade as an alternative to treatment for metallic surfaces. Although the discharge phenomena associated with electrolysis was well known for a long time [24], their importance as a surface engineering technique were realized only very recently [25]. The electrolytic plasma process includes two principal techniques: anodic and cathodic processes.

The technique has been intensively studied in the last decade, but overall emphasis of research is centered on performance evaluation, testing and characterization of the Plasma Electrolytic Oxidation (PEO – name under which the anodic process is known) coatings [26], mostly on aluminum and magnesium alloy. PEO has become a well-developed technology, with commercial applications by Keronite Ltd. (UK) achieving wide acceptance in industry.

On the other hand, the cathodic process is lagging far behind in fundamental understanding as well as control of processing parameters or processed surface analysis. Initial studies show that the EPP treated surfaces have increased corrosion resistance and a surface texture that enhances the adhesion of subsequent coatings [27].

Surface cleaning using the cathodic process developed by CAP Technologies (US) is still at the very first stage of introduction to the industrial environment. Process development however is based largely on empirical studies and understanding of the substrate – coating – process interaction is at the very early stage. In particular, the mechanism by which the coatings are formed is not well understood. Uncertainties regarding plasma process optimization, control and repeatability are some of the issues to be addressed for a full scale use of the process in the

industry. Also, only a few structure-property relations have been established, while most of the literature is focused on the oxide characteristics. Addressing these issues and fully exploiting the process, requires a better fundamental understanding of the interaction of plasma with material surfaces and its effect on produced material surface and coating characteristics.

CHAPTER 2

OBJECTIVES

The overall objective of the present work is to develop a fundamental understanding of formation of material surfaces and their characteristics as produced by EPP treatment. This process involves two components, cleaning and coating. The research is focusing in both aspects. Steel is by far the substrate of interest in cleaning and was included in the study. Since melting point was an important characteristic, two more substrates with different/wide variety of melting point were included also in the study. They are considered to be critical in the microstructural evolution of the produced surface layers during EPP and were studied at the same time.

The specific objectives are to study the:

i. Effect of material/plasma interactions on substrate surface layer formation and characteristics during cleaning;

ii. Effect of the coating material properties on evolution of the coating microstructure.

Again, steel was considered the most important material in the study, a combination of three materials with wide range of T_M were selected to study their interaction with steel used as a substrate in their deposition.

CHAPTER 3

REVIEW OF LITERATURE

3.1 Phenomenology

Cleaning is essential to many industrial processes, as a prelude to surface finishing or to protect active components. As an example, electroplating is in particular sensitive to surface cleanliness, since oil or mechanical debris can prevent the adhesion of the coating. Cleaning techniques include but are not limited to: solvent cleaning, hot alkaline detergent cleaning, electro-cleaning and acid etch. Acid pickling in particular is a widely used technique for metal surface treatment. A solution containing strong acids (hydrochloric acid and previously used sulfuric acid) are most commonly used especially for steel in various steelmaking processes. Disadvantages from the use of such products are: difficulty to handle because of high corrosiveness, hydrogen embrittlement for some steels and the pickling sludge from acid cleaning is considered a hazardous waste by EPA and requires neutralization before disposure.

3.1.1 Coating Techniques

3.1.1.1 Plasma Spraying

Plasma spraying [28] is a thermally activated coating procedure in which melted (or heated) materials are sprayed onto a surface by a plasma jet. In the jet, where the temperature is on the order of 10,000 K, the material is melted and propelled towards a substrate. There, the molten droplets flatten, rapidly solidify and form a deposit. Commonly, the deposits remain adherent to the substrate as coatings; free-standing parts can also be produced by removing the substrate. There are a large number of technological parameters that influence the interaction of the particles with the plasma jet and the substrate and therefore the deposit properties. Plasma spraying can be characterized by the plasma forming medium (usually hydrogen, argon, or helium and their mixtures) and spraying environment (air or vacuum plasma spraying), and plasma jet generation (direct current – DC plasma, or induction plasma – RF current).

Vacuum plasma spraying is also used for etching and surface modifications to create porous layers with high reproducibility. Figure 3.1 represents a typical plasma spraying system. Plasma processing is done in a controlled environment inside a sealed chamber at a medium vacuum, around 13 - 65 Pa. The gas or mixture of gases is energized by an electrical field from DC to microwave frequencies, typically 1 – 500 W at 50 V. The treated components are usually electrically isolated. The volatile plasma by-products are evacuated from the chamber by a vacuum pump [29, 30].

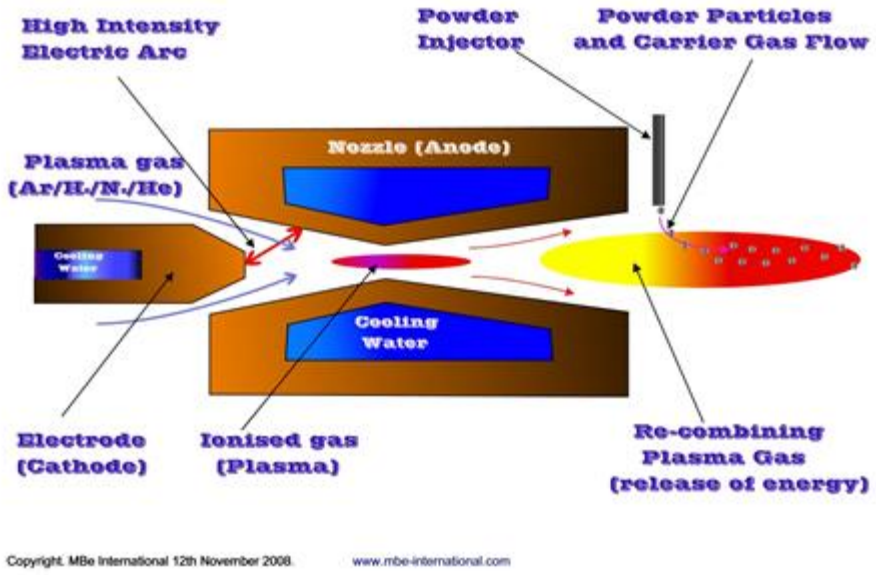

Figure 3.1 Plasma spraying system.

This technique is mostly used to produce coatings on structural materials. Such coatings provide protection against high temperatures (for example thermal barrier coatings for exhaust heat management), corrosion, erosion, wear, etc. The deposits consist of a multitude of pancake-like lamellae called 'splats', formed by flattening of the liquid droplets. As the feedstock powders typically have sizes from micrometers to above 100 micrometers, the lamellae have thickness in the micrometer range and lateral dimension from several to hundreds of micrometers. Between these lamellae, there are small voids, such as pores, cracks and regions of incomplete bonding.

As a result of this unique structure, the deposits can have properties significantly different from bulk materials. These are generally mechanical properties, such as lower strength and modulus, higher strain tolerance, and lower thermal and electrical conductivity. Also, due to the rapid solidification, metastable phases can be present in the deposits.

3.1.1.2 Electroplating

Electroplating is a plating process that uses electrical current to reduce cations of a desired material from a solution and coat a conductive object with a thin layer of the material, such as a metal or alloy. Electroplating is primarily used for depositing a layer of material to bestow a desired property (e.g., abrasion and wear resistance, corrosion protection, lubricity, aesthetic qualities, etc.) to a surface that otherwise lacks that property. Another application uses electroplating to build up thickness on undersized parts [31].

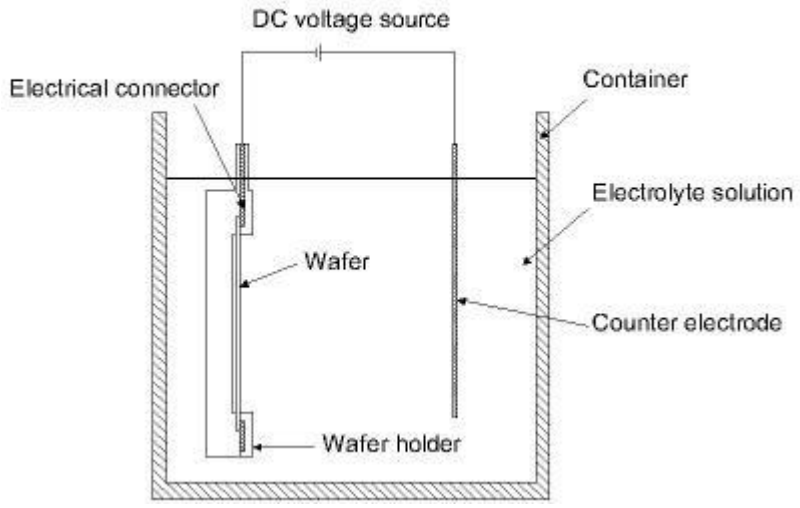

Figure 3.2 Typical setup for electroplating.

The process of electrodeposition is analogous to a galvanic cell acting in reverse. The part to be plated is the cathode of the circuit. In one technique, the anode is made of the metal to be plated on the part, Figure 3.2. Both components are immersed in an electrolyte containing one or more dissolved metal salts as well as other ions that permit the flow of electricity. A rectifier

supplies a direct current to the anode, oxidizing the metal atoms that comprise it and allowing them to dissolve in the solution. At the cathode, the dissolved metal ions in the electrolyte solution are reduced at the interface between the solution and the cathode, such that they "plate out" onto the cathode. The rate at which the anode is dissolved is equal to the rate at which the cathode is plated, vis-à-vis the current flowing through the circuit. In this manner, the ions in the electrolyte bath are continuously replenished by the anode [32]. Other electroplating processes may use a non consumable anode such as platinum. In these techniques, ions of the metal to be plated must be periodically replenished in the bath as they are drawn out of the solution.

The current density in this process strongly influences the deposition rate, plating adherence, and plating quality. This density can vary over the surface of a part, as outside surfaces will tend to have a higher current density than inside surfaces. The higher the current density, the faster the deposition rate will be, although there is a practical limit enforced by poor adhesion and plating quality when the deposition rate is too high.

While most plating cells use a continuous direct current, some employ a cycle (8–15 seconds on followed by 1–3 seconds off). This technique is commonly referred to as "pulse plating" and allows high current densities to be used while still producing a quality deposit. In order to deal with the uneven plating rates that result from high current densities, the current is even sometimes reversed in a method known as "pulse-reverse plating", causing some of the plating from the thicker sections to re-enter the solution. In effect, this allows the "valleys" to be filled without over-plating the "peaks". This is common on rough parts or when a bright finish is required. In a typical pulse reverse operation, the reverse current density is three times greater than the forward current density and the reverse pulse width is less than one-quarter the forward pulse width. Pulse-reverse processes can be operated at a wide range of frequencies up to the order of MHz [31].

3.1.1.3 Chemical Vapor Deposition

CVD is a chemical process used to produce high-purity, high-performance solid materials. The process is often used in the semiconductor industry to produce thin films. In a

typical CVD process, the substrate is exposed to one or more volatile precursors, which react and/or decompose on the substrate surface to produce the desired deposit. Frequently, volatile by-products are also produced, which are removed by gas flow through the reaction chamber.

The CVD process can be generalized as a sequence of steps (Figure 3.1):

1) convective and diffusive transport of reactants from the gas inlets to the reaction zone

2) Chemical reactions in the gas phase to produce new reactive species and by-products

3) Transport of the initial reactants and their products to the substrate surface

4) Adsorption (chemical and physical) and diffusion of these species on the substrate surface

5) Heterogeneous reactions catalyzed by the surface leading to film formation

6) Desorption of the volatile by-products of surface reactions

7) Convective and diffusive transport of the reaction by-products away from the reaction zone.

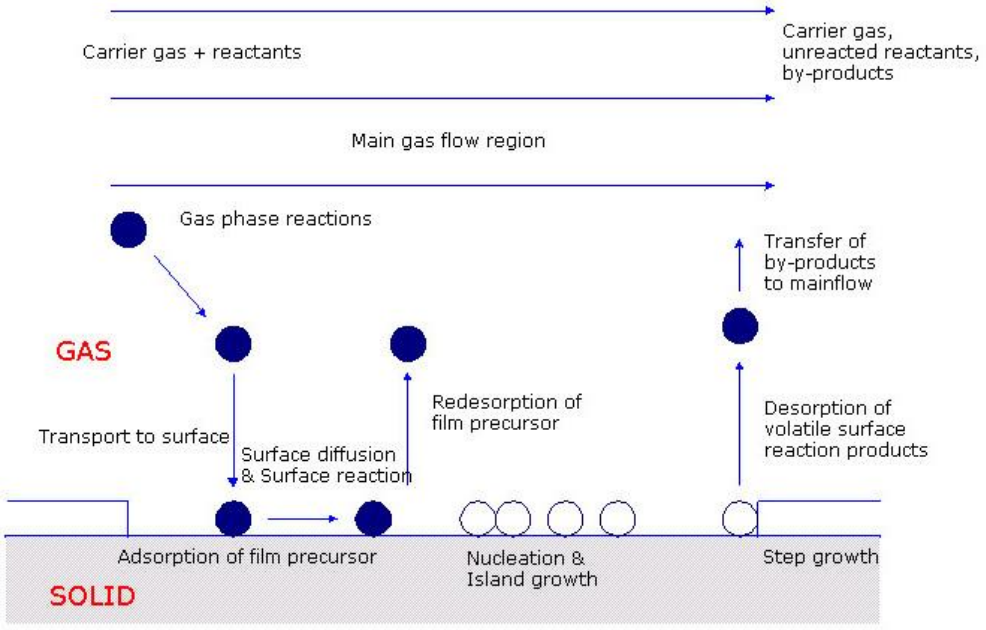

Figure 3.3 Sequence of gas transport and reaction processes in CVD [33].

Most CVD processes can be conveniently subdivided into two categories: thermal CVD processes employ heat energy to activate the required gas and gas-solid phase reaction, and plasma-enhanced CVD processes are based on plasma activation of the involved chemical species. Regardless of processing type, the design of process equipment must have the following

capabilities: deliver and control supply of the reactant gases into the reactor, supply heat to the substrate so that reaction and deposition can proceed efficiently, remove the by-product and depleted gases.

Microfabrication processes widely use CVD to deposit materials in various forms, including: mono-crystalline, polycrystalline, amorphous, and epitaxial. These materials include: silicon, carbon fiber, carbon nanofibers, filaments, carbon nanotubes, SiO_2, silicon-germanium, tungsten, silicon carbide, silicon nitride, silicon oxynitride, titanium nitride, and various high-k dielectrics. The CVD process is also used to produce synthetic diamonds.

Some metals (notably Al and Cu) are seldom or never deposited by CVD. However, CVD processes for Mo, Ta, Ti, Ni, and W are widely used. These metals can form useful silicides when deposited onto silicon. Mo, Ta and Ti are deposited by Low Pressure CVD, from their pentachlorides. Ni, Mo, and W can be deposited at low temperatures from their carbonyl precursors. In general, for an arbitrary metal M, the reaction is as follows:

$$2\ MCl_5 + 5\ H_2 \rightarrow 2\ M + 10\ HCl$$

The usual source for W is WF_6, which may be deposited in two ways:

$$WF_6 \rightarrow W + 3\ F_2$$

$$WF_6 + 3\ H_2 \rightarrow W + 6\ HF$$

The advantages of the CVD technique consist of producing uniform, pure, reproducible and adherent coatings at low or high rates. Disadvantages are the chemical hazards caused by toxic, explosive, inflammable or corrosive gases [34 - 37].

3.1.1.4 Physical Vapor Deposition

PVD includes a variety of vacuum deposition processes and is a general term used to describe any of a variety of methods to deposit thin films by the condensation of a vaporized form of the material onto various surfaces. The coating method involves purely physical processes such as high temperature vacuum evaporation, ion beam or plasma sputter bombardment rather than involving a chemical reaction at the surface to be coated as in chemical vapor deposition.

PVD methods are clean, dry vacuum deposition methods in which the coating is deposited over the entire object simultaneously, rather than in localized areas [38].

A schematic reactor for PVD under sputtering is represented in Figure 3.4. At low pressure, a voltage is applied to two parallel electrodes resulting in a plasma discharge. The accelerated gas ions impinge onto the cathode (target) and metal atoms are emitted from the target which deposit on the wafer leading to layer growth.

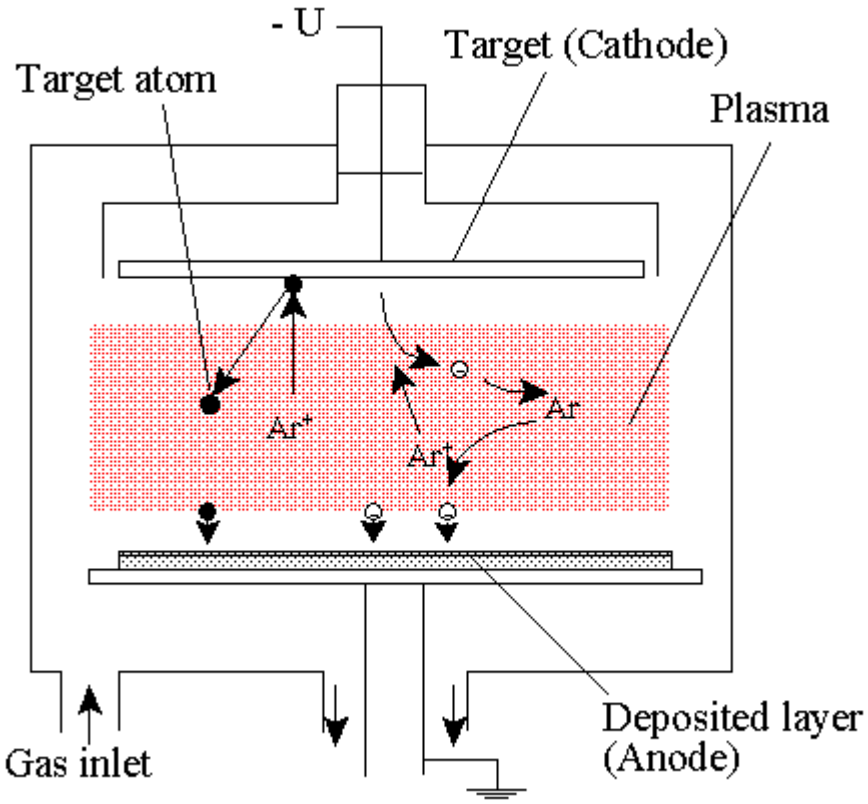

Figure 3.4 Schematic reactor for PVD via magnetron sputtering.

Variants of PVD include, in order of increasing novelty [39]:

- Evaporative deposition: in which the material to be deposited is heated to a high vapor pressure by electrically resistive heating in "low" vacuum.

- Electron beam physical vapor deposition: in which the material to be deposited is heated to a high vapor pressure by electron bombardment in "high" vacuum.
- Sputter deposition: in which a glow plasma discharge (usually localized around the "target" by a magnet) bombards the material sputtering some away as a vapor.
- Cathodic Arc Deposition: in which a high power arc directed at the target material blasts away some into a vapor.
- Pulsed laser deposition: in which a high power laser ablates material from the target into a vapor.

PVD is used in the manufacture of items including semiconductor devices, aluminized PET film for balloons and snack bags, and coated cutting tools for metalworking. Besides PVD tools for fabrication special smaller tools mainly for scientific purposes have been developed. They mainly serve the purpose of extreme thin films like atomic layers and are used mostly for small substrates. Good examples are mini e-beam evaporators which can deposit monolayers of virtually all materials with melting points up to 3500°C.

3.1.1.5 Galvanizing

Typically refers to hot-dip galvanizing, a metallurgical process that is used to coat steel or iron with zinc. This is done to prevent galvanic corrosion (specifically rusting) of the ferrous item; while it is accomplished by non-electrochemical means, it serves an electrochemical purpose.

Hot-dip galvanized steel has been effectively used for more than 150 years. The value of hot-dip galvanizing stems from the relative corrosion resistance of zinc, which, under most service conditions, is considerably better than those of iron and steel. Zinc coatings prevent corrosion of the protected metal by forming a physical barrier, and acting as a sacrificial anode if this barrier is damaged. When exposed to the atmosphere, zinc reacts with oxygen to form zinc oxide, which further reacts with water molecules in the air to form zinc hydroxide. Finally, zinc hydroxide reacts with carbon dioxide in the atmosphere to yield a thin, impermeable, tenacious and quite insoluble dull grey layer of zinc carbonate which adheres extremely well to the underlying zinc, so protecting it from further corrosion, in a way similar to the protection afforded

to aluminum and stainless steels by their oxide layers. Furthermore, galvanizing for protection of iron and steel is favored because of its low cost, the ease of application, and the extended maintenance-free service that it provides.

3.1.2 Electrolysis Terminology

Used largely in chemistry and manufacturing, electrolysis is a method of using an electrical current to drive an otherwise non-spontaneous chemical reaction. The electric current passes through an ionic substance that is most often dissolved into an aqueous solution. The main components required to achieve electrolysis are two electrodes immersed in the ionic solution and an external voltage applied between the electrodes. The electrical charge is carried by the mobile ions and each electrode attracts ions that are of opposite charge. Positively charged ions (cations) are moving towards the electron providing (negatively charged) electrode called cathode while the negatively charged ions move towards the positively charged electrode (anode). The energy required to achieve ions migration between electrodes is provided by the external source of electrical potential. The amount of electrical energy that must be added is related to the change in Gibbs free energy of the reaction taking place in the electrolyte. The oxidation (loss of electrons) of ions occurs at the anode and the reduction (gain of electrons) of ions at the cathode [43].

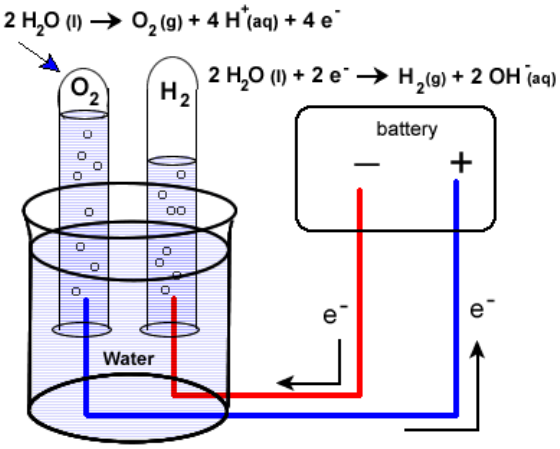

Figure 3.5 Electrolysis of water [44].

An example of such reactions is provided by the electrolysis of water, which is the most common electrolyte medium used in applications involving EPP:

$2H_2O \rightarrow O_2 + 4\ H^+ + 4\ e^-$ Anode (oxidation) E^o (oxidation) = -1.23 V (vs. SHE)

$2\ H^+ + 2\ e^- \rightarrow H_2$ Cathode (reduction) E^o (reduction) = 0.00 V (SHE)

where E^o is the standard potential for water electrolysis. The standard potential is defined relatively to the standard hydrogen electrode (SHE) - reference electrode, which is arbitrarily given a potential of 0.00 Volts. The negative voltage indicates that the Gibbs free energy for electrolysis of water is greater than zero for these reactions, so the reaction cannot occur without adding the necessary energy, usually supplied by the applied potential.

3.1.3 Plasma Terminology

By definition, plasma is a gas, in which a certain portion of its particles are ionized. The presence of the charge carriers makes plasma electrically conductive so that it has properties unlike those of solids, liquid or gases and is considered to be a distinct state of matter. Like gases, plasma does not have a distinct shape but under influence of a magnetic field will form structure like filaments. Although plasma contains ions and electrons about in equal number, if present very close to an electrode, the ions specie will dominate and plasma will be characterized by its ion content. Temperature controls the degree of plasma ionization, and is a measure of the thermal kinetic energy per particle. In particular, plasma ionization is determined by the “electron temperature” relative to the ionization energy. Under an applied potential, the particles are accelerated and the plasma temperature will increase, and this property is taken advantage of in “plasma processing” techniques, weather it takes place in vacuum or aqueous electrolytes (atmospheric plasma) [45].

3.1.4. Electrolysis Enhanced Surface Bubble Formation

Various recent studies [46 - 48] on surface bubble formation have tried to explain the formation and stability of small scale size bubbles located at the liquid-solid interface. The size and density of these bubbles depends on the dissolved gas concentration and they disappear completely when the liquid is degassed [46]. The classical theory of bubble stability [47]

expresses that small bubbles have large internal gas pressure, in order to balance the compressive action of surface tension. This internal pressure (Laplace pressure) is much larger than the gas concentration at the outside, leading to a diffusive outflow of gas and bubble dissipation. Bubble stability against dissolution requires a physical effect to cancel the diffusive outflow. Stabilization can be achieved by mechanisms causing an influx of gas into the bubble. Such an influx was suggested to occur not uniformly across the bubble surface, but localized near the contact line with the wall [46]. Molecular dynamic simulations demonstrated the origin of such influx to exist due to gas enrichment near solid walls [48]. Such an enhanced gas concentration at hydrophobic walls was confirmed by spectroscopy [49] and with x-ray reflectivity measurements [50]. There is a bubble size for which a dynamic equilibrium exists. This bubble radius is determined by several factors, such as material properties of the solid wall and the relative gas concentration. The driving mechanism of bubble formation and evolution is a transitory one to avoid conflict with the second law of thermodynamics.

For EPP, the mechanism can be related to the temperature gradient due to plasma formation. It has been shown that one method to create controlled non-equilibrium conditions for surface bubble generation is through electrolysis [51]. By analogy with the water boiling process, the different conditions corresponding to bubble formation and film boiling can be traced in plasma electrolysis and can produce a continuous gaseous envelope [52].

3.2 Development of the EPP Process

The first significant work in using the electrolytic and plasma discharge phenomena for hybrid application was conducted in 1964 by Kellogg [53]. The essential features of the glow-discharge electrolysis process were then analyzed and interpreted as a form of electrolysis in which energy transfer as well as charge transfer is involved, and this serves to break up solvent molecules into reactive radicals that will produce the chemical reactions being observed. It was also suggested that energy is conveyed by gaseous ions accelerated in the electrical field near the liquid surface.

In 1981, Sengupta [54] conducted work on the high voltages required for a normal electrolysis to switch over to a phenomenon called contact glow discharge electrolysis (CGDE). He also looked into the anode-cathode relative distance, electrolyte influence and polarity of the electrode on the growth of a stable vapor envelope during normal electrolysis. Later on, [55], the same author published an analysis of the chemical products obtained at the anode during CGDE in inert electrolytes at various applied voltages and electrolyte compositions and found that the main products, H_2 and O_2 from the dissociation of water molecules are the result of plasma around the anode when the glow discharge is maintained constant. A comparative study of the chemical yields of anodic and cathodic CGDE indicates that the breakup of water molecules occurs entirely in the plasma during cathodic CGDE, but primarily in the liquid (electrolyzed water) and partly in the plasma during the anodic phenomenon. It can be observed that different phenomena occur depending on the evolution of the discharge, anodic or cathodic.

Several other studies have been conducted on plasma electrolysis, on issues regarding the basic science [56, 57] and practical applications [58, 59]. All studies have in common the observation that for a certain voltage applied between the two electrodes, a significant deviation from the Faraday's normal electrolytic regime occurs. The conclusion of the studies was that several factors may influence the formation and evolution of the continuous plasma surrounding the electrodes: applied potential, temperature and properties of the electrolyte medium, flow dynamics, electrodes material and geometry. Others, such as applied current (DC or pulse), processing time or gap between electrodes are also presently investigated.

Figure 3.6 shows a simplified representation of the electrochemical processes taking place at the electrodes in an aqueous solution during Plasma Electrolysis. The activity of gaseous oxygen and hydrogen as byproducts of water electrolysis is of particular importance. At the anode, made of metals which exhibit anodizing behavior (Al, Mg, Ti), the oxygen promotes oxide formation. At the metallic cathode, atomic hydrogen assists in the formation of plasma envelope while the cations from electrolyte are accelerated toward the electrode for coating formation.

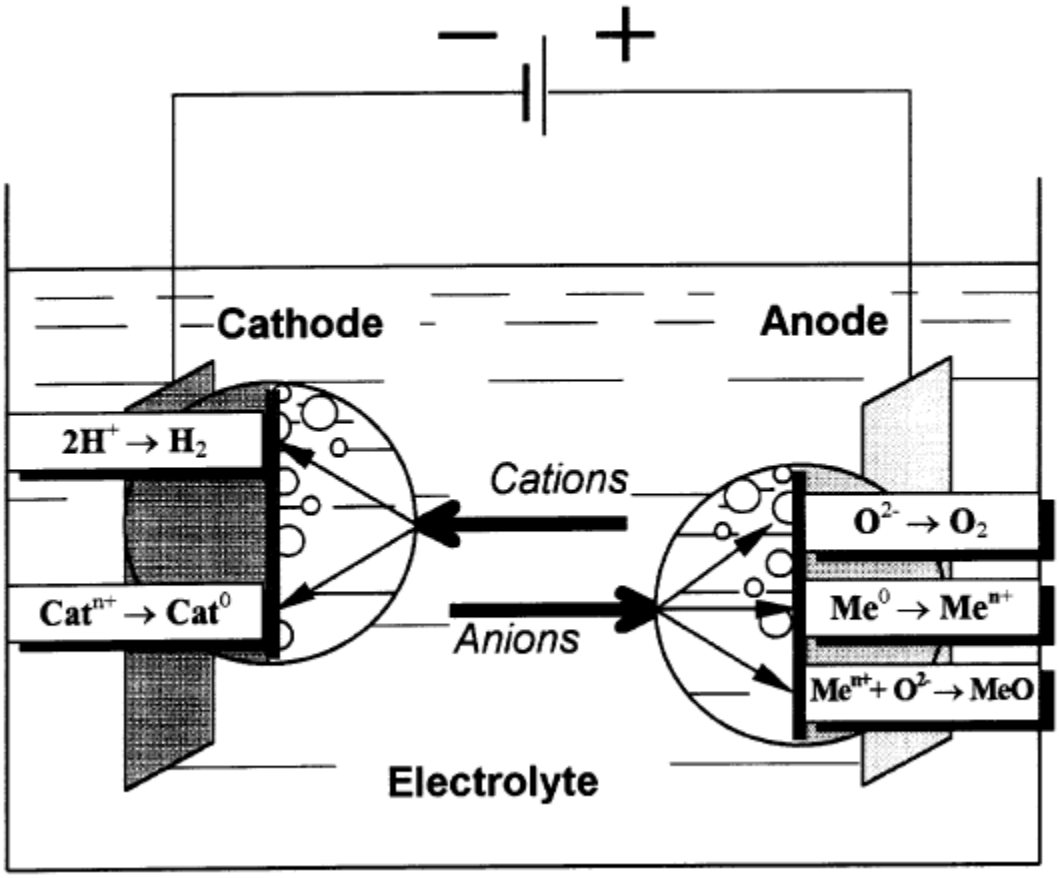

Figure 3.6 Electrode processes in electrolysis of aqueous solutions [60].

A review on plasma electrolysis published in 1999 by Yerokhin et al. [60] summarized most of the known fundamental knowledge on the process applied to surface engineering, from the point of view of the anodic process. The study left open the extent of fields of applications, which is only at its incipient stage. While PEO has become a well-developed technology over the past 10 years [61], applications for the cathodic process (referred in this work from now on as EPP) were only starting to emerge in the early 2000. Among the first to be mentioned are: plasma electrolytic nitrocarburizing treatments for stainless steel [62 – 65] and cleaning and coating of metallic surfaces (most common used on steel surfaces) [27, 66]. Recent works [67 – 69] were published on the application of “pulsed” DC current during EPP processing. Initially, the pulse source was considered for the anodic process and only recently 4340 steel was cleaned [67] and

Zn-Ni-Cd coatings were deposited [69] with the cathodic process. The applied pulse current allows in theory more control of discharges used in various surface treatments and coatings. Also, thermal impact from the treatment is in significant on the surface hardness of steel compared to the DC approach and cleaning of the surface is more effective with increased duty cycle and frequency [67]. More work is needed to evaluate the influence of pulse potential on the microstructure and mechanical properties of deposited coatings.

3.3 Description of EPP

The EPP process is based on the cathodic regime of the electrolytic plasma processing involving the electrolysis of a liquid environment by application of an electrical potential between the workpiece and a counter-electrode, and the production of plasma (micro-arc discharges on the workpiece surface). The electrolytic-plasma results in fine bubble formation and collapsing with simultaneous forceful disruptions and shock wave production along with local melting of a thin material surface layer. These events are very effective in creating a “clean” metal surface. Furthermore, the local surface is melting and subsequent quenching resulting in ultra-fine grain structures and a favorable ‘anchor’ surface profile providing a proper mechanical interlocking for a subsequent coating treatment. Deposition of coatings predominantly occurs by ion acceleration through the plasma, ion adsorption and transport to the surface via bubble collapsing. These processes eliminate boundary layer diffusion and result in very high deposition rates compared to traditional electroplating.

Figure 3.7 represents a typical current-voltage characteristic curve for the EPP process. In the U_1 region, the current increases linearly following Faraday’s law. The regime is characterized by gas liberation at the near surface of the cathode, mainly H_2. The high voltage (180 – 200 V) characteristic to EPP will enhance greatly water electrolysis and will produce excess H_2 which will migrate towards the cathode and will be the source for bubble formation and growth. Upon further voltage increase, at a certain point, U_2, first luminescence can be observed. Initially, it was believed that normal electrolysis at high voltages switches over spontaneously to

contact glow discharge electrolysis due to electrolytic gas evolution. Sengupta [55, 71] showed that this phenomenon was due to electrolyte vaporization due to Joule heating [72] and to the hydrodynamic instabilities in solvent vaporization at the electrode. These two factors contribute to the transition of normal electrolysis to CGDE. The glow color depends upon the nature of the metal ions present in the solution.

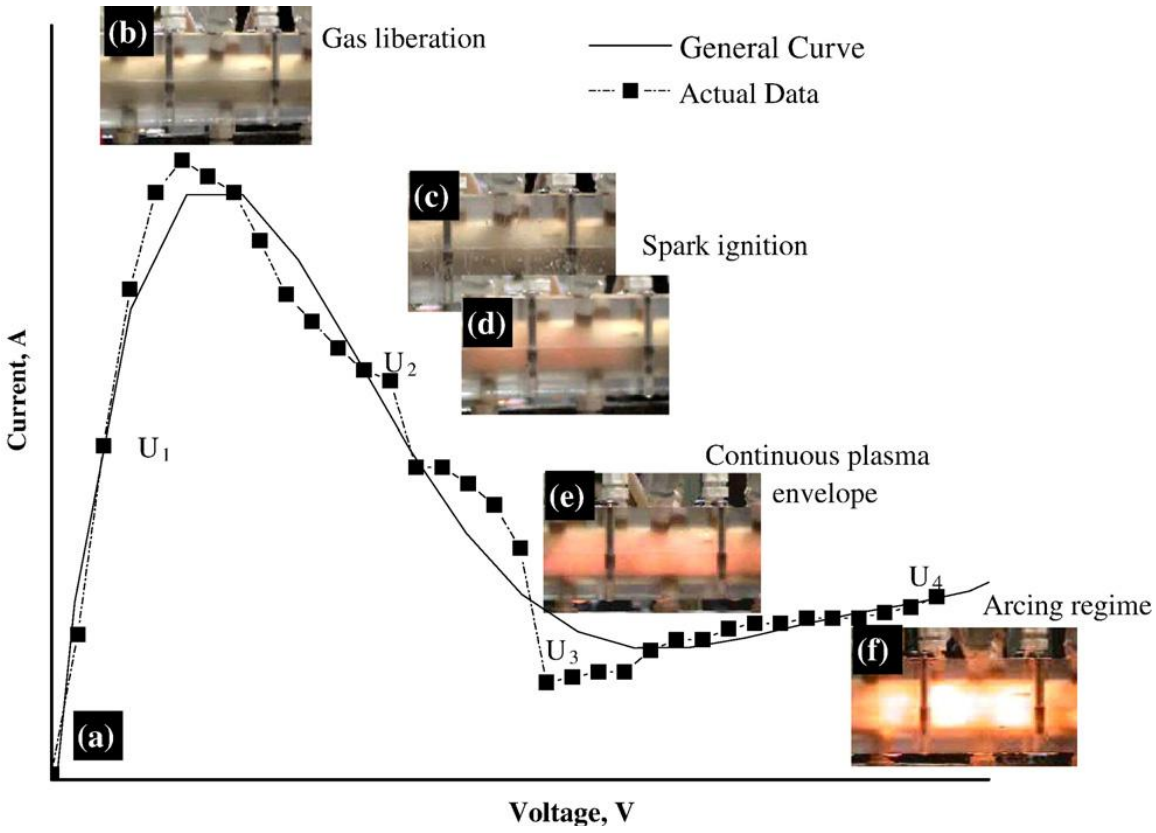

Figure 3.7 Current – Voltage dependence in EPP [70].

The U_3 zone is selected as the work region, where the electrode current decreases but plasma intensity increases from U_2 to U_3. This increase in plasma evolution is due to the fact that almost all the voltage is dropped in this limited contact region between the gaseous hydrogen bubble and substrate surface. The sample (cathode) can be either immersed in the electrolyte or electrolyte can drip on the sample [73] through a “perforated” anode. When dripped, the electrolyte is released onto the workpiece through small holes made in the anode and forms an

enveloping “foam” that has a stabilizing effect on the plasma formation. A plasma envelope is fully formed at U_3 characteristic voltage and this is the normal operating voltage for surface treatment. This regime was first mentioned by Kellogg [74] and is called Kellogg region. Although there is heating of the substrate due to plasma action, the bulk substrate temperature remains relatively low (<100ºC) due to simultaneous cooling action by the surrounding electrolyte solution. The local surface temperature adjacent to plasma is very high, which is critical for the interactions at the near surface and the effect produced on surface characteristics. The current density was shown to depend on geometrical factors related to the electrodes [75] (size, shape, orientation and electrode gap).

3.4 EPP Interaction with Material Surfaces

Metallic coatings can enhance surface sensitive material properties (resistance to corrosion, wear, fatigue crack initiation, etc.). Before coating, a surface requires cleaning to remove oxides and other contaminants for successful deposition and a strong adhesion between the coating and substrate surface.

Figure 3.8 is a schematic representation of the EPP process mechanism. As mentioned before, the processing time corresponds with the stable plasma completely surrounding the workpiece. For the sake of process modeling, we assume the gaseous envelope is composed of discrete gas bubbles. The applied voltage between electrodes is high, around 150-250 V and it will induce a concentration of positive ions from the electrolyte around the virtual bubbles formed by the hydrogen evolution from electrolysis. Thus, a very high positive charge is at close proximity of the cathode which will generate a high localized electric field, reported to reach 10^5 V/m or higher [67, 73, 76]. At such high electric field, the gas inside the bubble is ionized, becomes plasma and discharge is initiated, Figure 3.8(a). The ionization phenomena appear initially as a rapid sparking in individual gaseous bubbles and then transforms into a uniform glow distributed all around the enveloping gaseous layer. Plasma temperature can reach thousands of degrees,

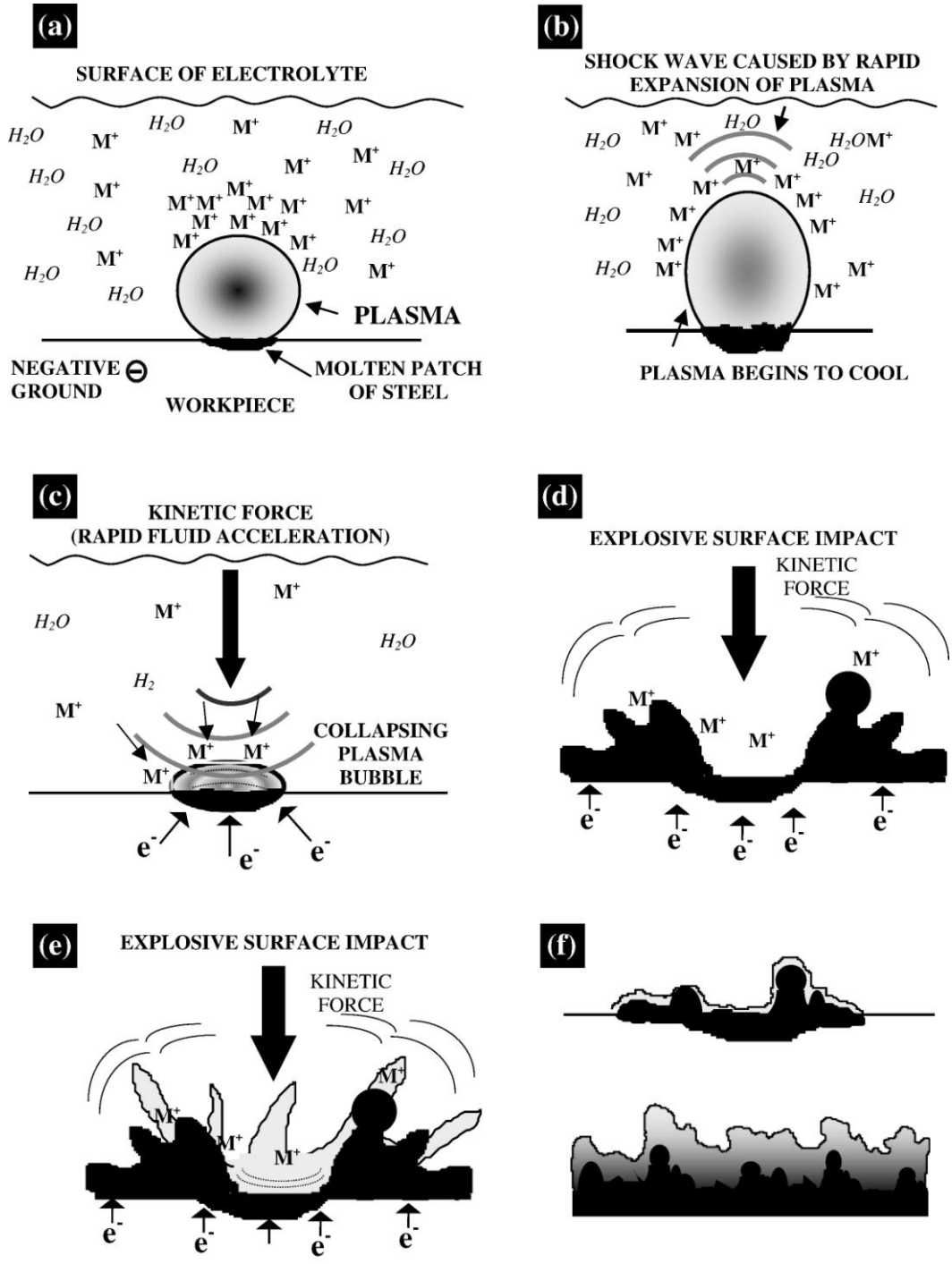

Figure 3.8 Schematic of the EPP process mechanism showing one single plasma bubble: (a) plasma bubble on the surface of the work piece, (b) shockwave production by the cooling plasma bubble, (c) collapsing plasma bubble and cleaning, (d) collapsing plasma bubble and creation of micro-crater, (e) collapsing bubble deposits ions in case of coating, and (f) increasing coating thickness with processing time [70].

based on anodic process studies [60]. Although the temperature of the plasma is high, the surrounding electrolyte is at much lower temperature (boiling water temperature), resulting in cooling of the plasma that will generate a collapse of the bubble onto the substrate surface, Figure 3.8(b) to 3.8(d). The extinction of the discharge takes place as the bubbles collapse, and the total duration was estimated at ~ 10^{-6} s per each individual collapse. Recent studies on the anodic EPP revealed that discharges are individual events present at a given time, although the plasma envelope appearance is uniform around the workpiece [77].

The implosion of the plasma bubble triggers two phenomena at the surface of the cathode. First, the metal ions present in the electrolyte near the surface of the collapsing bubble are accelerated toward the substrate surface by riding on the surface of the bubble and thrown on the metal surface. Second, the stored kinetic energy from the bubble, as it collapses, is released onto the surface of the cathode. This energy can be very high, comparable to that in cavitation process, which is reported in the order of hundreds of MPa or higher [78]. The kinetic energy will further move the accelerated ions towards the cathode surface. This combined action results in unrealistically high deposition rates (as high as 1 μm/s), as evidenced by previous experimental observations [25, 27] and shown in Figure 3.8 (e) and (f). The movement of ions toward the electrode is driven by two main components: ion acceleration through the plasma and ion absorption transport as the bubble collapses. Of a lesser effect is the hydrodynamic transport of ions promoted by electrolyte flow through the reactor [73]. The combination of the above actions leads to high deposition rates. The observed plasma phenomena are described by various sources as glow, corona, spark or arc-plasma. The reported discharge temperatures vary widely, from 800–3000 K [79] to 3000–6000 K and even 10000–20000 K [77]. These differences have arisen from the complex structure of the plasma discharge, reported to have a hot core (6000–9000 K) and a “cold” circumferential area (1600–2000 K) [80]. More recent reports [81, 82], using emission spectra characteristics, have confirmed that there are two distinct regions of plasma: a lower density peripheral region at ~ 3500 K and a higher density core at ~ 16000±3500 K.

Following the bubble collapse, the surface is quenched by the electrolyte environment and can lead to unique surface microstructures. The impurities are instantly removed by the action of the heat and the mechanical impact of the shock wave from collapsing bubble, while the hydrogen reduces oxides at the surface [27]. A desirable profile is created with micro-craters from the localized melting and bubble cavitations, providing a mechanical interlocking for subsequent coating.

Coating deposition is a combination of three concurrent processes: ion acceleration through the plasma, ion adsorption and transport to the surface via bubble collapsing. The metal ions present in the electrolyte are accelerated toward the substrate surface by riding on the surface of the bubbles and thrown on the metal surface as the bubbles collapse. Due to local surface melting, deposition initially is expected to occur as a mixing layer of substrate/coating elements, resulting in a good adhesion for the subsequent coating formation. Due to high plasma energy and very fast cooling rates, an ultrafine grain structure can form along with non-equilibrium phases at the substrate/coating interface.

EPP has the ability to routinely deposit metal and alloy coatings, such as Zn, Ni, Zn-Ni, Ni-Cu and recently to alloy metals such as Mo onto the metallic substrate [40]. The present work will address both issues: metal coating deposition and surface alloy mixing, processes that can intrigue the interest for industrial applications.

3.5 Recent Advances in Processing Parameters and Equipment

One of the most recent advances in EPP involves filling the electrode gap between the anode and cathode with an electrically conductive medium consisting of a foam comprising a vapor phase and a liquid phase, as opposed to just the liquid phase in the immersion or flow-through technique [41, 42]. The foam technique can be used for both cleaning and coating applications. The operating parameters that can be adjusted to provide the necessary conditions for the establishment of electrolytic plasma include the voltage, the chemical composition, the density and the temperature of the foam, the rate at which the foam is supplied to the working gap, and the width of the working gap (distance between the anode and the cathode). There are

several methods for generating the foam, including using heaters in the anode assembly to raise the temperature of the electrolyte to near its boiling point or using chemical foaming agents. Generally, 50% by volume of the foam is gas with the reminder being liquid.

The use of a foam as a conductive medium has several advantages over liquid electrolytes:

i. The foam, by virtue of its gas/vapor content, has a lower conductivity than the liquid, which reduces the power consumption and improves the economics of the process.

ii. Because the bubble size and overall vapor content of the foam may be varied, it provides an additional means of control over the power consumption and the intensity of the process; this in turn permits control over the roughness of the cleaned or coated surface.

iii. Since the foam fills the entire working gap, electrical conduction involves the entire electrode surface of the anode and workpiece (cathode). The use of foam thus improves the uniformity of the process both as regards the treated surface and the erosion of any sacrificial anode used for coating.

iv. When liquid streams impinge on the workpiece there is a limit to the size of the working gap that can be used in practice because the liquid streams break up and destroy the conductive pathway. This does not occur when foam fills the working gap uniformly, so that both smaller and larger working gaps can be used. This has great practical importance for cleaning and coating of internal surfaces and complex geometries where it is not practicable to maintain a uniform working gap.

Another favorable aspect of the process is the ability to collect the electrolyte, pass it through a filtration system, and then reuse it after adding the appropriate chemical compounds for either cleaning or coating operations. This ability to recycle the electrolyte virtually eliminates any waste disposal problems associated with the process and further adds to its environmental attractiveness.

It seems that EPP can offer several research opportunities given a better fundamental understanding is gained.

CHAPTER 4

EXPERIMENTAL TECHNIQUES

4.1 Materials

Three metallic materials were used as substrates. All processed samples in the present study were 50mm x 10mm x 3mm strips. All samples were finely ground down to 600 grit SiC paper as the last step. Materials used as substrates for cleaning processing were: low carbon steel (mentioned for simplification as steel in the present work), 1100 aluminum (mentioned as Al) and commercially pure titanium (mentioned as Ti).

Three coating materials were studied. Steel was selected as the substrate for all three coating materials. Steel was selected due to its widespread use in all processing, more than any other material. The selected coatings were Zn, Ni and Mol. Several factors have influenced the coating material selection. For example, Zn is presently used on large scale as coating on steel, so it will be convenient to relate and compare its EPP coating deposition characteristics with other processes. The major factor for the coating selection was its melting temperature (T_M). For the given steel substrate, coatings were chosen to cover a wide range of $T_{M.}$ Zn was at the lower limit, Ni closely matching Fe and Mo at the upper limit, Table 4.1. As noted earlier, EPP involves repeated cycles of localized melting and rapid cooling at the surface and thus, the T_M of substrate and coating material is expected to play a critical role in the interface substrate/coating formation

Table 4.1 T_M for substrate and coatings selected for EPP processing

Material	T_M [ºC]	
	EPP cleaning	EPP coating
steel (Fe)	1538	1538
Al	660	
Ti	1668	
Zn		419
Ni		1453
Mo		2623

4.2 Experimental Setup

All processing in the present work was conducted in an electrolytic plasma unit located at CAP Technologies (Baton Rouge, LA), figure 4.1. An experimental laboratory unit was also built at the University of Texas at Arlington, Figure 4.2.

An important aspect of EPP is the anode design. Figure 4.3 presents design type of anodes that have been fabricated for flat specimen processing.

A typical unit at CAP Technologies is shown in Figure 4.1. Also, Figure 4.2 shows the laboratory unit built in the Surface and Nano Engineering Laboratory at UTA. In the processing equipment using the “foam” technology, the workpiece is surrounded by foam rather than by a thin electrolyte layer. The unit is capable of processing a variety of material shapes (i.e. round and flat metal surfaces. The active elements are the anode and the cathode (workpiece). The anode is perforated allowing flow of the electrolyte on to the cathode surface. EPP does require a specific uniform plasma state and the anode to cathode distance is one parameter the steady plasma depends upon. The anode assembly involves a mechanism for adjustment of the anode-cathode working distance. The electrolyte is being admitted directly from the supply tank into a vertical cylinder that has a diffuser plate positioned just above the perforated anode disk. The role of the diffuser is to distribute the electrolyte flow even before it reaches the anode. An immersion heater with steel tubing and temperature controller achieves electrolyte heating to desirable temperature. The electrolyte flow is adjusted via a mechanical pump and a regulator. A generator unit with DC and pulse capabilities is providing the required power. The cathode is connected to the power supply and the ground to the anode through a copper rod that is electrically isolated from the electrolyte by being inserted into the wall of the vertical Plexiglas cylinder. The anode is connected to the ground. The processing unit has the capability of processing under a desired atmosphere (Ar, N_2, etc.). The unit can be modified to process other shapes of specimens if required.

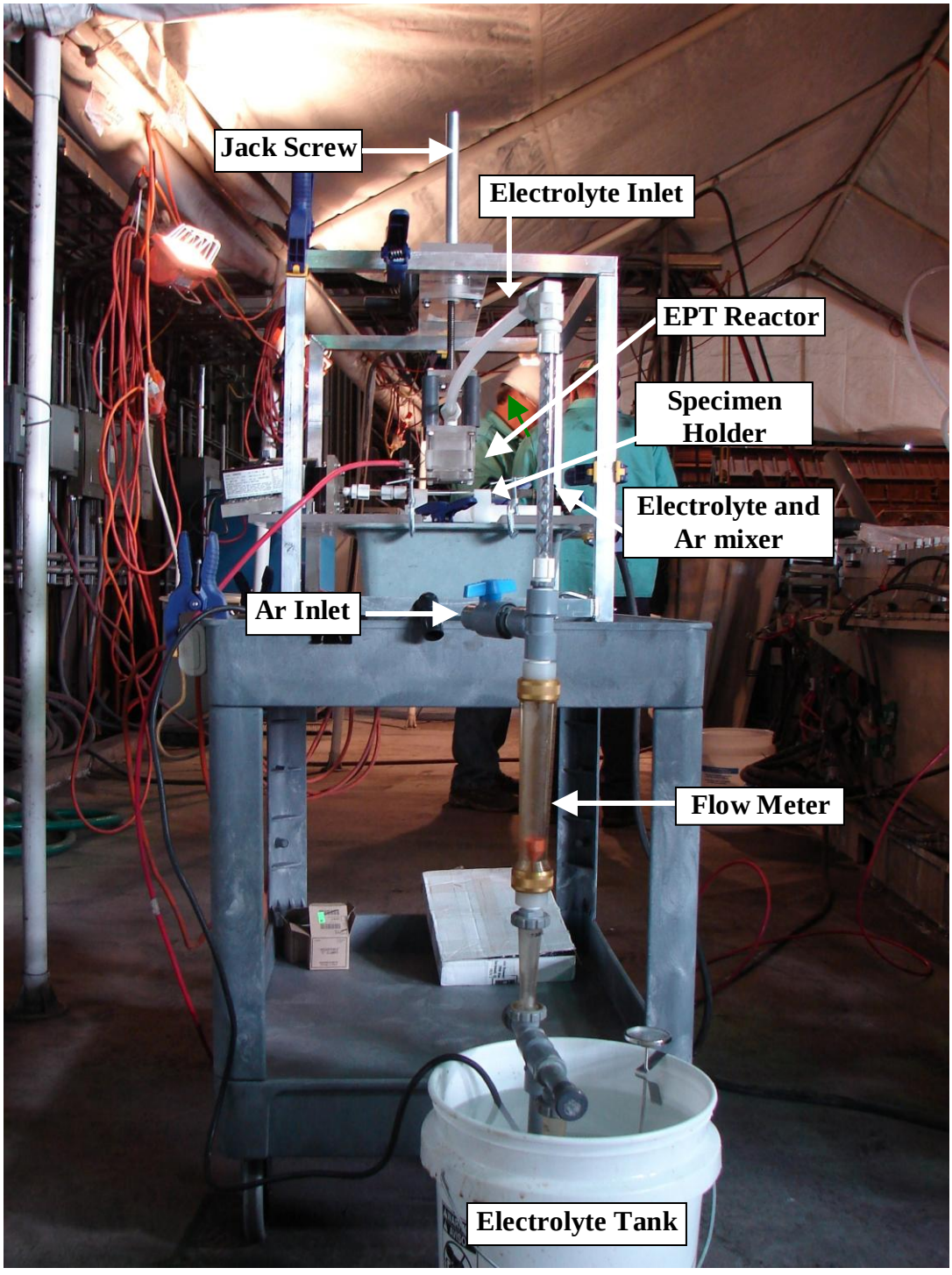

Figure 4.1 CAP Technologies EPT reactor that was designed to handle different type of specimens.

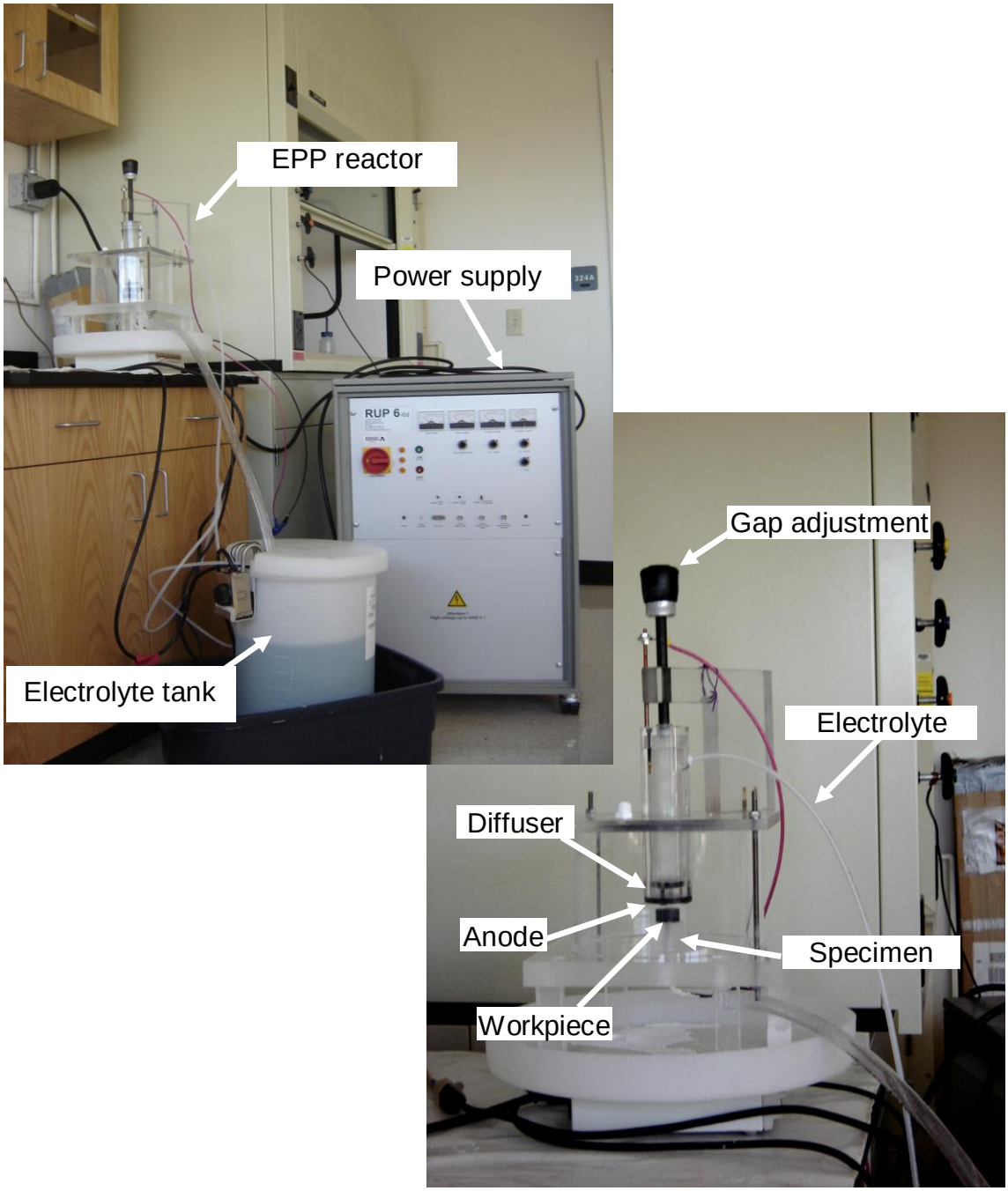

Figure 4.2 EPP reactor and setup built at UTA; right side image represents the close up view of the reactor.

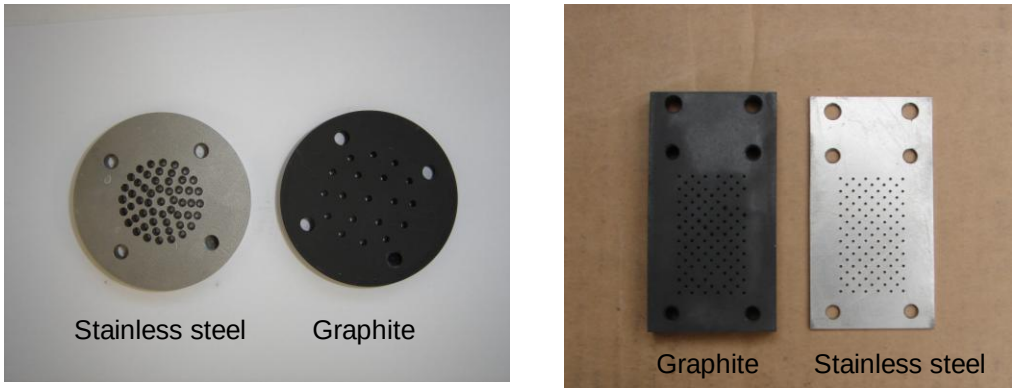

Figure 4.3 Design of anodes for processing flat samples.

4.3 Processing of Materials

The electrolyte used for cleaning processing was 12% $NaHCO_3$ aqueous solution maintained at a temperature of 75ºC. The cleaning conditions included: a voltage of 140V, current 12–15A, at processing time of 10, 20 and 30 seconds and constant electrode gap ~5 mm. For the given substrate size and current, the prevailing current density was ~3 A/cm^2. The selected substrate materials were all cleaned with the same electrolyte under the same conditions.

The coating procedure was performed on flat steel substrate polished down to 600 SiC grit paper. During processing, the power output was maintained constant. Coating processing conditions are presented in Table 4.2:

Table 4.2 Process parameters for EPP coating deposition:

Coating	Substrate	Electrolyte	Voltage [V]	Current [A]	Processing time [s]	T [ºC]
Zn	steel	16% $ZnSO_4$*7H_2O	170	15–20	30	75
Ni	steel	20% $NiSO_4$*6H_2O	200	10	30	75
Mo	steel	10% Na_2MoO_4	170	14–15	30	75

Coating was achieved by using an appropriate salt bearing the coating material. Since the anode was graphite, all depositing material was originated from the salt in the electrolyte. The electrolyte concentrations used are based on previous experience where EPP is producing the corresponding coatings under stable processing conditions. Even though a deposition rate comparison was not the objective of the present study, it should be noted that since the applied

current and electrolyte concentrations used differ in the three coatings, direct deposition rate comparison cannot be made, but it may be a contributing factor along with others in the coating characteristics.

Once the EPP process was completed, the specimen was removed from the electrolyte, washed in water and dried in compressed air. For the cross-section observations, samples were cut, mounted in epoxy, then ground and fine polished with 0.1 micron alumina as the final step.

4.4 Characterization of Produced Materials

Several complementary techniques were employed to characterize the cleaned and coated specimens.

4.4.1 Surface Morphology and Roughness Measurements

Optical interference profilometry [83] is a nondestructive, fast and precise method for characterization of surface morphology. A WykoNT9100 instrument was used in the present work. This instrument generates a topographic map of the surface by analyzing a set of fringes produced by the interference generated by a set of beams scanning the sample surface.

Measuring surface properties, such as surface roughness, skewness, flatness, etc., can be complicated, since many parameters contribute to a surface's behavior. The first industry-standard surface measurement statistics were developed to quantify the output of stylus profilers.

i. Standard Surface Roughness Measurements

Because stylus profilers make two-dimensional (2D) measurements, early roughness statistics, often referred to as R–parameters, were all 2D. Still in wide use today, the most commonly generated R–parameters are surface roughness R_a (average roughness), R_q (root mean square roughness), and R_z (an average of the maximum peaks and valleys). However, surfaces with similar average surface roughness values (R_a) sometimes actually have vastly different surface topographies. In order to better quantify these types of surface roughness measurements, for challenges such as film stress measurement, surface finish measurement,

and complex applications such as semiconductor etch measurement, industries are starting to develop three-dimensional (3D) standards.

ii. 3D Surface Metrology

3D surface metrology uses 3D surface profilers to provide non-contact measurement of surface features. These 3D surface profilers include white light based interferometric microscopes (optical profilers) and 3D confocal microscopes. Since the technology is non-contact, it is non-destructive, providing more repeatable and thus, more effective surface imaging and measurement. To characterize 3D surfaces, S–parameters have been developed by the ISO standards committee to replace the traditional 2D R–parameters. 3D surface metrology offers the opportunity to generate an enhanced measurement set for accurate quantitative interpretation. For example, the 3D S_{sk} parameter illustrates load carrying capacity, porosity, and characteristics of non-conventional machining processes. A surface that is smooth but covered with particulates has positive skewness, while a surface with deep scratches will exhibit negative skewness. In particular we are interested in the volume of any projections or holes that can be measured with 3D imaging.

4.4.2 Scanning Electron Microscopy

Surface morphology analysis of the processed materials was conducted using Scanning Electron Microscopy (SEM). A typical voltage of 10 keV - 25 keV was used. Surfaces were examined to obtain different characteristics related to morphology. Of special interest were the shape, size and distribution of surface features, from the more simple shapes such as valleys and nodules, to more complicated ones present in coating surfaces. Those features may be attributed as surface characteristics for a given processed material, and would be the first indication on how processing was dynamically interacting with the surface. Those features were later compared with profilometry results.

More details can be revealed by cross-sectional SEM analysis. Interfaces, coatings thickness and porosity were examined. Carbon tape was used to contact the metal samples in the epoxy-mounted cross-sections to avoid charging.

The extent and the microstructure of the affected layer (for cleaning) and interaction coating-substrate layer (for coating) were examined. Energy-dispersive X-ray spectroscopy (EDS) in conjunction with SEM was employed to evaluate the elemental composition of the aforementioned layers and coatings. It is known that X-ray penetration depth is a factor that cannot be avoided in these studies; therefore the resulting composition maps study should considered this factor.

Backscattered Electron image provides a better contrast for heavy elements, such as Mo, present in one of the coatings. This mode is particularly useful when phases with heavy and light elements are present.

4.4.3 Transmission Electron Microscopy

More detailed observations of the microstructures were performed using a JEOL 200CX TEM. It was used to observe and study details in the produced microstructures, such as the characteristic interfaces that formed between the substrate and the coating. Fine grains, sub-micron size, and interfaces tens on nanometers wide were observed using bright field and dark field imaging. Electron Diffraction (ED) patterns from the areas of interest were acquired, d_{hkl} spacing calculated, and diffraction spots indexed by comparing them with standard values for phase identification.

High resolution TEM (HRTEM) coupled with Fast Fourier Transformation (FFT) was used to obtain the image of the crystallographic structure at the atom scale. It is an invaluable tool for phase identification at the small substrate – coating interface.

Prior to TEM analysis, thin foils were prepared from the cross-sectional area of EPP–processed samples using Focused Ion Beam (FIB) micro-sampling (also known as lift-off technique). Micro-sampling is a technique that allows the extraction of a TEM–usable sample from bulk specimens, using an ion beam and a microprobe inside the FIB chamber.

FIB is a technique used for site-specific analysis, deposition, and ablation of materials. FIB setup is a scientific instrument that resembles an SEM. However, while the SEM uses a focused beam of *electrons* to image the sample in the chamber, FIB setup instead uses a focused beam of *ions*. FIB can also be incorporated in a system with both electron and ion beam columns, allowing the same feature to be investigated using either of the beams. Gallium is the most widespread ion source. Unlike an electron microscope, FIB is inherently destructive to the specimen. When the high-energy gallium ions strike the sample, they will sputter atoms from the surface. Gallium atoms will also be implanted into the top few nanometers of the surface.

Because of the sputtering capability, the FIB is used as a micro-machining tool, to modify or machine materials at the micro- and nanoscale, an ideal FIB might machine away one atom layer without any disruption of the atoms in the next layer, or any residual disruptions above the surface [85, 86].

FIB can also be used to deposit material via ion beam induced deposition. FIB-assisted chemical vapor deposition occurs when a gas, such as tungsten hexacarbonyl, $W(CO)_6$, is introduced to the vacuum chamber and allowed to be chemisorbed onto the sample. By scanning an area with the beam, the precursor gas will be decomposed into volatile and non-volatile components; the non-volatile component, tungsten, remains on the surface as a deposition. This is useful, as the deposited metal can be used as a sacrificial layer, to protect the underlying sample from the destructive sputtering of the beam.

FIB is also commonly used to prepare TEM samples from selected areas, Figure 4.4. First step is to deposit a tungsten thin film by FIB-assisted chemical vapor deposition, Figure 4.4(a). This metallic film is used as a sacrificial layer to protect the underlying sample from the destructive sputtering of the beam. By pattern etching, a sample of desired size is carved out of the substrate, Figure 4.4(b). A probe (or specimen carrier) is attached to the sample by metal deposition around its tip, Figure 4.4(c). Then, the sample is released from the substrate by etching off the anchor, Figure 4.4(d), transported to specimen stub and attached by metal coating to the stub, Figure 4.4(e). The probe is removed by etching its tip near the point of contact with

the sample, Figure 4.4(f). Figures 4.4(g) and 4.4(f) show the sample attachment procedure to the stub, and the sample ready to be FIB – thinned to the required size for TEM analysis (~100 nm).

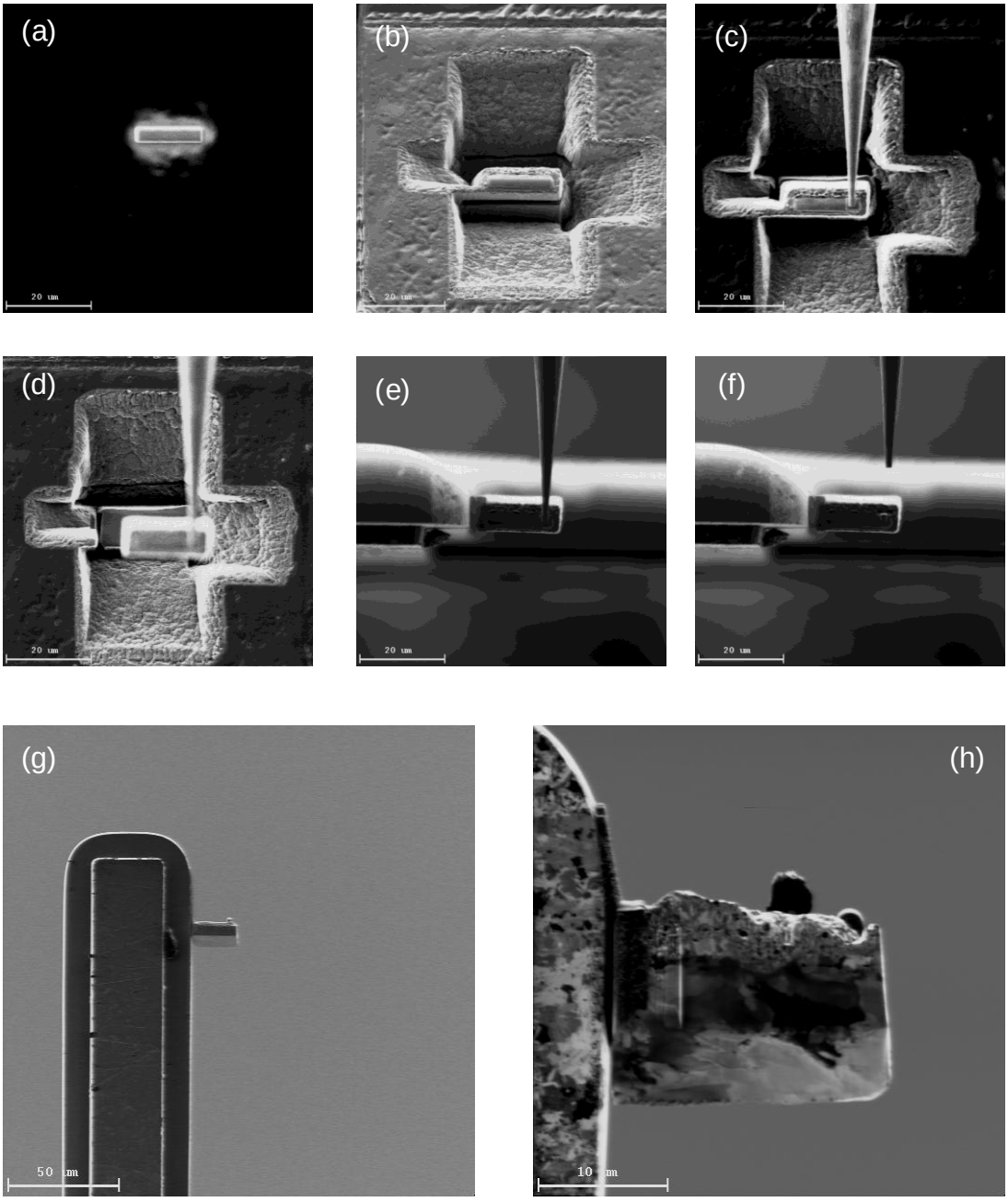

Figure 4.4 TEM micro sample prepared with Hitachi FB-2100 System, (a) metal coating, (b) specimen creation, (c) specimen pick-up using microprobe, (d) specimen transportation, (e) fixation on specimen stub, (f) microprobe release, (g) and (h) specimen cross-section before thinning.

It should be mentioned that sometimes the FIB-thinning does not go far enough and the TEM sample will prove to be too thick when studied. There was such an instance with two of the present samples In order to decrease further the sample thickness for usable TEM analysis, 2-3min of ion milling was applied to those samples.

4.4.4 X-ray Diffraction

The phase structure of the EPP–treated samples was studied using a Siemens D500 X-ray diffractometer operated in the Bragg-Brentano mode. This technique was used to obtain information on the crystalline structure, texture, grain size and residual stresses.

For cleaning, the top processed layer was studied for grain size and residual stress determination. The intensity diffraction signal from the thin substrate/coating interface is expected to be too weak to allow analysis by this technique. Similarly, XRD was used for the coatings to study grain size, texture and residual stresses.

A Cu K_α radiation source (λ_{Cu} = 0.154 nm), with accelerating voltage and filament current of 40 kV and 30 mA, were be used to perform θ - 2θ angle scans. Peak fitting was then applied to the resulting diffraction pattern using a search method with a database search application (Jade platform), and from the position of the peaks compared to a reference pattern (Powder diffraction file – PDF), phases could be identified for the best fit of overlapping patterns.

The approximate size of crystalline grains, d, was then calculated by analyzing peak width as the full width half maximum intensity (FWHM) which can be correlated to crystallite size according to the Scherrer formula [87].

$$d = \frac{0.9\lambda}{B\cos\theta} \tag{4.1}$$

where B is the FWHM of the diffraction peak, and θ is half of the diffraction angle. Meanwhile, the penetration depth (Dθ) of x-rays at different glancing angle (α) can be calculated by the expression:

$$D_0 = 2\sin(\alpha)/\sin(22.5) \tag{4.2}$$

Similarly, glancing angle XRD was employed to determine residual stresses as a result of EPP processing. First, interplanar spacing was obtained from the positions of the diffraction peaks using Bragg's law. The interplanar distance and grain size at different distance from the surface are then calculated and plotted. Zhang et al [88] proposed that the stress, σ, in films can be obtained using glancing angle XRD by

$$\sigma = -\frac{E}{\nu}\Delta l \tag{4.3}$$

where $\Delta l = (l - l_0)/l_0$; E and ν are the Young's modulus and Poisson's ratio, respectively; l_0 is the distance of the unstressed *hkl* plane, l represents the distance of the stressed *hkl* plane in the direction normal to the sample surface, which is defined as:

$$l = \frac{d_{hkl}}{\cos(\theta - \alpha)}, \tag{4.4}$$

where d_{hkl} is the d-spacing of the diffracted *hkl* plane and α is the x-ray incidence angle. From this equation, it can be seen that the larger interplanar spacing in the near surface region indicates the presence of a higher compressive stress, and the decrease of interplanar spacing implies a reduction of compressive stresses with depth. However, it is difficult to calculate the internal stress at different depth since it is hard to determine the value of l_0.

In order to investigate the existence of a compressive stress and obtain qualitative information about the internal stress in the EPP-treated surface layer, the standard $d_{hkl}(\psi)$ versus $sin^2(\psi)$ method was used. A high order diffraction plane with a relative high intensity is used for the stress measurements due to its high diffraction angle. During measurement, the specimen surface is tilted 0-30° (ψ angle) and a θ-2θ scan was conducted in the 2θ range. The calculated $(d_\psi - d_0)/d_0$ *vs* $sin^2(\psi)$ is plotted. For cubic structures, the stress (σ) in a thin layer in a state of equi-biaxial stress could be computed according to the $sin^2(\psi)$ method by the following equation [89]:

$$\frac{d_{hkl}(\psi) - d_0}{d_0} = \sigma\left[\frac{1+\nu}{E}\sin^2(\psi) - \frac{2\nu}{E}\right], \tag{4.5}$$

where d_0 is the stress-free lattice parameter, $d_{hkl}(\psi)$ is the lattice spacing measured with the surface tilted at ψ angle, ν and E are the Poisson's ratio and elastic modulus. The internal stress in the surface layer can be calculated from this equation after obtaining the slope of the $(d_\psi - d_0)/d_0$ vs. $sin^2(\psi)$.

CHAPTER 5

MICROSTRUCTURAL EVOLUTION OF NEAR-SURFACE LAYERS DURING EPP CLEANING PROCESSES

In the present work, a rigorous study of the EPP process was undertaken. To our knowledge, there is no comprehensive study to date on the plasma – surface interaction during EPP in the literature. Therefore, the main objective is to address the lack of fundamental knowledge on the EPP by investigating and building an understanding of the surface layer formation under plasma action. This objective was approached through studying the two main components of EPP considered to be major candidates for practical applications: first, cleaning (the process of substance removal and modification of the substrate surface and second, coating (deposition of a material on a given substrate under plasma action). Characteristics such as surface features, topography, microstructure and composition of the near-surface layer produced by EPP were correlated with material properties in such a way that allow extrapolations to a large variety of candidate materials for substrate processing or coating deposition.

Surface topography analysis deals with the three-dimensional representation of surface features and characteristics. At this point, the focus is on the characteristic features produced by the surface-plasma interaction. These features can be described as “peaks” and “valleys” and their characteristics (size, spacing, shape, etc.) are expected to be influenced by the material properties.

An optical surface profiling system (WykoNT9100) was used and 3D scanning data were acquired for a systematic study using statistical analysis [90, 91]. The expectation was that the surface texture produced by plasma - material surface interaction is a “fingerprint” of the

processing environment (plasma parameters) and nature of substrate material. For each of the three substrate materials involved in this study, three processing times – 10, 20 and 30 seconds were used. The shorter (10 s) time is representative of that pertaining during typical processing. The longer treatment time (30 s) was selected to be able to study evolution of "steady-state" morphologies. Optical profilometry scans were performed over the entire treated specimen surface and the data sets collected were averaged to determine their statistical significance. Similar earlier studies on the surface profile characteristics produced in fracture surfaces have been performed by Underwood et al. [92].

5.1 Surface Morphology

Surface morphology characterization of the processed materials was first conducted using SEM. A typical accelerating voltage in the range of 10 keV - 25 keV was used to acquire top-view micrographs that reveal the evolution of the surface morphology with processing time. The sequence of these micrographs is represented in Figures 5.1 to 5.3 for all three substrates. Steel substrate shows well formed, round hills of around 0.5 – 1.0 μm size, separated by valleys. Similar observations were reported previously in the literature [27]. The micrographs show a progressive development of random distribution of hills and valleys with processing time. A longer duration treatment involves the result of numerous melting and freezing events on the surface. Following the very first events, surface appearance will be strongly influenced by the electrode and unprocessed surface profile. Looking at the "steady-state" it is evident that the material properties play a key role in the evolution of the surface features.

Steel maintains/develops a rather nodular type of hills, whereas hills in Al are rather flat and grow in plane with processing time. The Ti features posses a different characteristic, more "tortuous". Further it looks like T_M may not be the only material property in determining this morphology (i.e., steel and Ti both have high T_M but entirely different surface morphologies).

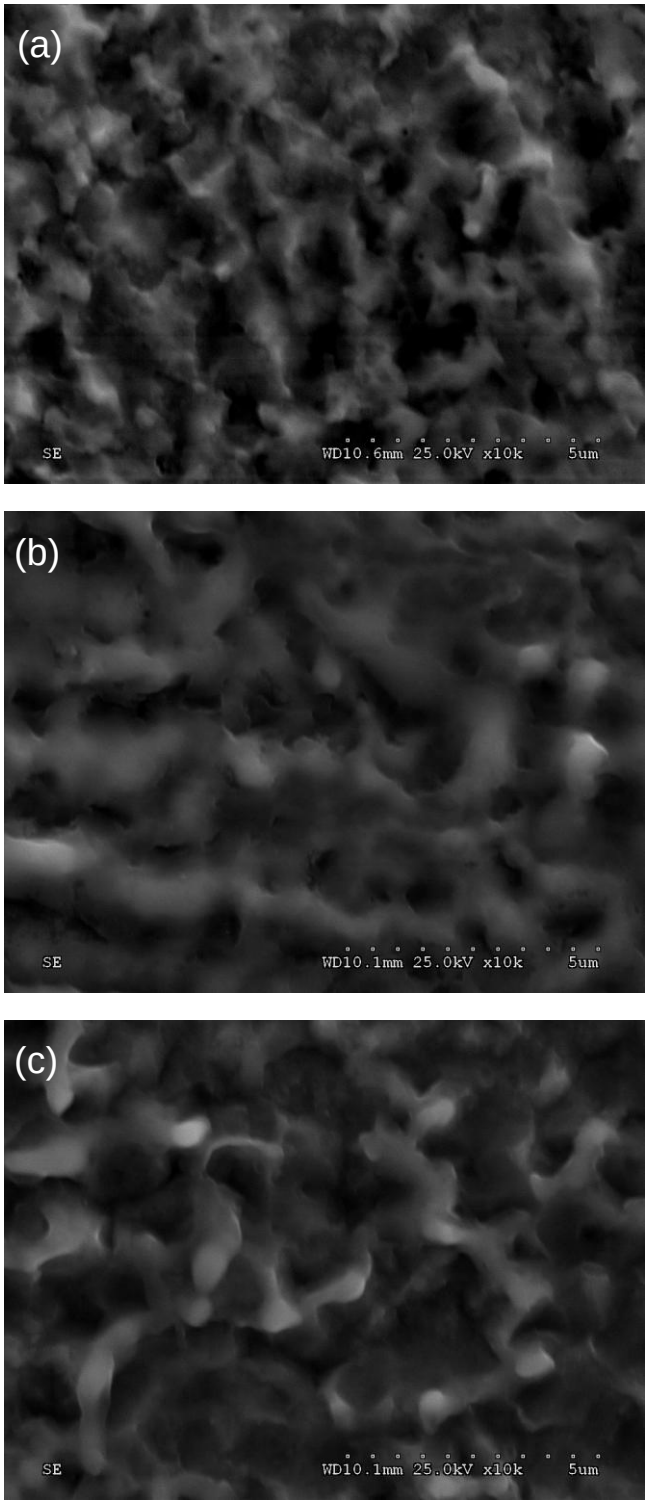

Figure 5.1 Top surface SEM micrographs of EPP-treated low carbon steel at different processing times of (a) 10 s (b) 20 s, and (c) 30 s.

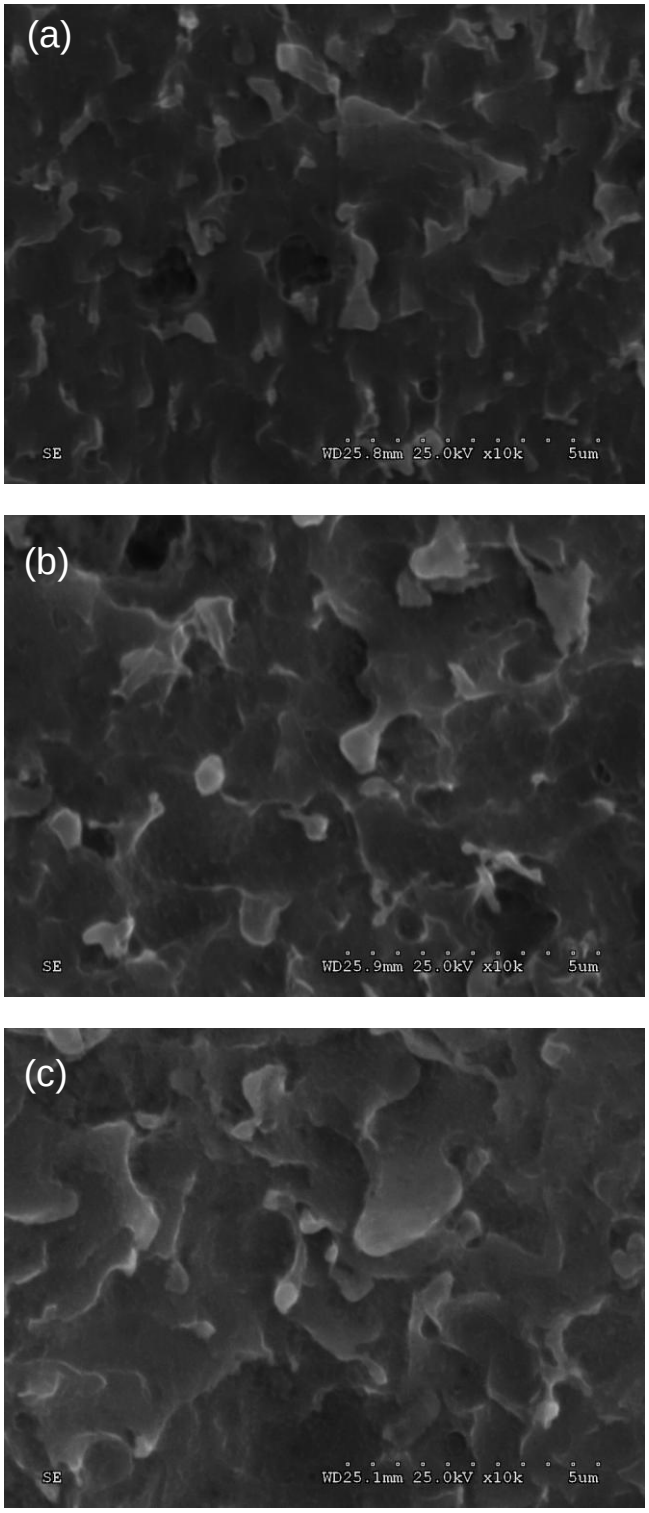

Figure 5.2 Top surface SEM micrographs of EPP-treated 1100 Al at different processing times of (a) 10 s (b) 20 s, and (c) 30 s.

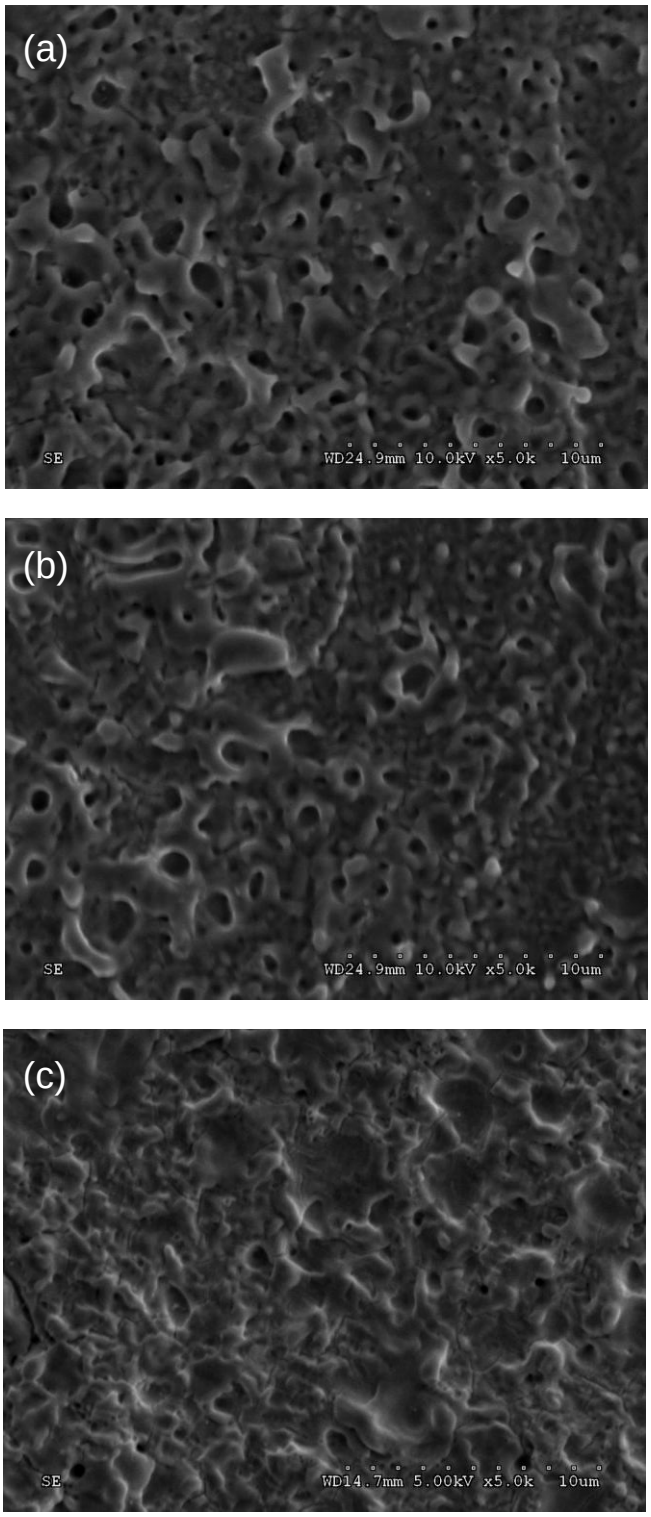

Figure 5.3 Top surface SEM micrographs of EPP-treated pure Ti at different processing times of (a) 10 s (b) 20 s, and (c) 30 s.

5.2 Surface Topography Analysis

Methodologies have been developed to characterize surface topography in a quantitative manner. Such techniques for example have been extensively used to describe fracture surfaces [92, 93, 94].

The parameters that characterize the overall morphology of a surface are:

R_a – represents the roughness average, the arithmetic mean of the absolute values of the surface departures from the mean plane; the approximation for three-dimensional R_a is

$$R_a = \frac{1}{MN}\sum_{j=1}^{M}\sum_{i=1}^{N}\left|Z_{ji}\right| \tag{5.1}$$

where M and N is the number of data points in the X and Y direction, respectively, of the array, and Z is the surface height relative to the reference mean plane [95].

A disadvantage of average roughness is that it cannot detect differences in spacing of surface irregularities (peaks and valleys) not it can give information as to their shape.

R_q – represents the root mean square roughness, obtained by squaring each value in the dataset, then taking the square root of the mean;

$$R_q = \sqrt{\frac{1}{MN}\sum_{j=1}^{M}\sum_{i=1}^{N}Z^2\left(x_i, y_j\right)} \tag{5.2}$$

Rq represents the standard deviation of the surface heights, and is used in more complex computations like skew.

Rz – represents the average maximum height of the profile, and is calculated as the average of the ten highest and ten lowest points in the dataset.

$$R_z = \frac{1}{10}\left[\sum_{j=1}^{10}H_j - \sum_{j=1}^{10}L_j\right] \tag{5.3}$$

where H_j are the highest points and L_j are the lowest points found in the dataset.

The advantage of R_z over a single peak-to-valley height is that it reduces the effects of odd scratches or non-typical irregularities.

R_{sk} – skewness, measured the asymmetry of the surface about the mean plane.

$$R_{sk} = \frac{1}{NMR_q^3} \sum_{j=1}^{N} \sum_{i=1}^{M} Z_{ij}^3 \quad (5.4)$$

Skewness takes many equally spaced profile heights in a sampling length into account. Skewness is like a mean-curbed roughness. Points farther from the mean surface level when raised to powers of 3 and higher have proportionally more weight than those closer to the mean surface level. The sign of the skewness will indicate whether the farther points are proportionally above (positive skewness) or below (negative skewness) the mean surface level. Thus, the predominance of bumps or peaks on a surface will have a positive skewness ($R_{sk} > 0$) and predominance of holes or valleys in a surface will have a negative skewness ($R_{sk} < 0$).

R_{ku} – kurtosis, measures the peakedness of the surface about the mean plane.

$$R_{ku} = \frac{1}{NMR_q^4} \sum_{j=1}^{N} \sum_{i=1}^{M} Z_{ij}^4 \quad (5.5)$$

R_{ku} provides information about the “spikiness” of a surface, or of the sharpness of the amplitude density function, which does not necessarily mean the sharpness of individual peaks and valleys, but rather the nature of the height distribution. Therefore, it is useful for indicating the presence of either peak or valley defects such as scratches. Kurtosis values can range from 0 to 8. If the surface heights are normally distributed (Gaussian or random distribution) then $R_{ku} = 3$. Surfaces composed of inordinately high peaks / deep valleys have $R_{ku} > 3$. Surfaces with fewer high and low extreme points than a Gaussian surface have $R_{ku} < 3$.

Figure 5.4 represents the variation of R_a as a function of processing time for all three substrates. The data shows that R_a for Ti and Al is similar and significantly higher than that of steel. R_a is in general decreasing with processing time. In addition, Ti and Al exhibit a different trend compared to steel. The R_z (Figure 5.5) also confirms the above roughness trend although these two parameters show insensitivity for differentiating between peaks and valleys.

In this aspect, of greater use is skewness R_{sk} (Figure 5.6), that compares the degree of symmetry of the surface heights about the mean plane. Figure 5.6 shows that for Al, $R_{sk}<0$, indicating the preponderance of valley structure independent of processing time. Rsk for steel

hovers around the equilibrium of peaks / valley texture (20s, 30s) while for Ti, R_{sk}>0, indicating the dominance of peaks on the substrate surface.

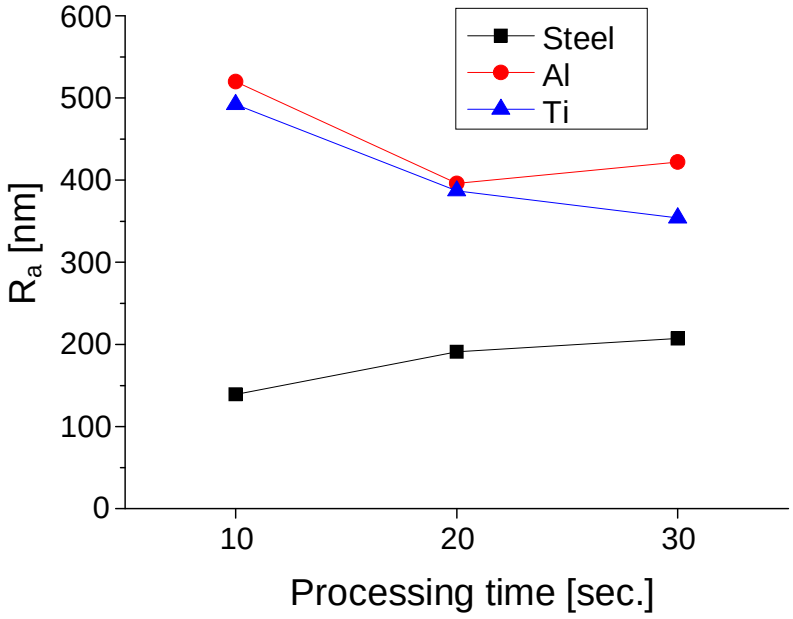

Figure 5.4 R_a as a function of processing time.

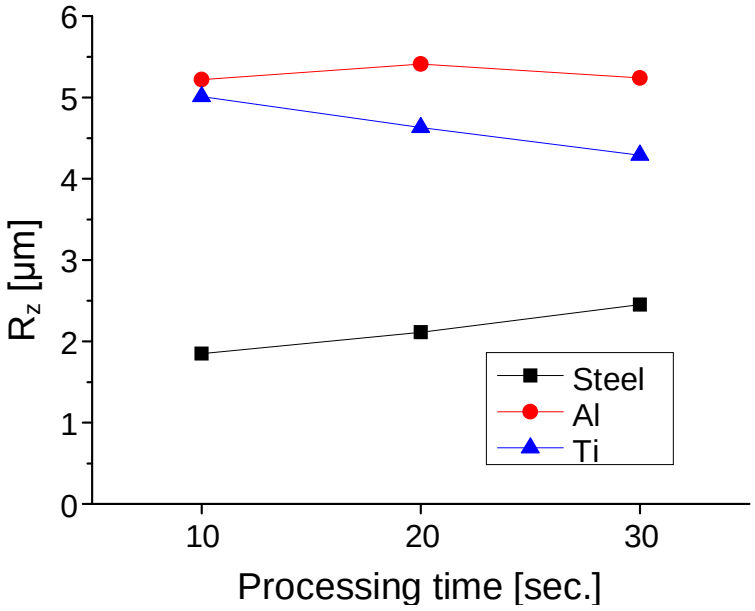

Figure 5.5 R_z as a function of processing time.

Kurtosis (Figure 5.7) indicates the nature of the height distribution, with a remarkable consistency for Ti versus processing time and a significant change for Al at increased processing

time suggesting Al will sustain a greater amount of deep irregularities, initially observed on SEM surface micrographs (Figure 5.2). For the steel substrate, there is a significant stabilization with increased processing time, the surface texture approaching that of Ti.

In order to obtain information on the shape and size of peaks and valleys, parameters from the functional volume family were analyzed.

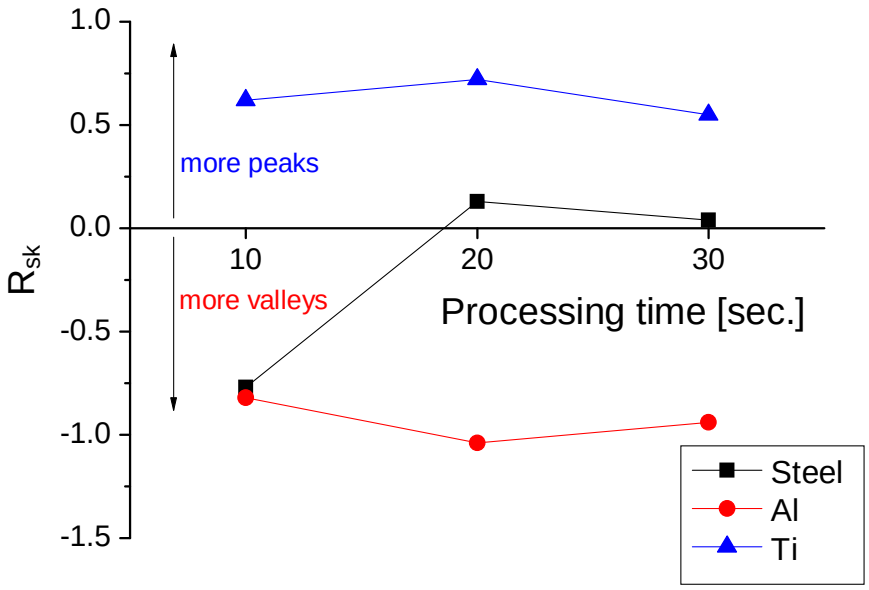

Figure 5.6 Skewness of 3D surface texture in plasma-surface interaction for Steel, Al and Ti.

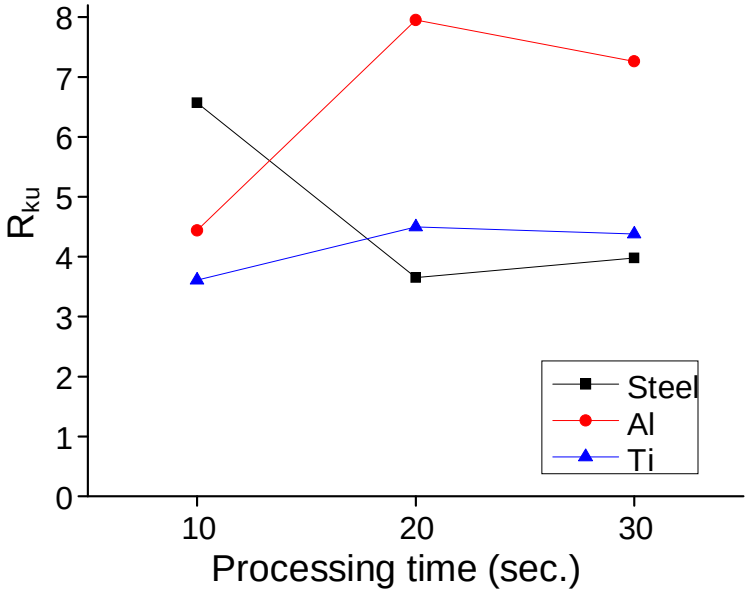

Figure 5.7 Kurtosis of 3D surface texture in plasma-surface interaction for Steel, Al and Ti.

5.3 Volume Parameters

Volume parameters (Sm, Sc, Sv) provide information on the volume of material or space filling the surface structures. Since they are calculated relative to the cross-sectional area of the measurement, they have units of volume/area ($\mu m^3/\mu m^2$). Volume parameters are derived from the bearing area analysis of the complete 3D surface. The bearing area curve (Figures 5.8 and 5.9) is formed by establishing the amount of material a plane would rest on relative to the complete cross-section of the surface for each height from the highest to the lowest point of the surface [96].

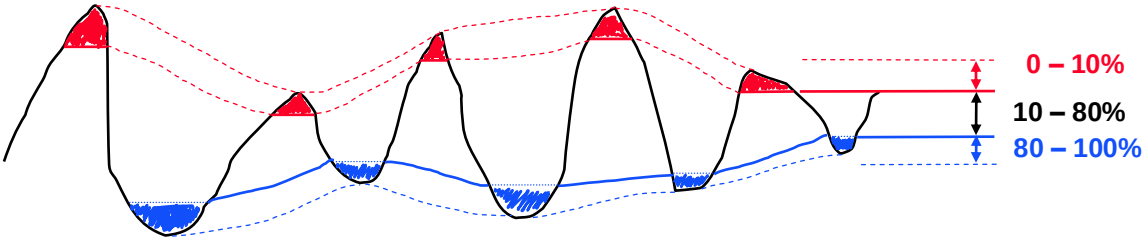

Figure 5.8 Volume of material contained in the bearing area (%) for Sm, Sv and Sc.

Sm – Surface Material Volume, is the amount of material contained in the surface peaks from 0% to 10% of the bearing area ratio.

Sc – Core Void Volume, is the volume (for example, of a fluid filling the core surface) that the surface would support from 10% - 80% of the bearing ratio.

Sv – Surface Void Volume, is the volume (for example, of a fluid filling the valleys) that the surface would support from 80% - 100% of the bearing ratio.

In addition, there are another series of parameters, Sbi, Sci and Svi, part of the functional index family. They are all unit-less parameters.

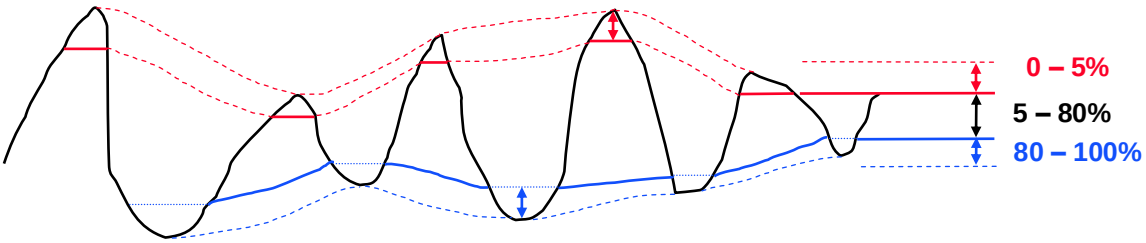

Figure 5.9 Height of material contained in the bearing area (%) for Sbi, Sci and Svi.

Sbi – Surface Bearing Index, is a measure, relative to Rq, of the surface height at 5% bearing area ratio.

Sci – core fluid Retention index, is a measure, relative to Rq, of the volume (for example, of a fluid filling the core surface) that the surface would support from 5% – 80% of the bearing ratio.

Svi – Valley Fluid Retention Index is a measure relative to Rq of the volume (for example, of a fluid filling the valleys) that the surface would support from 80% to 100% of the bearing ratio.

Another parameter was introduced here, that combines information regarding the density of peaks per unit area, which allows a quantitative measure of the mechanism of formation for peaks and valleys.

Sds – Summit Density, is the number of summits per unit area that make up the surface. Summits are derived from peaks:

$$S_{ds} = \frac{Number - of - peaks}{Measured - Area} \qquad (5.6)$$

5.4. Discussion

At this point, the size and shape of peaks and valleys is compared relative to the type of substrate material. A peak or valley is considered as an egg shaped structure characterized by a height and a cross-sectional area.

The volume parameters, Sm, Sc and Sv, are used to quantify the 3D shape height x cross-section of peaks/valleys and the Sbi, Sci and Svi only for cross-section of the egg-shaped structures. Since this is a qualitative comparison between the three materials (steel, Al, Ti), the quantities related to those parameters will result in a 3D peak to be tall - short and thick - thin and a 3D valley being deep-shallow and wide-narrow. Moreover, Surface Parameters Analysis were employed to analyze the steady-state processing (for processing time of 30 s) from the perspective of what was considered principal material characteristics for the surface formation, the melting temperature.

Steel features:

Figure 5.10 to 5.12 show that steel has *average* cross-section values (between the extremes Ti and Al) for both peaks and valleys, and the lowest Sc represents *short* peaks and *shallow* valleys, which is in agreement with the Ra and Rz, Figure 5.4 and 5.5.

The Sds variation with processing time, Figure 5.13, shows that there is a clear separation between steel and Ti. This parameter is the only one that may explain why there is no apparent direct correlation between T_M and volume of peaks – valley of steel and Ti, Figure 5.14. The steel substrate exhibits four times more peaks per unit area than Ti, and smaller peaks indicates less measured molten volume. This is the reason that although steel has larger available cross-sectional area of peaks/valleys (larger Sbi and Svi) the total volume is lower.

Al features:

Figure 5.10 to 5.12 show that Al has the highest Sbi and Svi but lowest Sci, which represents *tall*, *narrow* peaks and *deep*, *wide* valleys. Compared to Ti, what Al loses in peak volume is compensating by valley volume for an equal amount of Sc on average to Ti. For Al, skewness (Figure 6) shows an imbalance toward valleys versus peaks surface coverage. SEM micrographs also show a leafy type peaks and large valleys.

Sm=22 << Sv=73, since T_M (Al) is low, it is easily melted which explains the skewness results, with more valleys than peaks.

Svi = 0.13 << Sbi = 0.68 which shows that peaks are much wider than valleys. This suggests that high temperature plasma interacting with the surface has a high penetration depth and carves the substrate leaving behind a deep, narrow cavity, while the freezing of molten droplets builds upon previous ones forming a volcanic-type dome with a wider base.

Short, wide peaks are influenced by the freezing kinetics of molten droplets. Higher melting temperature results in a more viscous molten metal that will not travel much and will remain rather close to the cavity, freezing fast and forming the plate-like shape peaks. In addition,

since penetration depth for plasma is short, melting occurs directly at the top surface and the result will be a shallow, wide valley.

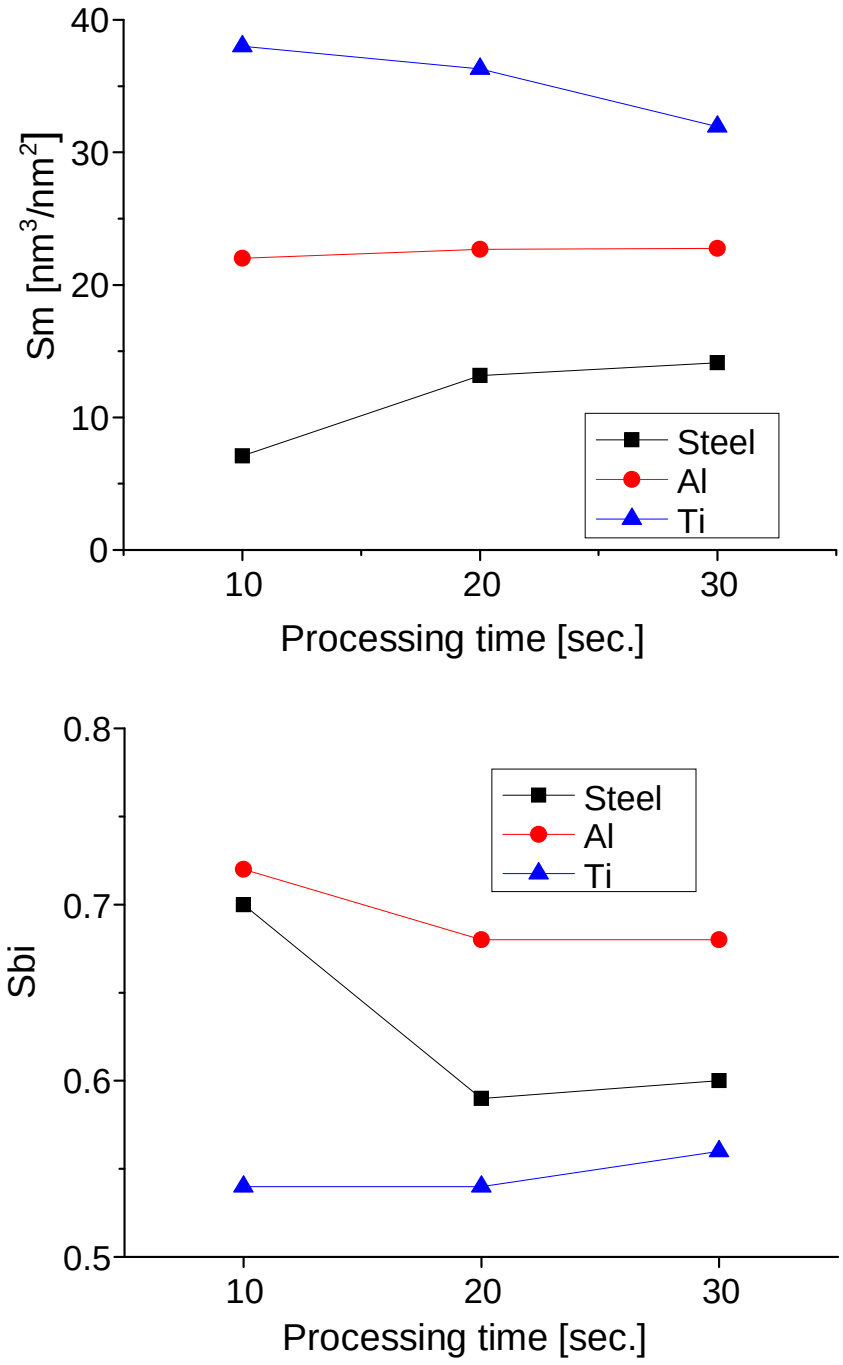

Figure 5.10 Sm and Sbi for steel, Al and Ti substrate peak analysis.

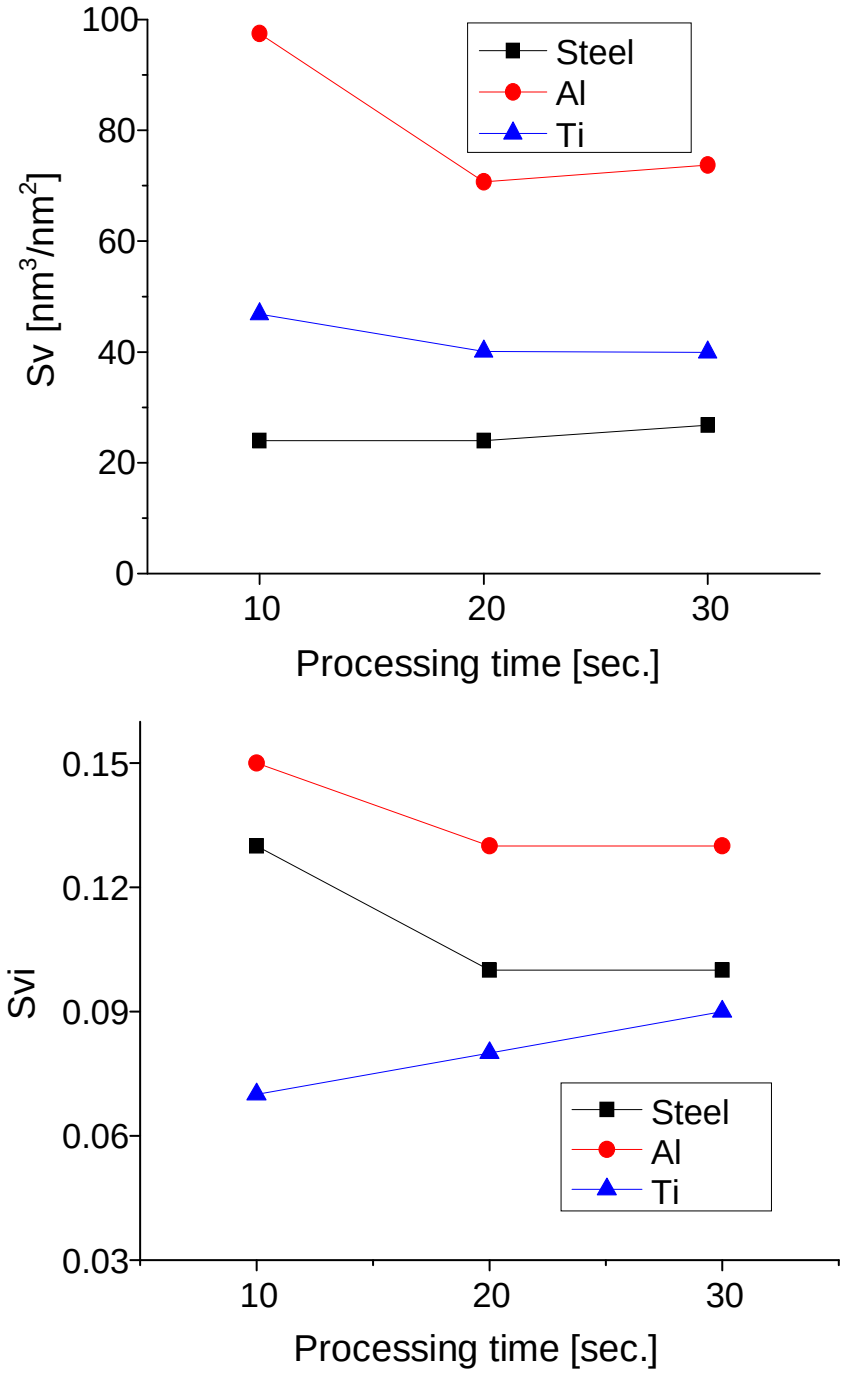

Figure 5.11 Sv and Svi for steel, Al and Ti substrate valley analysis as a function of time.

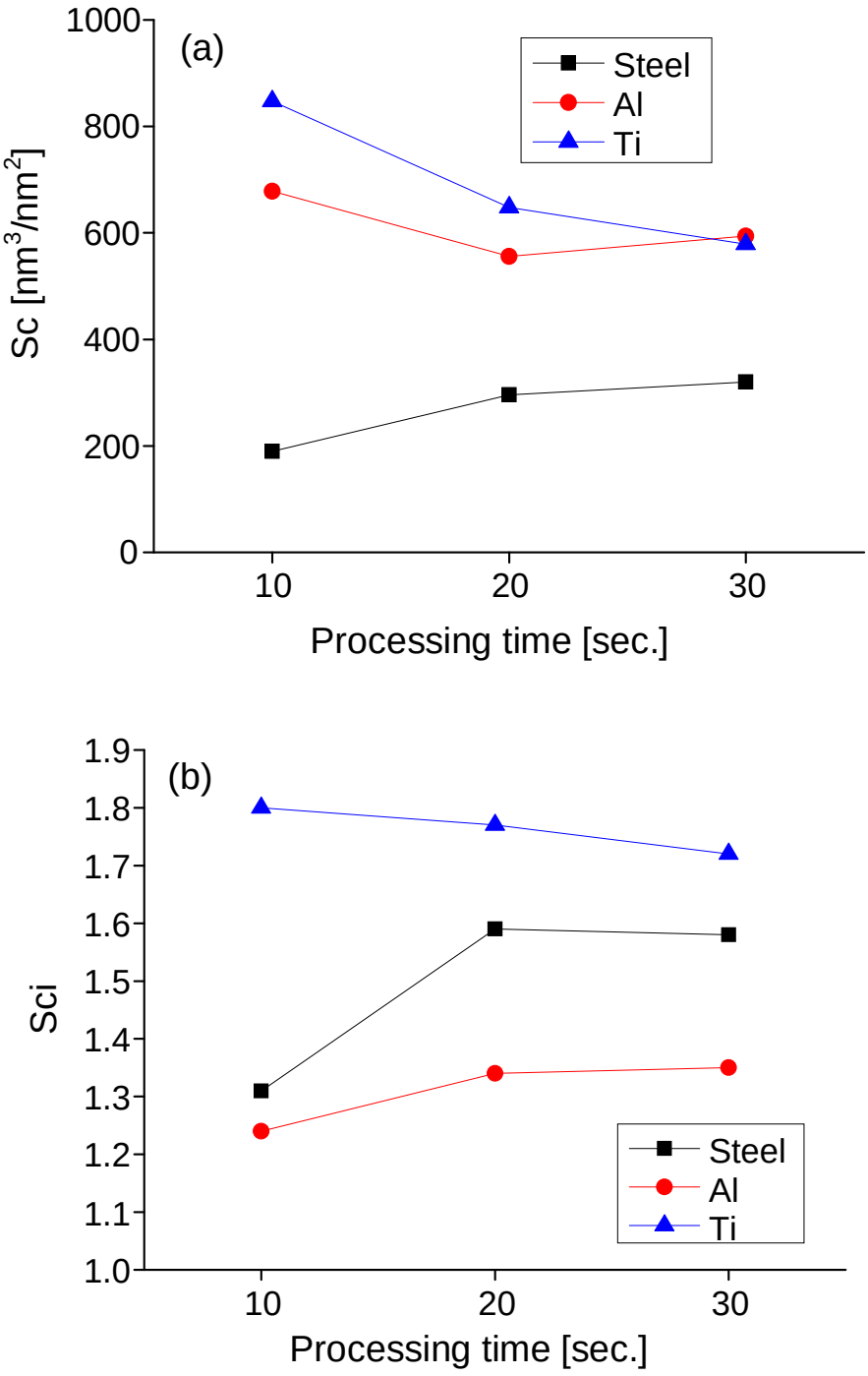

Figure 5.12 Sc and Sci as a function of processing time for steel, Al and Ti substrate (a) volume analysis and (b) core cross-section.

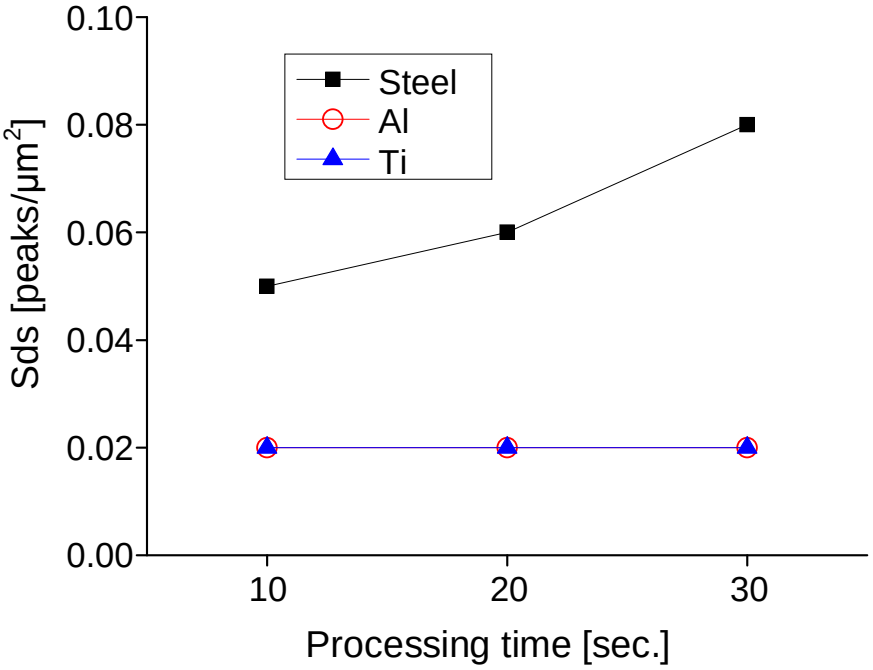

Figure 5.13 Summit densities Sds for steel, Al and Ti substrate.

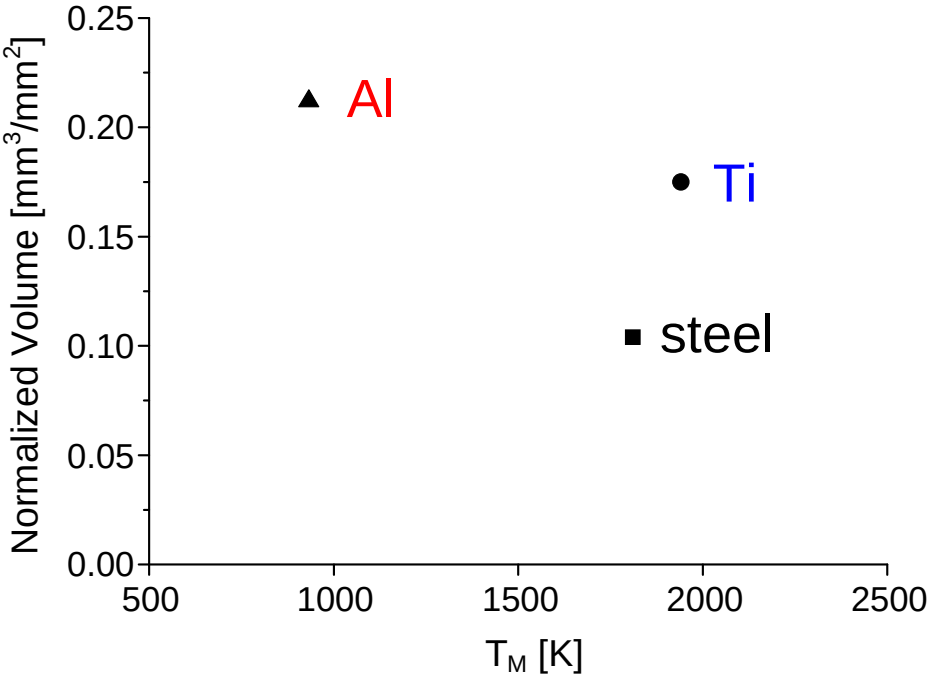

Figure 5.14 T_M vs. normalized molten volume for steel, Al and Ti substrate – plasma interaction.

Ti features:

It is evident from Figure 5.10 to 5.12 that Ti has the lowest Sbi and Svi but the highest Sci. Its peaks are *short* and *thick* and its valleys are *shallow* and *wide*, which is consistent with the SEM surface morphology observations showing plate-like structures (Figure 5.1 to 5.3).

Ti features. Sm=32 ~ Sv = 40, since T_M (Ti) is high, melting is more difficult but freezing/deposition is faster, and the balance valleys – peaks moves toward the latter.

5.5 Thermodynamic Considerations

There can be another approach to the surface solidification during processing, and that involves surface energy. Calculations for the surface energies [97–99], Table 5.1, allow comparisons of these values for steel, Ti and Al.

Table 5.1 Surface energies of substrate materials [99].

Physical Properties		Fe	Ti	Al
Average surface energy [J/m^2]		2.45	2.0	1.15
Surface Energy [J/m^2]	γ_{SV}	2.206	1.800	1.032
	γ_{SL}	0.326	0.266	0.154
	γ_{LV}	1.830	1.493	0.865
	$\Delta\gamma_{\infty}$	-0.050	-0.041	-0.013

The average surface energy of Fe is significantly higher than Ti and Al, which suggests there is a difference in the rate of nucleation and growth during surface solidification. Such surface energy difference also suggests differences in the shape of the solidified material after localized plasma-induced melting. Indeed, as Figures 5.1 to 5.3 show, steel possessing a higher surface energy exhibits nodular hills compared to rather flat hills in Al and Ti.

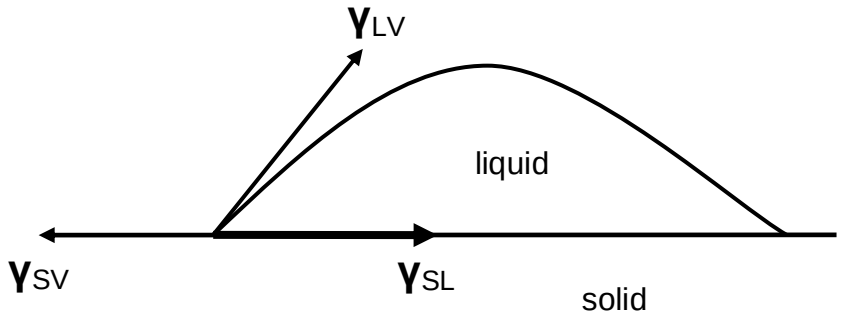

Figure 5.15 Balance of surface tensions during surface melting.

From the thermodynamic point of view [99], the free energy difference is dominated by short-range forces represented by the $\Delta\gamma_\infty$ term during solidification on a solid surface. Figure 5.15 gives:

$$\Delta\gamma_\infty = \gamma_{SL} + \gamma_{LV} - \gamma_{SV} \qquad (5.7)$$

where γ_{SL}, γ_{LV}, γ_{SV} are the surface energy components with respect to S – solid, L – liquid, V – vapor phases.

The value of $\Delta\gamma_\infty$ determines the melting behavior of the system, with $\Delta\gamma_\infty > 0$ is the non-wetting condition. It can be seen from Table 5.1 that $|\Delta\gamma_\infty(Fe)| > |\Delta\gamma_\infty(Al)|$ by a factor of 4, which suggests that steel will tend to form round nodules whereas Al wets the surface and tends to spread laterally, consistent with the SEM evidence. In this regard, Ti behavior is somewhat similar to steel, given the close value for $\Delta\gamma_\infty$.

An analysis of the physical properties for the three substrate materials was conducted in an effort to correlate molten mass of material at the surface with thermal properties. After considering various combinations of thermal properties, the analysis suggests that there is an inverse proportionality between heat of fusion and molten mass (Table 5.2).

Using H_f values from the literature (Table 5.2) and molten mass quantities estimated from the profilometry measurements, the amount of thermal energy for melting at the top surface layer can be approximated. As noted, only the mass of “nodules” was considered for the analysis as the molten mass from the process. The calculation shows that:

The thermal energy required to raise the substrate material mass (m) to T_M and subsequently melt is given by:

$$Q = m * Cp(T) * \Delta T + m * H_f \quad (5.8)$$

where Cp – heat capacity [J/kg*K], m - mass [kg], $\Delta T = T_M - RT$ – temperature gradient between melting temperature and room temperature, H_f - heat of fusion [kJ/kg].

During processing, the surface layer of the substrate undergoes repeated and localized melting and freezing events. The evidence shows that after a few seconds (i.e., 20s) of plasma treatment, the surface state/morphology reaches a "quasi equilibrium", with a temperature just below T_M. Thus, at this state, only the second term of eq. 5.8 is significant.

Table 5.2 Physical properties of substrate materials.

Physical Properties	Fe (steel)	Ti	Al
Crystal structure	BCC	HCP	FCC
Average Surface Energy [J/m^2]	2.45	2.0	1.15
Melting Temperature, T_M [°C]	1538	1668	660
Density, ρ [kg/m^3]	7874	4506	2700
$\Delta T = T_M - RT$ [K]	1511	1641	633
Thermal conductivity, K [W/m*K]	80.4	21.9	237
Heat capacity, Cp [J/kg*K]	460	540	910
Heat capacity, Cp [J/mol*K]	25.100	25.060	24.200
Heat of fusion, Hf [kJ/mol]	13.81	14.15	10.71
Heat of fusion, Hf [kJ/kg]	272	419	398
Thermal diffusivity α [m^2/s] α = K/(ρ*Cp)	$2.22*10^{-5}$	$0.9*10^{-5}$	$9.64*10^{-5}$
$Cp*\Delta T + H_f$ [kJ/mol]	51.73	55.27	26.03
$Cp*\Delta T + H_f$ [kJ/kg]	967	1305	974
$Cp*\Delta T$ [kJ/kg]	695	886	576
Normalized peaks volume [μm^3/μm^2]	0.104	0.178	0.212
Normalized peaks mass, m [g / m^2]	$819*10^{-3}$	$802*10^{-3}$	$572*10^{-3}$

The produced hills represent most of the molten mass as a result of the plasma processing. A thin "affected layer" (molten and solidified) is also present at the bottom of the

valleys but this was not taken into account in view of the much larger mass of the molten/solidified material in the hills.

$$H_f(Fe) * m(Fe) = 227\ J/m^2$$
$$H_f(Al) * m(Al) = 222\ J/m^2$$

$$Hf(Ti) * m(Ti) = 336\ J/m^2$$

where m = molten mass per unit area, Q = input plasma energy per unit area (constant for all three materials).

The correlation of molten mass and H_f for Fe and Al shows excellent agreement in spite of their diverse thermal properties. It should be noted that during the quasi equilibrium state at the surface, the top layer is maintained at a high temperature, just below the melting point. Thus, it is very reasonable that such relationship between H_f and molten mass exists. However, the above analysis for Ti implies a much smaller molten mass than the one estimated from profilometry. Figures 5.1 to 5.3 show the evolution of surface topography of the three substrates as a function of processing time. It is clear that for Fe and Al substrates, the profilometry measurements are representative of the surface profile. Indeed, hills are well separated by valleys and their volume is accurately estimated by the profilometry analysis. On the contrary, the volume estimation for Ti is less straightforward. Initially, wide-open cavities can be observed, Figure 5.3. In time, some of the cavities are covered by fresh, splashed molten layer-like material. At the full processing time, the surface is almost free of cavities, which are completely covered by freshly solidified material. It is evident that the hidden cavities are not accounted for during the profilometry measurements, resulting in an artificially larger molten volume. A thermal energy input per unit area from the plasma (220 – 230 J/m^2) equal to that for steel and Al, produces a molten mass that is about 33% lower than that obtained from profilometry measurements (with hidden cavities). A closer examination of the SEM evidence, Figure 5.3, suggests that overestimation of the molten volume by 33% is not unreasonable in view of the produced surface morphology.

5.6 Investigation of the Structure, Grain Size and Residual Stresses

The phase structure, grain size and internal stresses of EPP “cleaned” steel, Al and Ti were studied by XRD using a Siemens D-500 x-ray diffractometer with a CuK_{α} radiation source. SEM and HRTEM examinations on cross-section samples fabricated using the FIB lift-off techniques were conducted to observe the produced microstructure at the near surface layer.

Steel

Figure 5.16 shows cross-section SEM micrographs of the EPP cleaned steel. The presence of an affected zone at the surface is evident. A closer examination shows that the affected zone is composed of two layers. SEM cross-section analysis shows that the top affected zone (Layer 1) is less than 2 microns thick. The second layer (Layer 2) that most likely represents a thermally influenced zone in which the steel remains in solid state during the processing, is also clearly defined from the underlying bulk. The analysis is focused mostly on Layer 1 which is in direct relationship with the surface morphology and substrate structure.

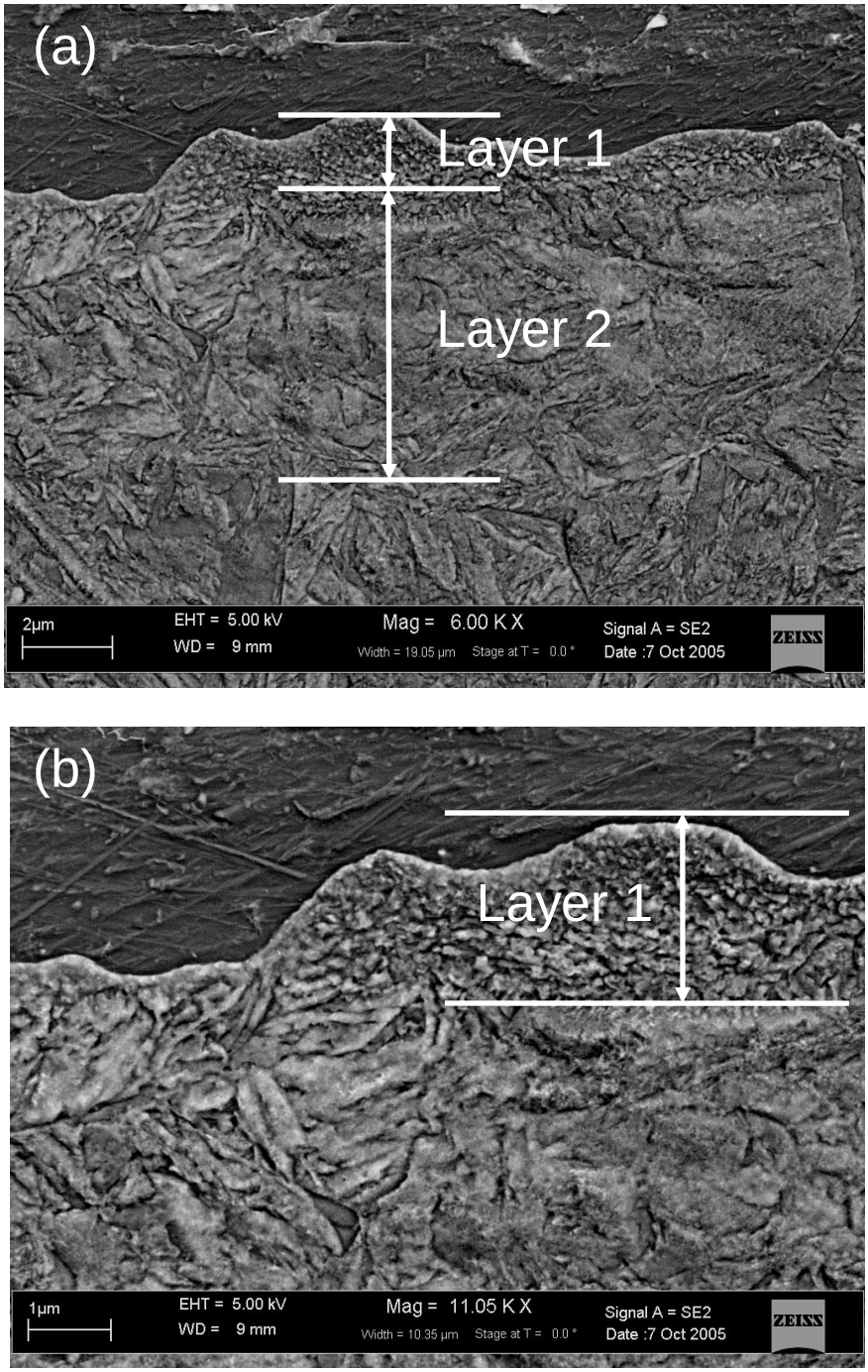

Figure 5.16 Cross sectional SEM images of EPP-treated low-carbon steel, (a) lower magnification with both affected layers, (b) top affected layer detail.

In order to identify the structure changes in the surface layer produced by EPP treatment, XRD measurements were conducted in the 2θ range of 20-120º with a θ-2θ scan. XRD patterns

showed that after the EPP treatment, the crystal structure in the surface layer is mainly composed of BCC α-Fe together with a small amount of martensite, cementite and retained austenite. As the penetration depth of x-rays with Cu K_α radiation in steel at a glancing angle of 22.5° is only 2 μm [8], the XRD pattern for the EPP treated steel mostly originates from surface layer.

In order to study the phase structure at different depths, the glancing angle XRD technique was utilized. In this case, the penetration depth of x-rays diminishes with decreasing the angle of incidence. During the measurements, the incidence angle was fixed while the 2θ angle changed from 42° to 47°. It is interesting to see that the (110) diffraction peak becomes broader and shifts to a lower diffraction angle with reducing the glancing angle. Figure 5.17(a) presents the peak center position and full width at half maximum (FWHM) of the (110) peak as a function of the glancing angle. With reducing the glancing angle, the (110) peak center position decreases linearly while its FWHM increases linearly with reducing glancing angle down to 1° followed by a rapid increase. The grain size, *d*, at different glancing angle was computed using the Scherer equation [100]:

$$d = \frac{0.9\lambda}{B\cos\theta} \tag{5.9}$$

where *B* is the FWHM of the diffraction peak, and θ is half of the diffraction angle. Meanwhile, the penetration depth (D_θ) of x-rays at different glancing angle (α) can be calculated by the expression:

$$D_\theta = 2\sin(\alpha)/\sin(22.5). \tag{5.10}$$

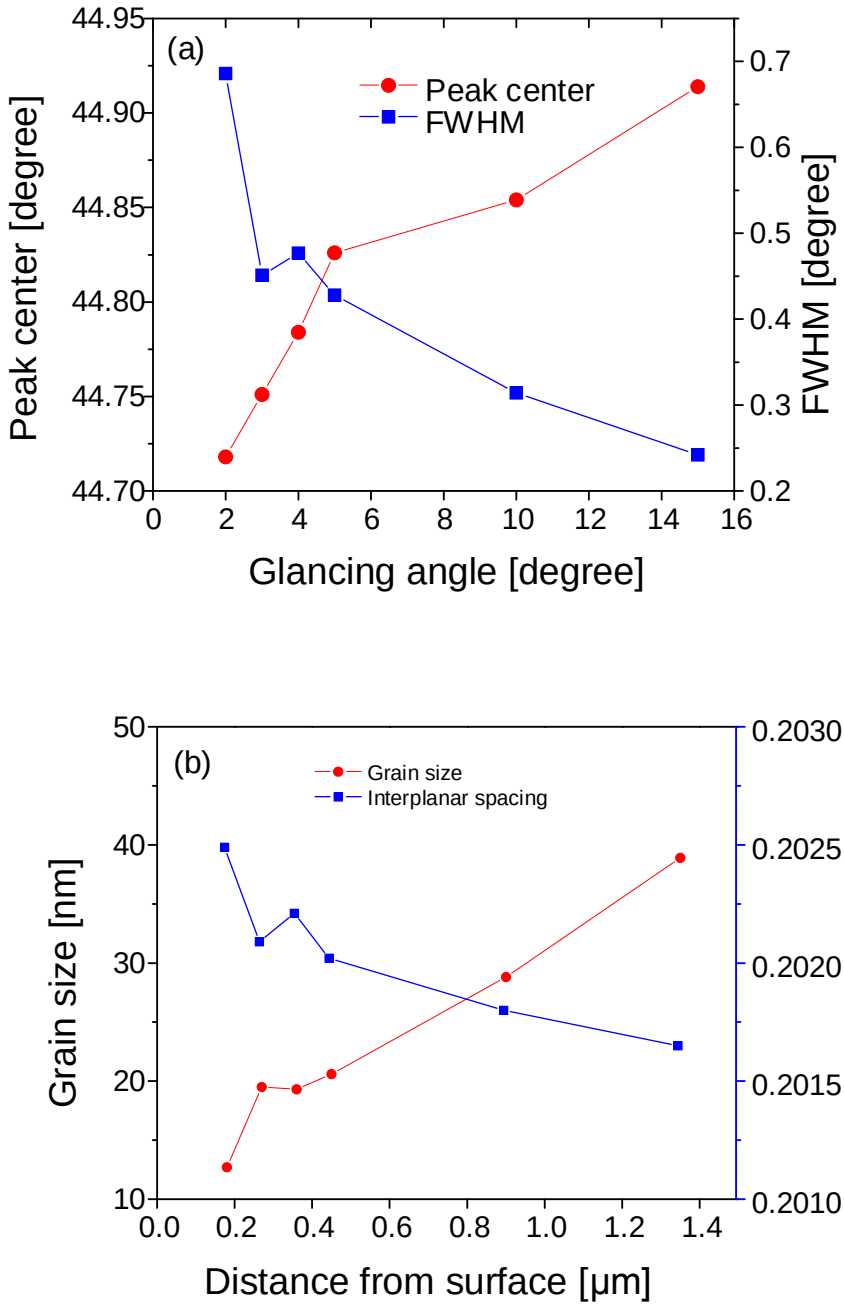

Figure 5.17 (a) Dependence of the peak center and FWHM of the XRD peak on the x-ray glancing angle and (b) calculated depth profile of interplanar spacing and grain size for EPP processed steel.

The grain size at different depth is plotted in Figure 5.17(b). Two distinct regions are shown: a top layer and subsurface layer. In the top layer (about 300 nm thick), the grain size is fairly small, but it increases rapidly with increasing depth. In the subsurface region, the grain size increases

slowly, but monotonically with increasing depth. This is consistent with the SEM observations. It should be noted that the grain size calculated from the FWHM of the XRD peaks measured at higher glancing angles should be larger than the value shown in Figure 5.17 because both the surface region and sub-surface region contribute to the XRD pattern. The cross sectional TEM was necessary to obtain detailed information on the change of grain size as a function of depth. As discussed above, the ultra-small grain size in the surface region results from the rapid freezing of the local melting produced by the process. Furthermore, the gradual change of the grain size is attributed to the pertaining temperature gradient.

Interplanar spacing was obtained from the positions of the diffraction peaks using Bragg's law. The interplanar distance and grain size at different distance from the surface were calculated and plotted in Figure 5.17(b). It can be seen that the interplanar distance decreases linearly with increasing distance from surface. Zhang et al [88] proposed that the stress, σ, in films can be obtained using glancing angle x-ray diffraction by

$$\sigma = -\frac{E}{\nu}\Delta l\,, \tag{5.11}$$

where $\Delta l = (l - l_0)/l_0$; E and ν are the Young's modulus and Poisson's ratio, respectively; l_0 is the distance of the unstressed *hkl* plane, *l* represents the distance of the stressed *hkl* plane in the direction normal to the sample surface, which is defined as:

$$l = \frac{d_{hkl}}{\cos(\theta - \alpha)}\,, \tag{5.12}$$

where d_{hkl} is the d-spacing of the diffracted *hkl* plane and α is the x-ray incidence angle. From this equation, it can be seen that the larger interplanar spacing in the near surface region indicates the presence of a higher compressive stress, and the decrease of interplanar spacing implies a reduction of compressive stresses with depth. However, it is difficult to calculate the internal stress at different depth since it is hard to determine the value of l_0.

In order to investigate the existence of a compressive stress and obtain qualitative information about the internal stress in the EPP-treated surface layer, the standard $d_{hkl}(\psi)$ versus

sin²(ψ) method was used. The (310) ferrite reflection was used for the stress measurements due to its high diffraction angle (about 116.4°) and relatively high intensity. During measurement, the specimen surface was tilted 0-30° (ψ angle) and a θ-2θ scan was conducted in the 2θ range of 110-120°. The calculated $(d_\psi - d_0)/d_0$ *vs* $sin^2(\psi)$ is plotted in Figure 5.18.

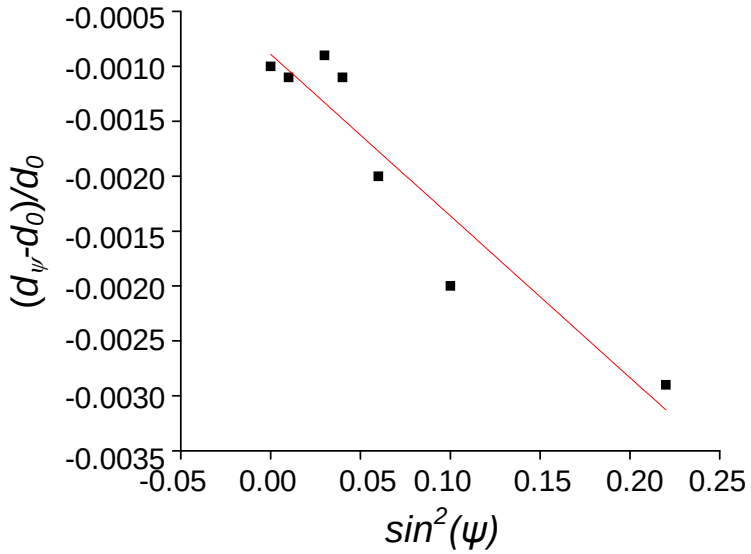

Figure 5.18 $(d_\psi - d_0)/d_0$ *vs* $sin^2(\psi)$ plot for the (310) ferrite reflection.

As shown, the $(d_\psi - d_0)/d_0$ decreases linearly with increasing $sin^2(\psi)$, indicating a compressive stress. For cubic structures, the stress (σ) in a thin layer in a state of equi-biaxial stress could be computed according to the $sin^2(\psi)$ method by the following equation [101]:

$$\frac{d_{hkl}(\psi) - d_0}{d_0} = \sigma\left[\frac{1+\nu}{E}\sin^2(\psi) - \frac{2\nu}{E}\right], \qquad (5.13)$$

where d_0 is the stress-free lattice parameter, $d_{hkl}(\psi)$ is the lattice spacing measured with the surface tilted at ψ angle, ν and E are the Poisson's ratio and elastic modulus, which are 0.29 and 200 GPa, respectively for 4340 steel [101]. The internal stress in the surface layer can be calculated from this equation after obtaining the slope of the $(d_\psi - d_0)/d_0$ vs. $sin^2(\psi)$ plot. The internal stress is calculated to be -1.8 GPa. The negative sign indicates that the stress in the surface layer is compressive. Such high compressive stress at the surface layer is expected to be

beneficial to resist crack initiation that may be produced by fatigue or stress environment interaction phenomena (hydrogen embrittlement and stress corrosion cracking).

The compressive stress maybe a consequence of the collapsing of hydrogen bubbles formed during EPP treatment, which produces a low-frequency shock wave on the steel surface. The shock wave could generate a compressive stress in the surface layer. It is expected that the amplitude of the shock wave diminishes with increasing distance from steel surface, corresponding to a decrease in internal stresses. In addition, during EPP treatment, the voltage is applied to a thin near-electrode plasma region generating a high electric field between 10^6 and 10^8 V/m [102]. The high electric field in the plasma accelerates the anions providing kinetic energy. The bombardment of the surface layer by the energetic ions could also contribute to the observed internal compressive stresses. This phenomenon has been widely observed in thin film physical vapor deposition involving ion bombardment [25].

Aluminum

A similar analysis was conducted on EPP treated Al. TEM cross-sectional samples were fabricated using the FIB lift-off technique and XRD peak analysis was used for grain size and residual stress studies.

Figures 5.19(a) and 5.19(b) are cross-sectional TEM micrographs that represent typical appearance of the top Al surface layer after EPP treatment. The presence of a near-surface layer with fine microstructure and about 2μm in thickness is evident. Furthermore, a couple of hills with even finer microstructure are clearly displayed. Figure 5.20(b) is a higher magnification micrograph showing details of the microstructure of the surface layer. This affected layer exhibits a microstructure composed of a very fine structure near surface layer followed by a zone with a grain size of approx. 500nm. The bulk grain size shown below is about ~5μm, Figure 5.20. The electron diffraction pattern (inset in Figure 5.20(a)) taken from one of those large grains confirms a single grain structure. The unusual size of this particular top surface grain is the result of the recrystallization resulting from the sequential melting-solidification which is much higher for low melting temperature metals.

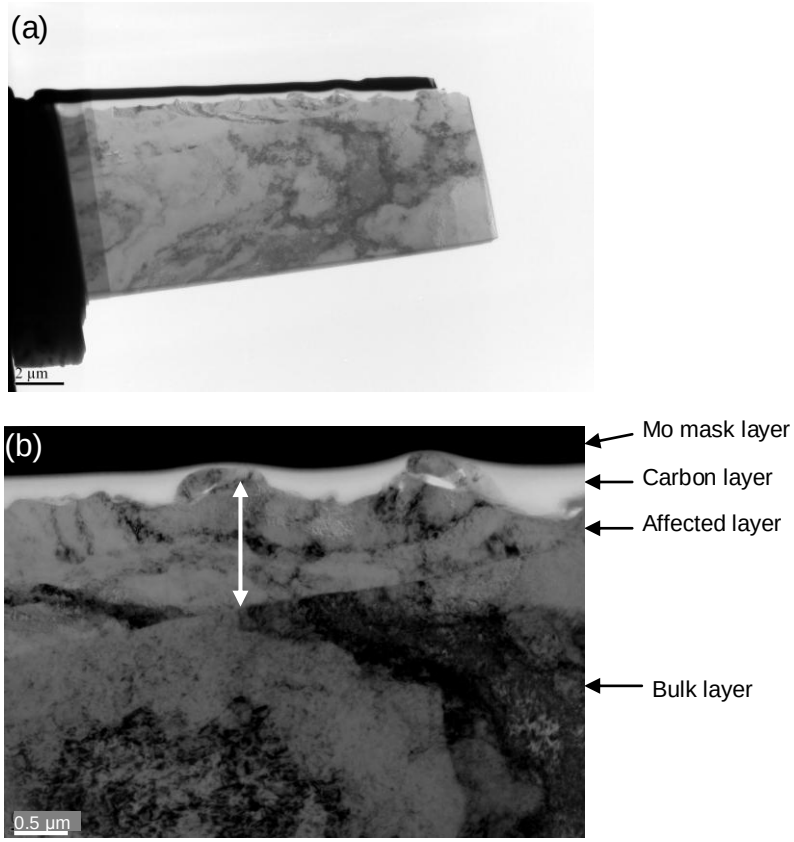

Figure 5.19 Cross-sectional TEM images of EPP treated 1100 Al showing (a) lower magnification of the affected layer and bulk, and (b) interface between surface affected layer and bulk. The affected layer thickness is about 2µm.

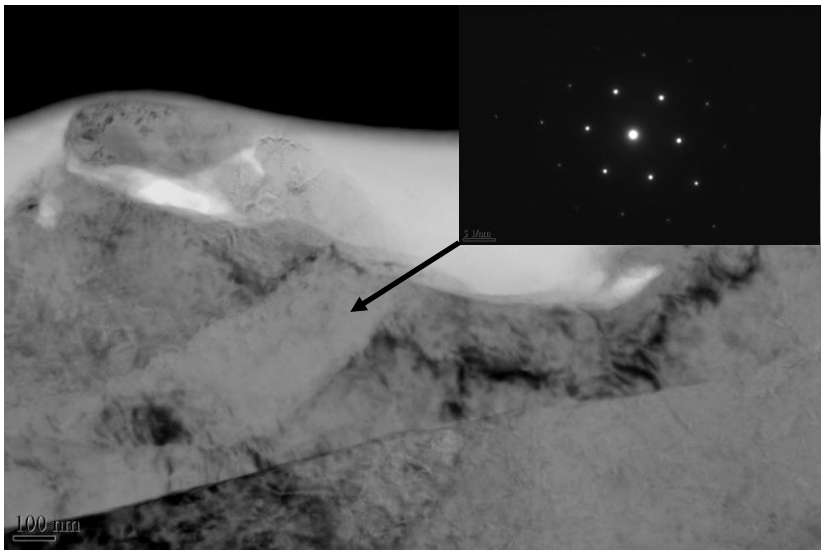

Figure 5.20 High magnification of the affected layer showing a fine microstructure followed by a larger grain size microstructure. The electron diffraction pattern (inset) was taken from one of those grains from the underlying structure.

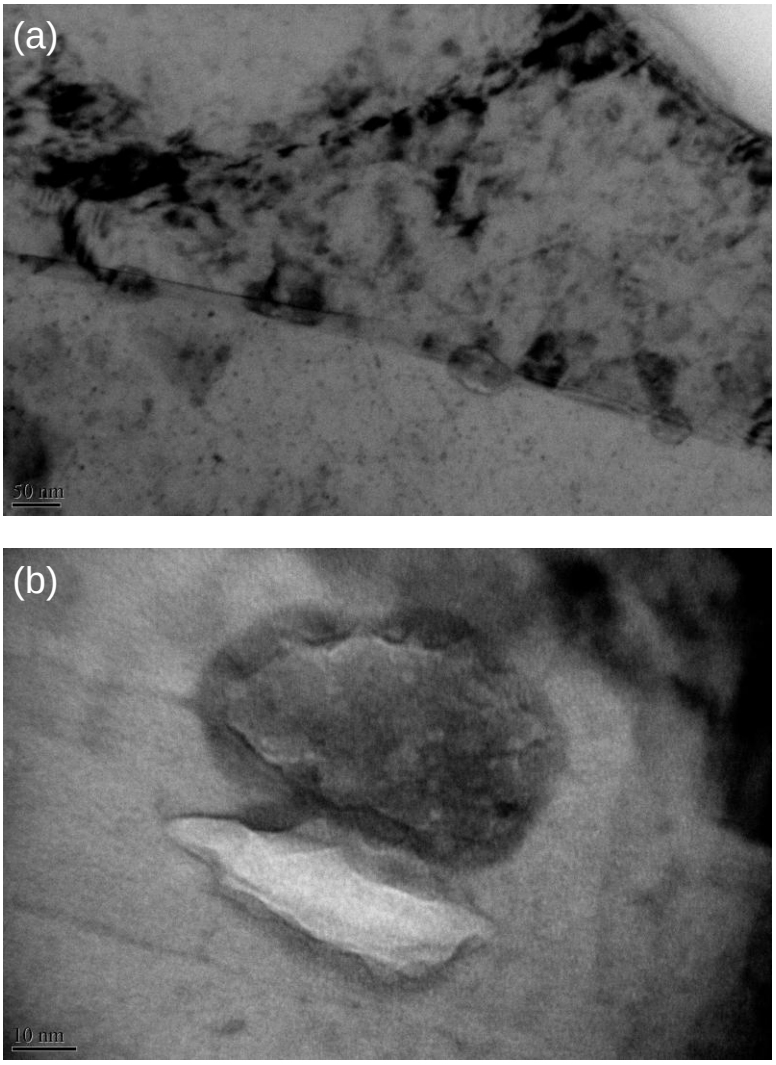

Figure 5.21 (a) Interface between affected top layer and bulk containing intermetallics for EPP processed Al, (b) high magnification of an intermetallic at the interface.

An interesting observation was also made at the interface of the affected layer with the bulk. Melting of the affected layer allowed several intermetallics to segregate at the interface, Figure 5.21. Such intermetallics (of average size 20 - 30 nm) are typically present in Al and Al alloys. The localized segregation of impurities indicates a mapping of the temperature gradient in the surface layer. Anything below this intermetallics level is expected to remain solid material during processing. All future thermodynamics considerations can be based on the solidified layer with boundaries given by the localized intermetallics.

A very thin layer was also observed at the very top of the surface, Figure 5.19. This layer exhibited a very fine microstructure and smaller grain size compared to the underlying layer. It should be noted that the latter layer has a much larger grain size due to continuous annealing that takes place. The top layer on the other hand is the result of the last solidification event during processing that was not subsequently annealed to increase its grain size. This layer is around 10 times smaller than the main affected layer and contains a grain size of about 35 nm.

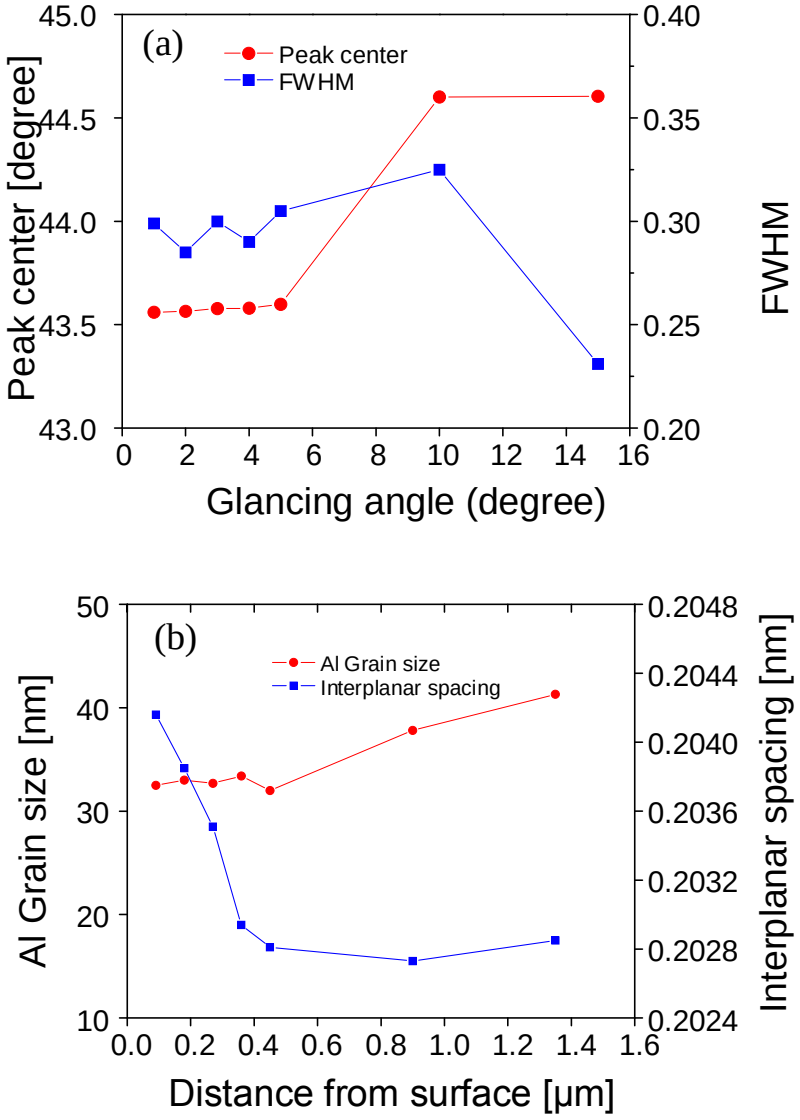

Figure 5.22 (a) Dependence of the (110) peak center and FWHM on the x-ray glancing angle and (b) calculated depth profile of interplanar spacing and grain size of EPP-treated Al.

An intermediate step in the grain size calculation from X-ray measurements is the determination of peak center location and FWHM for the diffraction angle considered. A peak center shift with glancing angle gives an initial indication of a grain size variation, Figure 5.22(a).

The calculated grain size, Figure 5.22(b), is ~32 nm. It should be noted that as the incident angle of the X-ray increases, the average grain size is estimated for an increasing excitation volume. In view of that, the XRD and TEM observations are in close agreement. All grains below the surface layer will inherently undergo annealing, and thus, expected to increase in size with depth from the surface therefore, resulting in an increase in the grain size average, as calculated from XRD.

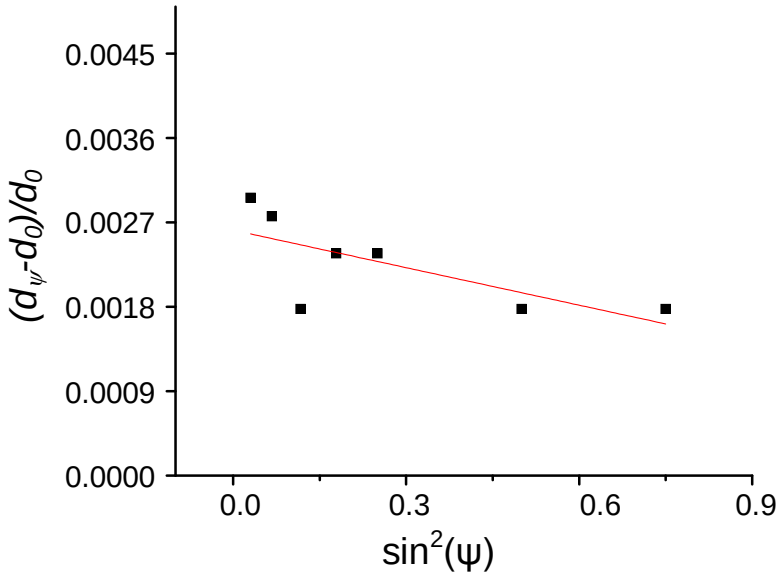

Figure 5.23 $(d_\psi - d_0)/d_0$ *vs* $\sin^2(\psi)$ plot for the (311) x-ray peak of EPP-treated Al.

Residual stress calculations were conducted using a higher diffraction peak (311), Figure 5.23, around $2\theta = 98^o$. The same procedure was followed as for steel. A Poisson ratio and elastic modulus of 0.35 and 70 GPa, respectively, were used in the calculations. The residual stresses were estimated to be compressive in nature and about -66 MPa. Interplanar spacing, Figure 5.22(b), gives an indication on how the residual stresses are distributed. A sharp variation at the near surface within the first 300 nm distance from the surface can be observed, Figure 5.22(b).

This is an indication that residual stresses are located only in the upper solidified layer that was not exposed to the annealing process from the repeated heating cycles. At around 400nm below the surface residual stresses are near zero.

Titanium

Microstructure, grains size and residual stress analysis was also performed for EPP "cleaned" pure Ti.

Figure 5.24 shows a typical microstructure of the produced layer after EPP processing. A surface affected layer can be clearly distinguished from the bulk, Figure 5.24(a). The affected layer thickness is about 1.5μm. The bulk shows no microstructural change, Figure 5.24, with a grain size around 5 μm, Figures 5.25(c) and 5.25(d). The affected layer presents a textured microstructure, with elongated grains normal to the surface, characteristic to a fast solidification process and heat extraction direction. There are several layers of elongated grains, oriented normal to the surface, suggesting they were formed sequentially in more than one freezing cycle.

A closer look at the affected layer, Figure 5.26(a), shows that these elongated grains are around 500 nm. A more detailed observation of the top layer, Figure 5.26(b), reveals the presence of another crystalline layer of 100 nm thickness near the surface. Direct measurements give a value of approximately 40 nm for the grain size of the top layer. As suggested earlier, this top layer was formed in the last melting/solidification cycle and was not exposed to additional thermal cycle from processing. The difference in grain size between the top layer and sub-surface layers (annealing effect) is more evident in the case of Al, compared to Ti. This effect is consistent with the lower T_M and thus annealing temperature of Al compared to Ti.

The (101) peak with the strongest intensity was found around $2\theta = 40^o$ and was chosen for the grain size analysis following the same glancing angle procedure as described earlier. The peak shift is plotted in Figure 5.27(a) along with the FWHM variation. The change in grain size is calculated and plotted in Figure 5.27(b) along side with the interplanar spacing. It can be seen from Figure 5.27(b) that the grain size has the lowest value for a very narrow range of the layer thickness at the near surface corresponding to the last solidification event. This layer has not

undergone any recovery and its grain size is representative of the prevailing solidification conditions of the molten top layer. The calculated grain size from XRD is 20-30 nm and in good agreement with the TEM observations.

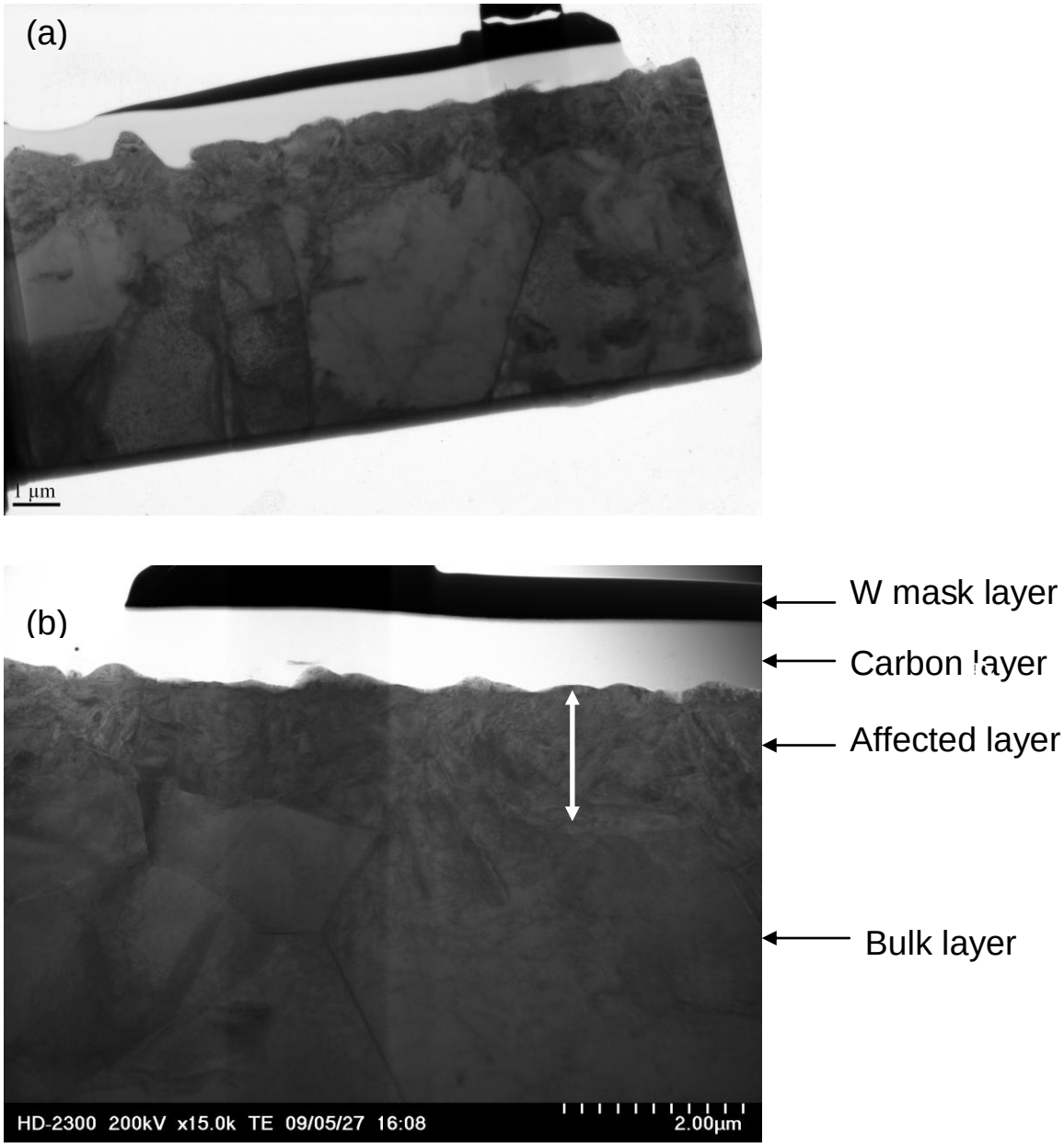

Figure 5.24 Cross-sectional TEM micrographs showing (a) overall view of the affected layer and bulk and (b) higher magnification showing thickness of the top EPP-treated layer.

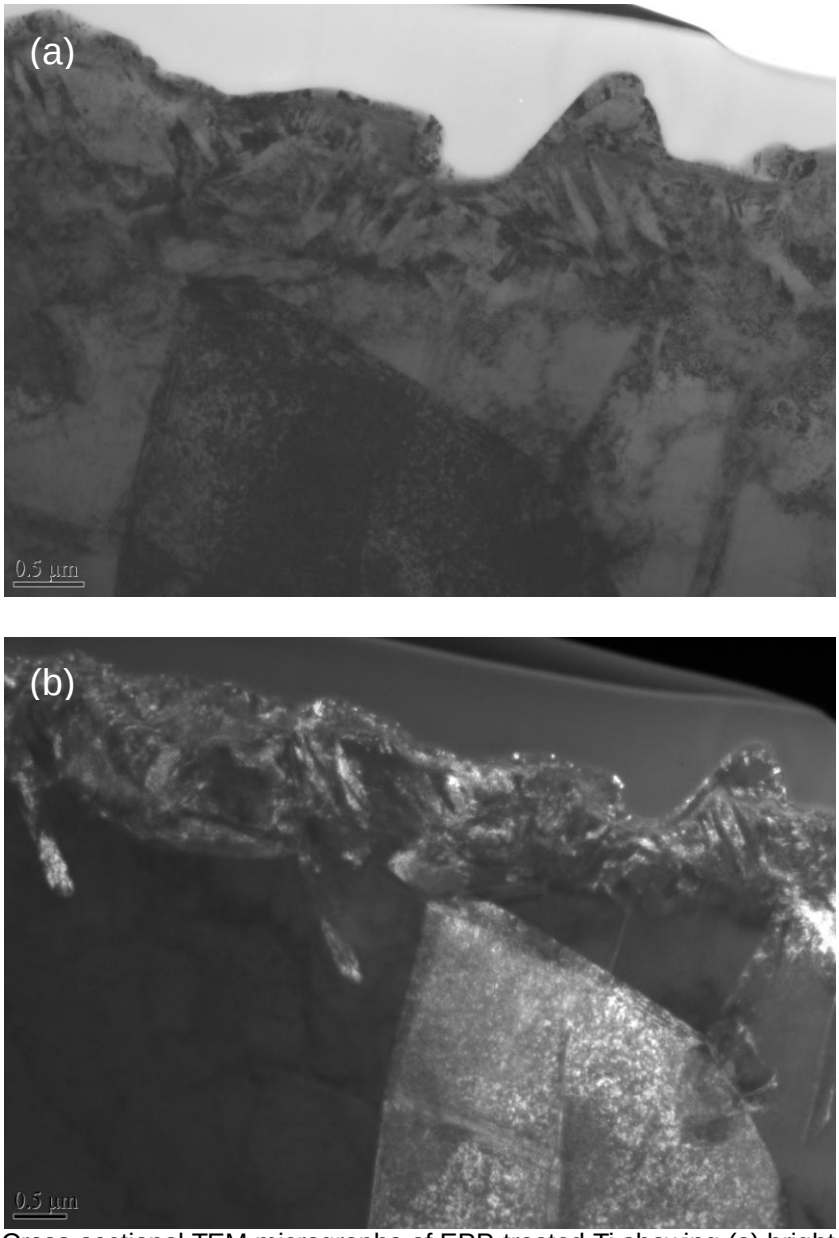

Figure 5.25 Cross-sectional TEM micrographs of EPP-treated Ti showing (a) bright field and (b) dark field image of top surface layer.

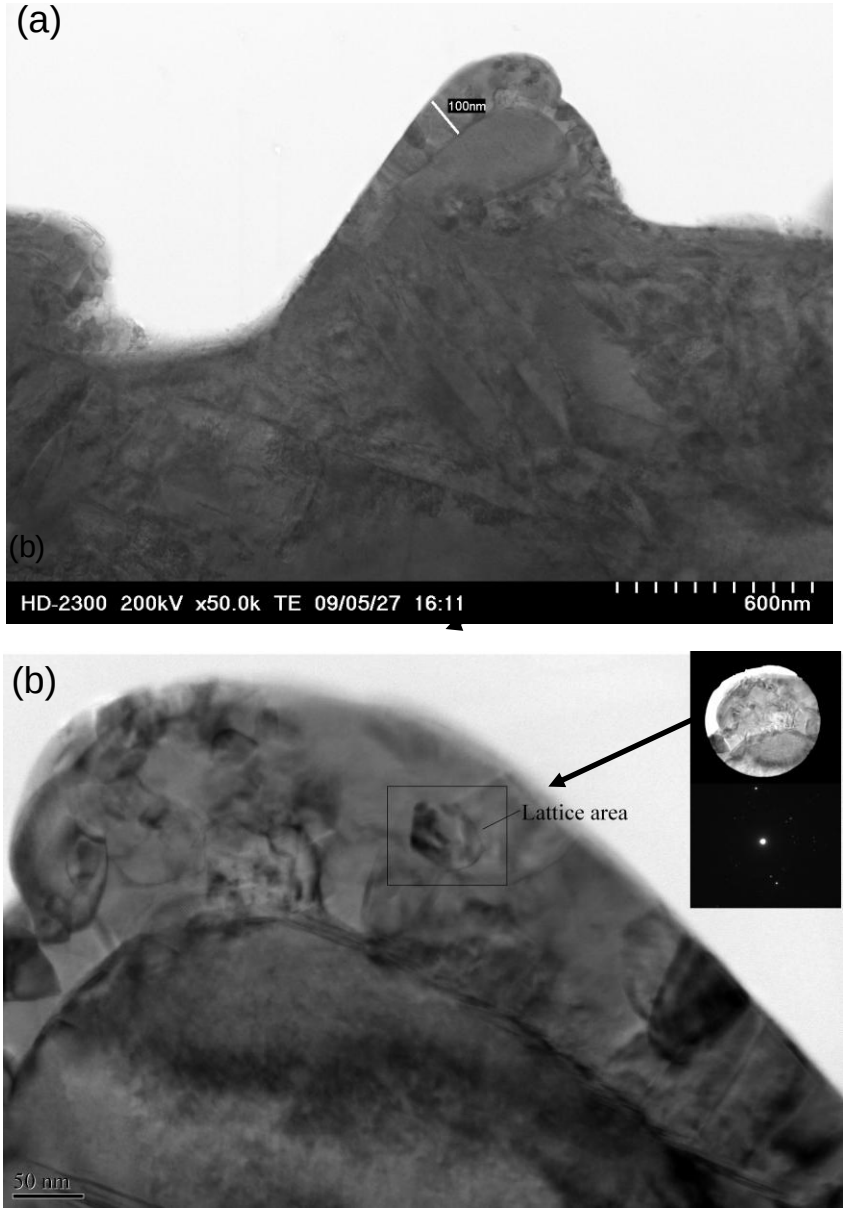

Figure 5.26 Cross-sectional TEM images of EPP treated Ti, a) appearance of affected layer and b) high magnification of the top layer (inset diffraction pattern).

T_M for Ti is significantly higher than that of Al, indicating the effect of annealing is limited and the compressive stress will be present through the affected layer. From Figure 5.27(a), the variation of the peak center towards lower angle with decreasing glancing angle (incident X-ray penetration moving closer to the surface) and FWHM of the diffraction peak shows a broadening

effect. The variation of the interplanar spacing is shown in Figure 5.27(b), with the distance from the surface which suggests a compressive stress uniformly distributed along the layer depth.

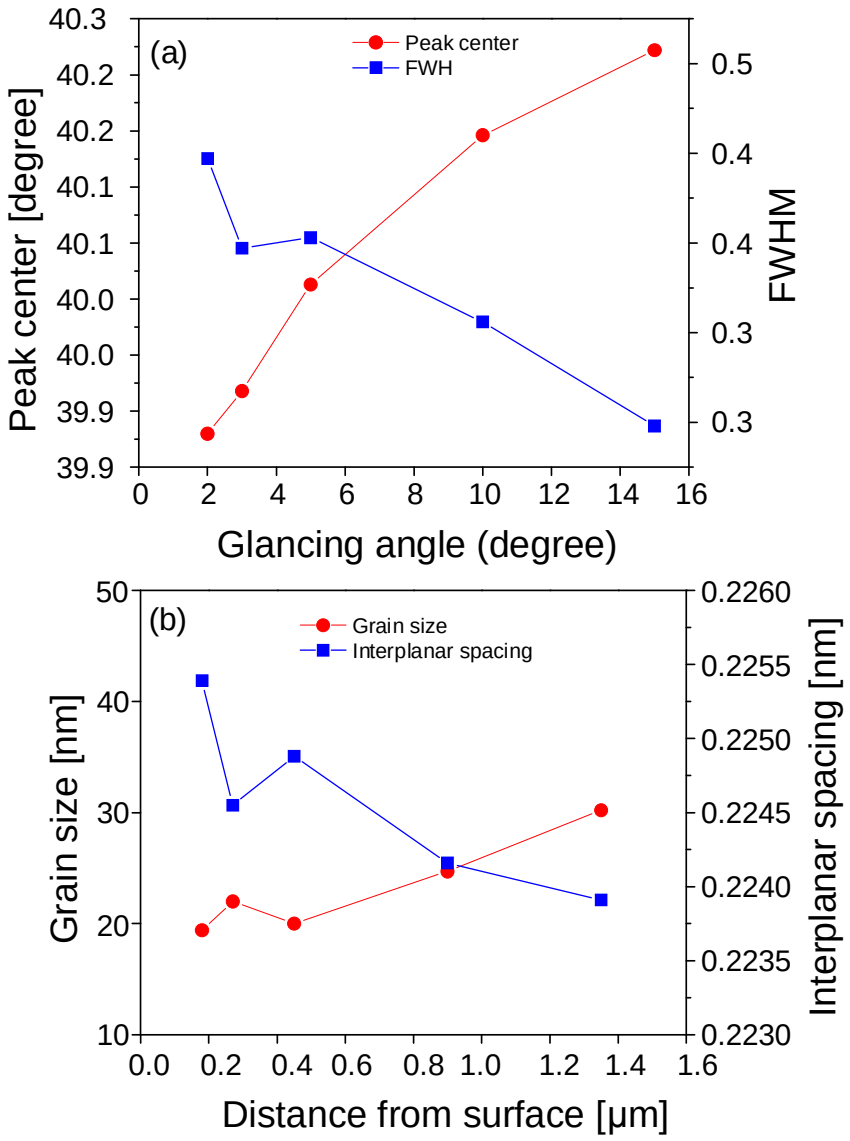

Figure 5.27 (a) Dependence of the peak center and FWHM of the XRD peak on the x-ray glancing angle, and (b) calculated depth profile of interplanar spacing and grain size for pure Ti.

Residual stresses were measured using the standard $d_{hkl}(\psi)$ versus $sin^2(\psi)$ method and the (103) high diffraction peak around 2θ = 70.5º, Figure 5.28. A Poisson ratio and elastic modulus, of 0.32 and 116 GPa, respectively, were used in the calculations.

Figure 5.28 shows that the $(d_\psi - d_0)/d_0$ decreases linearly with increasing $sin^2(\psi)$, indicating a compressive stress in the treated surface. The residual stress was estimated to be around -1.88 GPa. The high value of the compressive stress indicates that the EPP-treated surface layer is expected to have improved mechanical properties such as fatigue resistance.

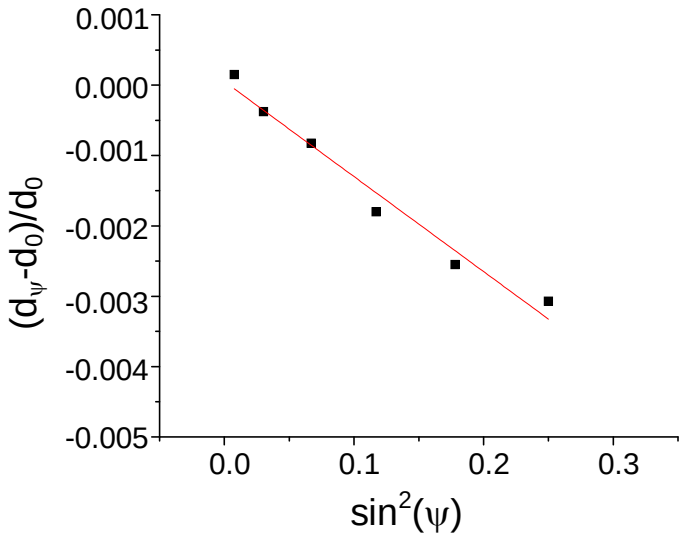

Figure 5.28. $(d_\psi - d_0)/d_0$ *vs* $sin^2(\psi)$ plot for the (103) x-ray peak of Ti.

5.7 Concluding Remarks

EPP is a surface treatment that induces localized melting and quenching cycles at the near surface region. These repeated cycles result in significant changes of the surface in morphology and near surface microstructure.

The three substrates investigated in the present work (Steel, Al and Ti) cover a wide range of T_M, nevertheless the affected layer thickness is remarkably comparable in thickness for all three substrates, at around 1.5 - 2μm, Table 5.3. A distinct interface has been observed between the affected layer and the bulk material. It is suggested this is the result of the applied energy per unit area that was maintained constant for all three processed materials. The fast cooling rates induced by the electrolyte in direct contact with the processed substrate will reach an equilibrium balance of the heat loss with the heat diffusion through the material. The experimental evidence shows that it is only the first 1.5 - 2μm from the surface that goes through

the melting-cooling cycle. This is the result of the short lifespan of plasma and the hydrogen bubble before collapse (less than 1 – 5 ms) [16] that will not allow heat to diffuse through the bulk.

In other words, the similar thickness in the molten layer for all three diverse substrates suggests that the extent of the melting for the present energy input is controlled by cooling via the electrolyte.

An evaluation of thermal conductivities for Steel, Al and Ti (absolute values 80, 237, 22 respectively) shows that although Al has the highest thermal conductivity value, and would be expected to form a thicker affected layer compared to steel and Ti, this is not the case. The small difference in layer thickness (~25%) among these three materials suggests thermal conductivity may be a factor, but with a small influence in the overall process.

Table 5.3 Thickness and grain size of the affected layers for EPP processed steel, Al and Ti.

Characteristics	Steel	Al	Ti
Thickness of surface layer [nm]	100	200	100
Grain size of surface layer [nm]	15 – 20	35	20
Thickness of affected layer [μm]	1.5	2.0	1.5
Grain size of affected layer [μm]	0.5	1.0	0.4 – 0.5
Residual Stress [GPa]	-1.8	-0.066	-1.88

The rapid change in substrate structure induced high compressive stresses for both high T_M materials, calculated at -1.8GPa for Steel and -1.88 GPa for Ti. The compressive stress for Al is about 50 times lower, and is due to effective annealing along the affected layer. The sharp variation in interplanar spacing, Figure 23(b), which flattens out beyond 400 nm depth from the surface, can be explained by the fact that only the last solidified top layer (not annealed) will experience significant residual stresses. The smaller grain size in this top layer relative to the main affected layer is also supporting this argument.

The well defined boundary between affected layer and the bulk is a characteristic of the EPP process. X-ray analysis of the grain size shows nanocristalline grains in the top surface layer in the range of 15 – 20nm for Steel, 35 nm for Al and 20 nm for Ti. The bulk crystal size is in the microns range, Figure 5.16 (b), 5.19 (b) and 5.24 (b). The three materials having different crystal structures (bcc, fcc, hcp) will yield the same result: a nanocrystalline structure.

The EPP treatment was found to produce a two layered surface microstructure. The very top surface layer possessed the finest grain size ranging from 15 to 40 nm. The underlying layer had a larger grain size due to annealing by the plasma action. This is producing a rather gradient microstructure from the bulk.

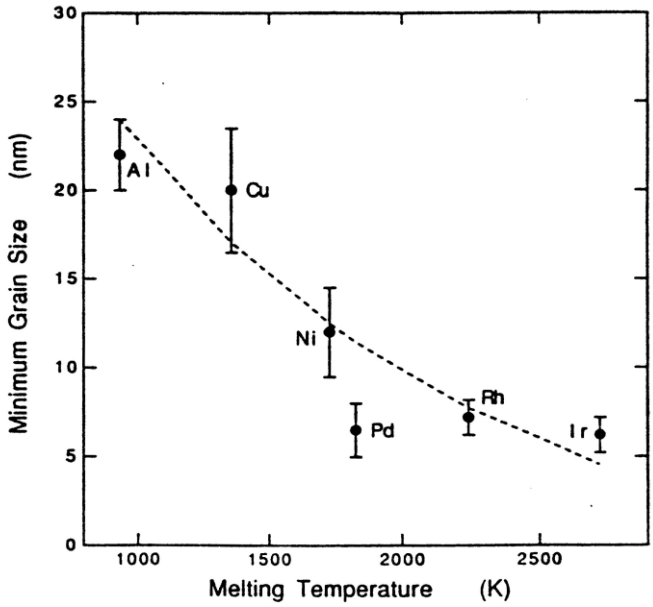

Figure 5.29 Minimum Grain Size versus T_M for metals [103].

The quenching of the molten metal caused by the electrolyte creates the observed nanostructure in the affected surface layer. The observed grain size is a direct result of the T_M of the treated metal. Similar effects have been observed in nanocrystalline Cu, Ni, i.e. prepared by mechanical attrition [103]. The previous work has found the same correlation between grain size and T_M, Figure 5.29. Nanosize grains produced by mechanical attrition (milling) scale with T_M and the result represent a balance between the heavy mechanical deformation induced during milling and the recovery behavior. EPP creates a submicron size grain structure following the same interdependence and the resulting grain size is in good agreement with the mechanical attrition processes (Al with the larger grain size corresponding to a lower T_M). Moreover, the EPP process suggests that the crystal structure is not a major factor in EPP, since there is no plastic deformation, but melting followed by solidification cycles. The EPP process extends the

applicability of the T_M to bcc and hcp metals. TEM and SEM observations of the microstructure with the optical profilometry analysis create a complete picture of the process mechanics.

As previously mentioned, EPP involves plasma interaction with a metallic substrate followed by cycles of fast melting and solidification processes. The solidification during EPP is not well understood, therefore several assumptions were made in an effort to reconcile the plasma processed substrate morphology and microstructure to classic solidification theory and parameters.

Solidification in metals and alloys produces solid phases with the release of latent heat, or heat of fusion, H_f .Undercooling is another key factor that affects the solidification of metallic materials. During the initial solidification process, undercooling is needed to drive the heterogeneous or homogeneous nucleation [104, 105] and an undercooled metastable state may appear as a liquid. The undercooling also affects the subsequent solidification and heat transfer. This suggests that during the solidification process, two types of heat transfer mechanisms may be present, from the initially undercooling as well as heat extraction through the electrolyte. Studies showed that undercooling on solidification has effects on the structure refinement, segregation and distribution of impurities [106]. Interface formation and evolution for both substrate surface modification and coating deposition microstructure may be originated from this undercooling.

A recent study on undercooling effects on droplet solidification for molten pure aluminum has shown a correlation between droplet size, undercooling and cooling rate [107]. Pure Al powder was used as study material and cooling rates on 5, 10 and 20 K/min were observed. The following equations were used in the study to describe the above effects:

$$X = \exp[-M\pi D^2] \tag{5.14}$$

where X - nucleation-free fraction of the droplet, M - number of nucleants per area and D - diameter of a spherical droplet.

$$\ln(\Delta T) - B\frac{1}{\Delta T^2} = \ln R - \ln(a\Omega_a) \tag{5.15}$$

where ΔT - undercooling, a - catalytic surface area, Ω_a - logarithmic factor, R - cooling rate and B - complex factor that is a function of heat of fusion and melting temperature.

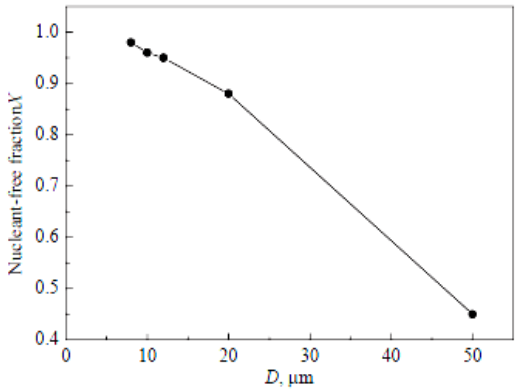

Figure 5.30 Relation of the free nucleation fraction versus the droplet size [107].

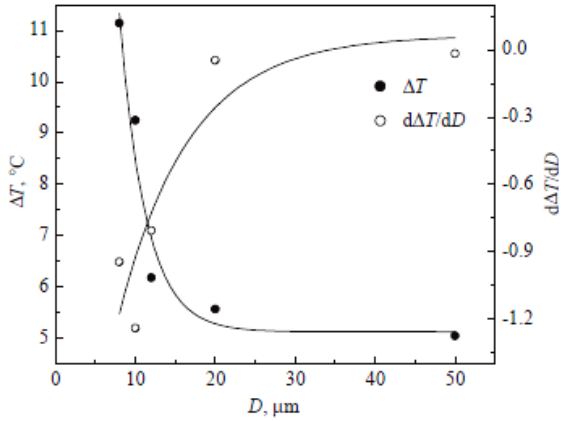

Figure 5.31 Relation between the undercooling and the size of droplet [107].

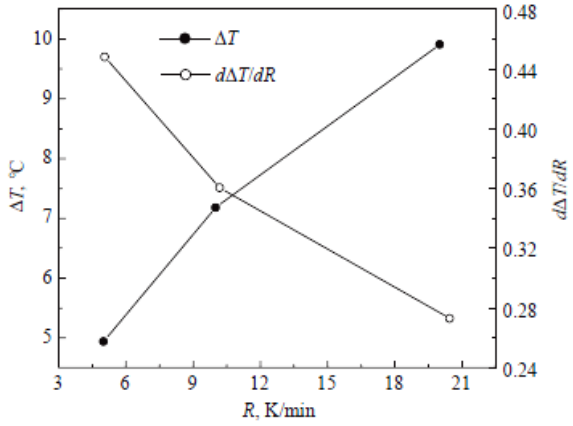

Figure 5.32 Relation between the undercooling and the cooling rate for droplets [107].

Figure 5.30 shows that the fraction of the droplet contributing to nucleation will increase with decreasing droplet size. Assuming that the droplet size for EPP represents the average hill (nodule) size of the processed surfaces (`1 – 2 μm), it is safe to assume a close to 100% nucleation-free fraction for all three substrates during EPP. Figure 5.31 shows that the undercooling as well as the change rate of undercooling (with respect to the cooling rate) increases with the decreasing droplet size, with an abrupt increase below 20 μm. Figure 5.32 shows the relation between the undercooling and the cooling rates. It is clearly seen that undercooling increases with the increase of cooling rate. EPP, for which much higher cooling rate are expected compared with the above experimental data, a maximum but limited undercooling will be present for the extremely high cooling rates.

From the above experimental case scenario can be concluded that for small droplet size and high cooling rates, undercooling plays a significant role in the nucleation and solidification of EPP treated surfaces.

Considering the high rate of heat transfer characteristic of EPP, undercooling should be taken into account for different metals and factored in a possible general solidification mechanism for EPP. Solidification models for alloys melt with undercooling are already available [105] and they can be adapted to take into consideration the bubble-surface interaction, substrate molten droplets re-solidification and surface energy at the solid-liquid phase.

In summary, the EPP - treated substrates have been found to exhibit several common characteristics:

1. EPP-treated materials possessed a unique surface morphology composed of hills and valleys. However, each material was found to exhibit its own individual characteristics. Those were suggested to be influenced by several factors, such as surface energy, melting temperature, heat of fusion and undercooling.

2. The affected layer extends to a depth of about ~ 2 μm from the surface. This was attributed to the dominating cooling by the electrolyte of the applied energy level during processing (the estimated energy per surface area was ~ 200W/cm^2).
3. The affected layer is composed of a (i) top layer with an ultrafine grain structure (10-40nm) with the grain size depending on T_M followed by an (ii) underlying layer with a coarser grain size (400 nm to 1000 nm). The grain size in this layer depends also on T_M that determines the annealing effect and grain growth kinetics.
4. EPP-treatment produced a desirable compressive residual stresses in all three materials. The magnitude of the residual stresses was also attributed to T_M that determines the cooling rate and extent of annealing.

CHAPTER 6

MICROSTRUCTURAL EVOLUTION OF NEAR-SURFACE LAYERS DURING EPP COATING DEPOSITION

6.1 Physical Characteristics of Coating Surfaces

Over the last several years, a limited number of studies were conducted on metallic coatings deposited with EPP process [27, 40, 42, 69, 70]. Such investigations were initiated on specific applications and the objective was the empirical optimization of the process parameters for deposition of metallic coatings. Having this particular final objective in mind, characteristic tests related to functionality of the coatings were performed: study on the composition, corrosion resistance, wear, and mechanical properties such as bond strength (coating adhesion) and hardness.

Coating deposition during EPP is a combination of three concurrent processes: ion acceleration through the plasma, ion adsorption and transport to the surface via bubble collapsing. The metal ions present in the electrolyte are accelerated toward the substrate surface by riding on the surface of the bubbles and thrown on the metal surface as the bubbles collapse. This typically results in unrealistically high deposition rates (as high as 1 μm/s), as evidenced by previous experimental observations [40]. However, such high rates of deposition may be associated with porosity in the coating. Due to local surface melting, deposition initially is expected to involve some mixing of substrate/coating elements, resulting in a good adhesion for the subsequent coating formation. Due to high plasma energy and very fast cooling rates, an ultrafine grain structure can form along with non-equilibrium phases at the substrate/coating interface [40].

Based on the process description given in Chapter 3, favorable plasma conditions for EPP are developing in a specific V-I envelop, and thus, a characteristic input energy may have a direct influence on process behavior. In view of the energetic considerations, a key material

property influencing/controlling the outcome of the plasma/surface interaction is expected to be attributed to the T_M of the substrate and the coating material. Both are expected to critically influence the extent of possible mixing at the substrate/coating interface as well as the coating microstructure. Thus, a basic understanding of these interactions is needed to design and develop coating systems of interest.

In order to simplify the variables involved, one substrate material was used. In the present case, a low carbon steel was selected that was studied as a substrate in the previous chapter and three different coating materials (Zn, Ni and Mo), exhibiting a variation in T_M and phase diagram characteristics with respect to the substrate, Table 6.1. Steel was selected as the substrate due to its wide utilization at present in relation to EPP. The intent was not to study all possible combinations but rather to address important characteristics allowing future extrapolation. EPP can be a sequential cleaning and coating process. However, at this stage, the main interest was concerned with the interaction zone first forming during coating deposition. Thus, for simplicity, flat polished samples were utilized, rather than samples possessing a “hill” and “valley” profile, treated by EPP. It is noted that this aspect, studied in the previous chapter (“cleaning”), will still be present here since at the initial stages, the surface-cleaning action also occurs during EPP coating.

Table 6.1. T_M of the selected coating elements.

Coating element	T_M [ºC]
Fe (substrate)	1538
Ni	1455
Zn	440
Mo	2623

Results from previous chapters show that T_M of the substrate material plays a role in the resulting surface topography. At this stage, among other parameters, we investigate the effect of the difference in T_M between the substrate and coating material on the nucleation of the coating at the interface with the substrate. The deposition process in the initial stage involves surface melting of the substrate at the same time with arrival and deposition of the coating material. Therefore, certain amount of mixing may be occurring, developing an interaction zone. In view of

the extremely high cooling rate of deposited coatings (as mentioned previously), the extent of mixing, if present, is expected to be influenced by the relative T_M of the substrate and coating material and possibly their solubility or other phase diagram characteristics.

6.1.1 Surface Morphology

Surface characterization of three coatings deposited using EPP provides information especially related to the last stage of EPP deposition. However, it should be noted that a similar surface morphology exists at any time during arrival of the new coating specie. Thus, coating evolution may have been continuously affected by the prevailing surface morphology.

Zn Coating

Coatings of metallic Zn have generally been regarded as the most popular and economical means of protecting steel products from corrosion because Zn acts as a sacrificial anodic coating. As such, including Zn as part of the present study was appropriate not only for its low T_M, fitting well in the study of the T_M influence of surface microstructure, but also as a potential incentive for industry to adopt EPP processes for large scale applications.

Zn coatings were found to be dull grey in color with a matte finish. Figure 6.1 presents a top-view micrograph of the coating. Under SEM, at lower magnification, Figure 6.1(a), the Zn coating exhibits a particular morphology, that consist of a mixture of a nodular phase (a so-called cauliflower-like morphology) and a lamellae phase. The lamellar phase is present in low volume fraction relative to the dominant nodular phase. At higher magnification, Figure 6.1(b), it can be seen that those nodules are actually nodular clusters of various sizes, from 5 to 20 µm, with individual nodules sub-micron size.

During deposition, Zn^{2+} ions are predominantly transported to the steel surface through the collapse of the hydrogen bubble on which the ions ride. The rapid collapse corresponds to an extremely high transportation rate for Zn^{2+} ions. An instantaneous super-saturation condition for Zn^{2+} ions will develop on the steel surface, resulting in a high nucleation rate, thus, the nuclei do not have enough time to grow before a new nucleus forms on their surface. Therefore,

nanocristalline Zn coatings form. Similar porosity in Zn coatings has been observed during Zn electroplating [108, 109]. The preferential deposition of Zn during electroplating occurs at voltages below the H_2 evolution potential. The amount of porosity was reported to be influenced by the plating bath temperature, with inhomogeneous and spongy coating above 25ºC, in part due to the hydrogen evolution [110, 111]. In EPP electrolysis producing H_2 also occurs and the observed porosity can also be attributed to the H_2 evolution.

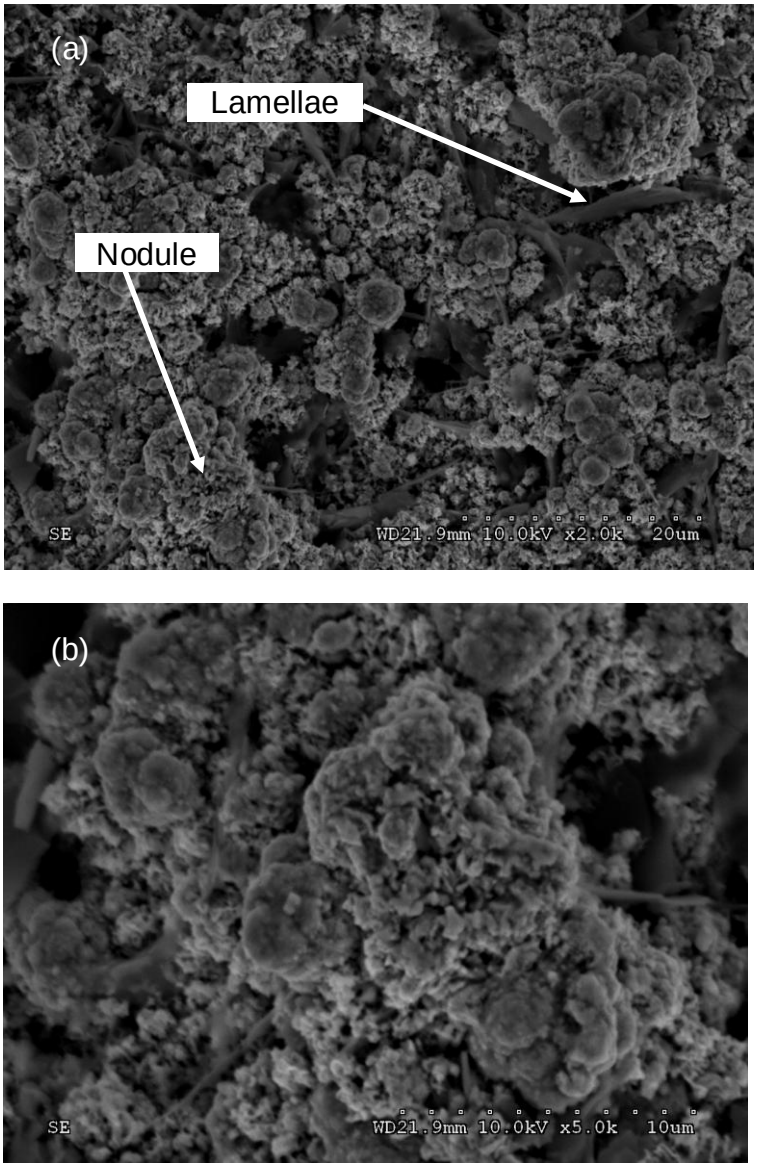

Figure 6.1 Top view surface SEM micrograph of Zn coating deposited with EPP (a) low mag. and (b) higher magnification featuring a nodule cluster.

Table 6.2 EDS analysis of surface composition of Zn coating of for the two features, nodule and flake.

Sampling location	Composition (at.%)	
	Zn	Fe
Nodule	96.5	3.5
Lamellae	95.0	5.0

To determine nodule/flake composition, EDS analysis was conducted. The results are reported in Table 6.2. It is evident that the two morphologies have a small variation in composition. Furthermore, given the inherent porosity and thickness (~30 μm) of the coating, it is reasonable to expect that Fe may be accounted from the substrate. Thus, the different morphologies may be attributed to crystal growth in different crystallographic directions.

Ni Coating

Figure 6.2 presents the top-view of the Ni coating. Certain features present on the surface can be observed at lower magnification, where the nodular character is prevailing. Under SEM observation, it can be seen that nodules have smooth surface with the exception of the higher summits, where small porosity is present. The orientation of the nodules is pilling up, suggesting that the ones closer to the electrode will undergo accelerated deposition due to a smaller anode gap, where as expected, discharges will occur faster. The uppermost nodules, Figure 6.2(b) are the result of the last discharge events and they are less than 1 μm in size. The resulting Ni coating, with a 3 μm thickness, is remarkably uniform, in agreement with previously reported work [112, 113]. The morphology is similar to Zn. The typical nodule is 2 – 5 μm with the top nodules in the sub-micron size.

Table 6.3 Surface composition of Ni coating of three locations: nodule, flat and full surface scan.

Sampling location	Composition (at.%)		
	Ni	Fe	O
Nodule	96.12	3.78	0.10
Flat	95.96	4.04	0
Full area	96.72	2.99	0.29

A semi-quantitative EDS analysis of the top surface features is presented in Table 6.3 as an average of surface nickel composition of the reported features considered of importance for

the coating formation in multiple stages (melting/solidifications cycles). The presence of some Fe may be due to the excitation volume from X-ray penetration depth through the coating and into the steel substrate. The low ratio of Fe to Ni suggests the coating is basically pure Ni, with the low amount of oxygen most likely the result of surface contamination.

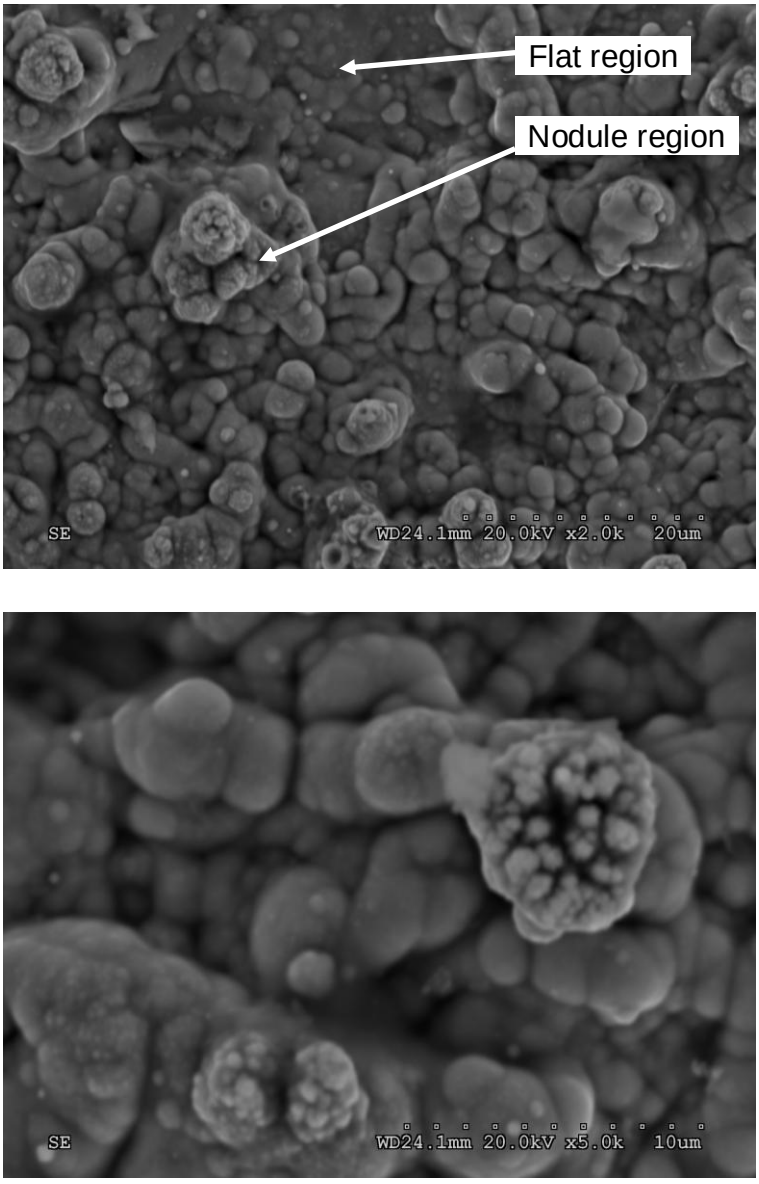

Figure 6.2 Top view surface SEM micrographs of EPP Ni coating (a) low magnification and (b) higher magnification of the surface features.

Mo Coating

In recent years, Mo has been considered as a potential candidate for replacement of chromium as a protective coating [118, 119]. The most common deposition method for Mo is plasma spray [120 – 127], but thermally sprayed coatings are usually inhomogeneous and discontinuous, characterized by large pores, oxide lamellas or partly molten spray particles [121].

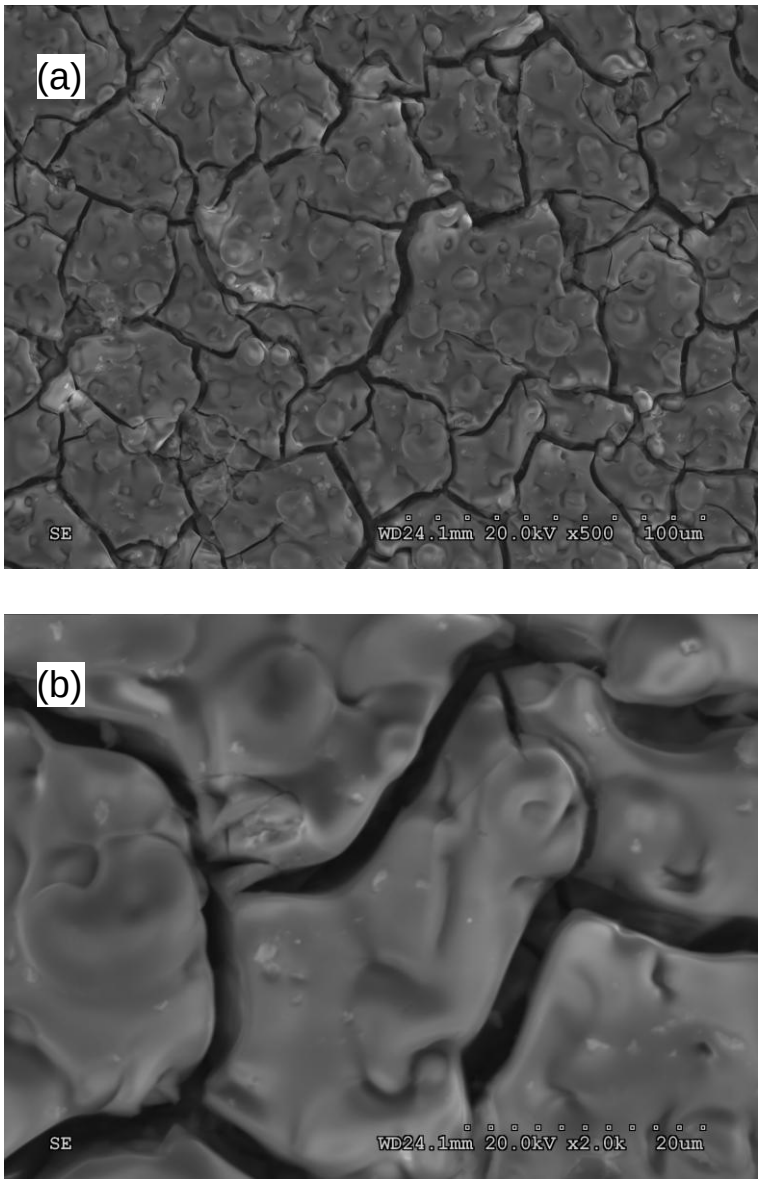

Figure 6.3 Top view surface SEM micrographs of EPP Mo coating (a) low magnification and (b) higher magnification of the surface features.

The Mo coating shows a flat surface, Figure 6.3, with regular deep cracks separating platelets like around ~50 μm in size. The morphology can be compared to that of dry mud. No distinct nodule-like features were present. The entirely different morphology suggests a different deposition behavior. Previous attempts to deposit Mo coating on stainless steel [40] have shown the propensity of Mo to alloy into the steel substrate instead of depositing as a separate layer (coating). The presence of cracks and especially in view of their regularity is likely the result of the difference in the coefficient of thermal expansion (CTE) of the deposited layers with respect to the steel substrate.

Table 6.4 CTE at room temperature for Fe and Mo.

Material	Crystal structure	CTE [μm/mK]
Fe	BCC	11.8
Mo	BCC	4.8

6.1.2. Surface Topography Analysis for Surface Parameters

Surface topography analysis was performed for all three types of coatings and the parameters defined in the previous chapter were studied.

R_a and R_z are average roughness and represent the highs and lows of the surface. In view of that, it can be seen from Figure 6.4 that Zn and Mo exhibit the highest roughness. This is due to their morphology, Zn with high hills and irregular heights, while Mo, although having relatively flat surface, deep cracks will be counted as lows in the roughness calculation, resulting in high values. However, if the surface regions between cracks are considered, roughness of Mo is low. With its particular morphology, Ni is positioning somewhere in the middle of the roughness spectrum, having higher hills comparable with those of Zn but virtually no valleys, such as only the “max” and not the “min” of the scanned surface were computed. Finally, the cleaned steel, with its low hills and small valleys (see previous chapter) has the lowers roughness value, ~10 times lower than Zn and Mo coatings, indicating a cleaning behavior of the previously surface mirror finish substrate. The roughness of Zn coating is intensified by its high deposition rate, as well as by higher plasma intensity on the newly formed hills, which adds up with each discharge cycle. Indirectly, if deposition rate can be controlled, porosity may be controlled as well.

R_{sk} represents the skewness of the profile, indicating whether the farthest points are above or below the mean surface level. For Zn, due to its closed-packed hills, the mean surface is considered the top of the hills, resulting in a negative value representing for the predominance of holes or valleys. Same is true for the Mo coating, where the average plane is the flat surface of the platelets, with the cracks counting for the negative R_{sk} parameter. In the case of Ni coating, the mean plane is the flat substrate, and the rounded hills giving a positive R_{sk} value.

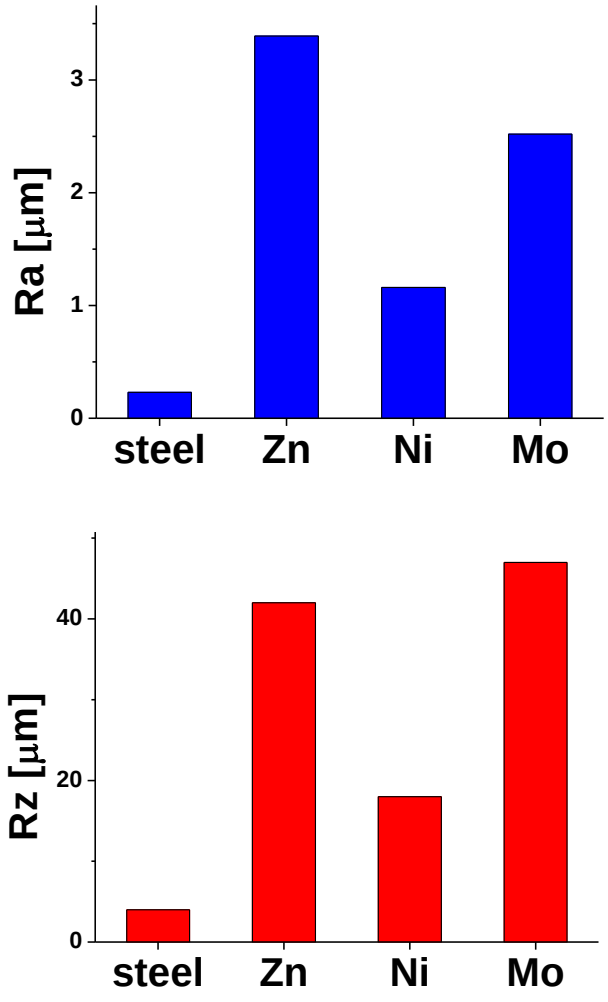

Figure 6.4 Ra and Rz parameters of the 3 coatings and cleaned substrate.

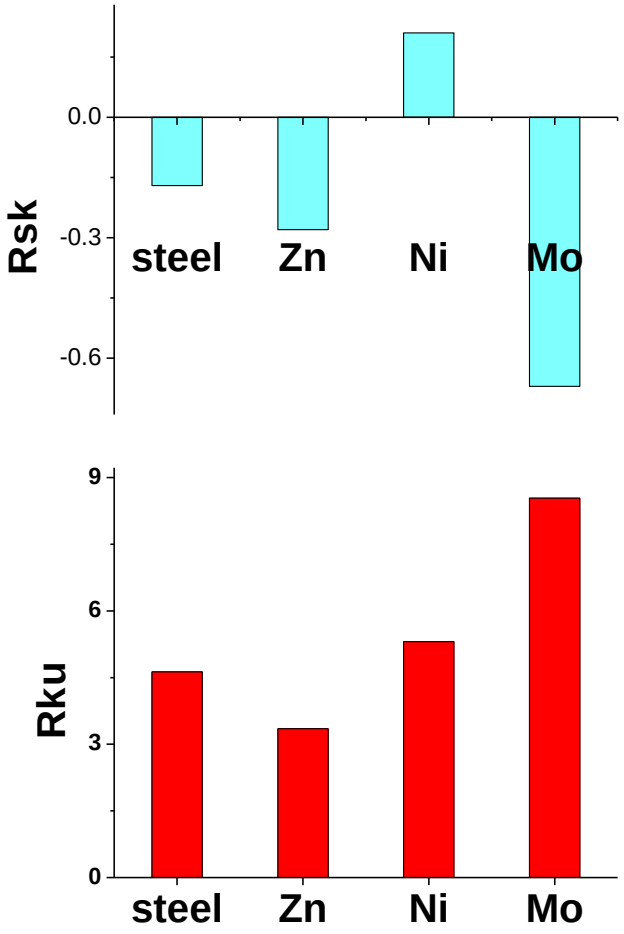

Figure 6.5 R_{sk} and R_{ku} parameters of the 3 coatings and cleaned substrate.

R_{ku}, the kurtosis, is representative for defects such as scratches. A random distribution is around R_{ku} = 3, which is the case for Zn and cleaned steel. A high R_{sk} value for Mo comes from the deep cracks while for Ni comes from the inordinate hills shaped surface.

6.1.3. Surface Topography Analysis for Volume Parameters

Compared to “cleaned” substrates, where all samples where exhibiting the hill/valley morphology, in the case of the three coatings, the volume parameters characterizing the shape and size of peaks/valleys are not a good approximation, not a basis for topography analysis.

Table 6.5 Surface and volume parameters for EPP deposited coatings.

Parameters	Cleaned steel substrate	Zn coating	Ni coating	Mo coating
Ra [μm]	0.23	3.39	1.16	2.52
Rz [μm]	3.96	42	18	47
Sm [nm^3/nm^2]	17	179	103	182
Sc [nm^3/nm^2]	356	4960	1750	3930
Sv [nm^3/nm^2]	33	534	184	444
Sbi	0.60	0.64	0.61	0.62
Sci	1.57	1.45	1.54	1.48
Svi	0.11	0.12	0.11	0.13
R_{sk}	-0.28	-0.28	0.21	-0.67
R_{ku}	4.63	3.35	5.31	8.54

Cleaned steel is the base and then deposition creates its own characteristics. Still the values in Table 6.5 show an agreement and numerically describe the surface coating morphology as observed by SEM. This is for Zn and Ni coatings where Mo numbers are biased due to cracking.

6.2 Investigation of the Structure and Composition

The phase structure and grain size of the three coatings was studied by XRD using a Siemens D-500 x-ray diffractometer with CuK_α radiation source. Particular detailed analysis was performed for the interface substrate – coating (previously labeled mixing zone). High resolution TEM on cross-section samples fabricated using the FIB lift-off technique was conducted to observe the structure and composition at the mixing zone. X-ray mapping was conducted on the cross-sectional TEM coatings. Selected Area electron Diffraction (SAD) patterns were recorded and Fast Fourier Transformation (FFT) on HRTEM DP were calculated and studied for phase identification.

Zn Coating

A standard X-ray diffraction θ-2θ scan was performed to ascertain the crystal structure of the Zn coatings. Figure 6.6 depicts a typical XRD pattern of the Zn coating. The peaks were indexed to Zn with a hexagonal structure and Fe with a BCC structure. The peaks from Fe arise

from the steel substrate. The intensity ratio of the (101) peak to (002) peak is 5, which is much higher than the ratio of 1.89 from randomly oriented Zn powder. This indicates that the Zn coatings exhibit a (101) preferred orientation.

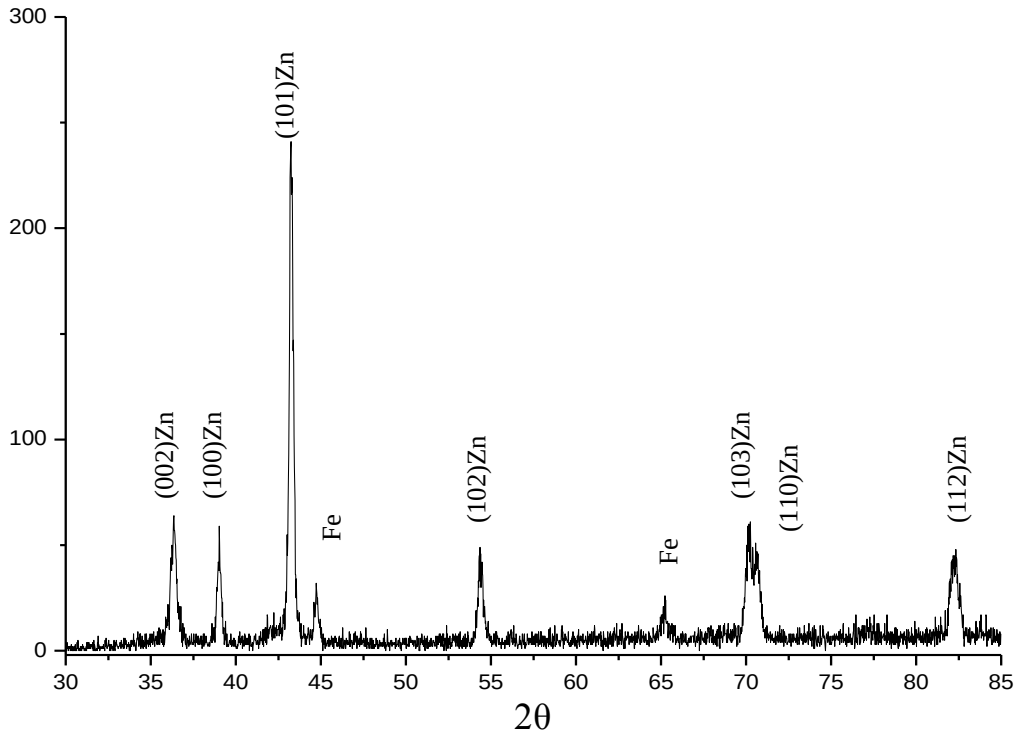

Figure 6.6 X-ray patterns of Zn coatings from a θ-2θ scan.

In addition, 2θ scans by fixing the glancing angle in the range of 0.5 – 15° were conducted to investigate the phase structure of the coatings at different depth. The method is used because the penetration depth of the X-ray decreases with reducing glancing angle. To quantify the change of the peak position and width with glancing angle, the XRD (101) peak of Zn from different glancing angle was fitted with Gaussian function. There is no significant change in the peak position, while the FWHM of the (101) peak of Zn increases almost linearly from 0.19º to 0.57° as the glancing angle is reduced from 21.6º to 0.5°, as shown in Figure 6.10. It is well accepted that the broadening of the XRD peak could result from the decrease of the grain size or the strain in the coating.

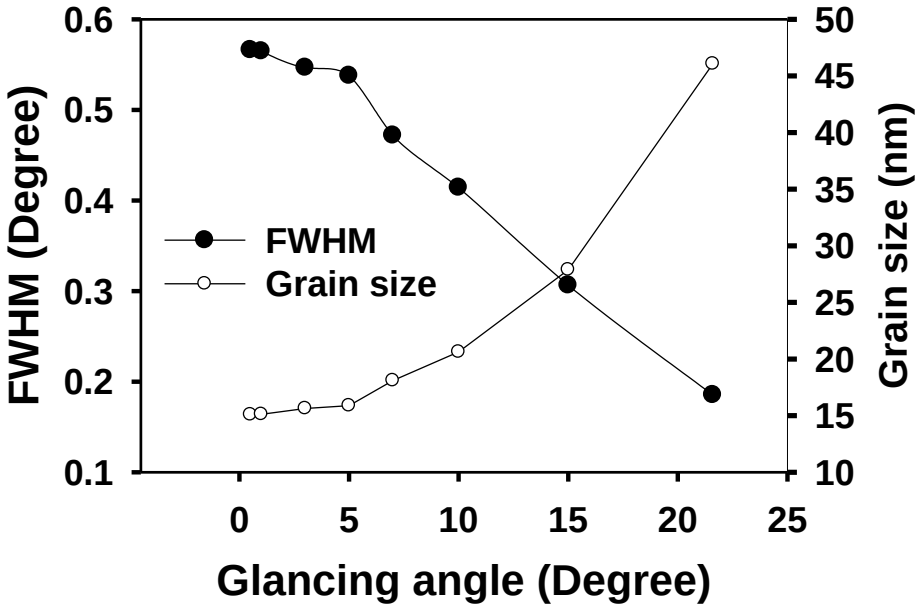

Figure 6.7 Dependence of the FWHM of the (101) peak of Zn and the calculated grain size of Zn coating on the glancing angle.

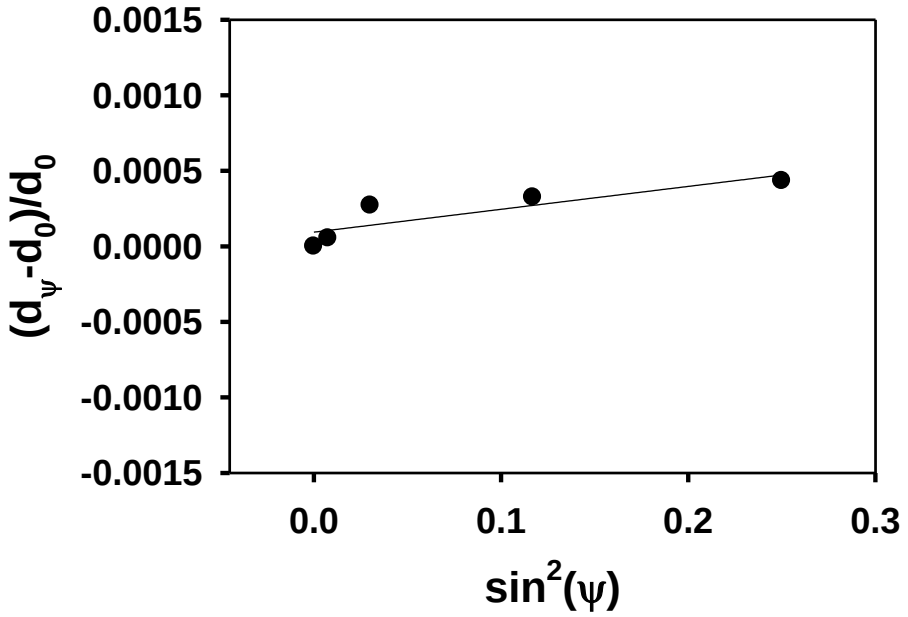

Figure 6.8 $(d_\psi - d_0)/d_0$ vs. $sin^2(\psi)$ plot for the (114) Zn reflection.

The grain size was calculated using Scherer equation and the calculated average grain size at different glancing angle is also shown in Figure 6.7. At a glancing angle below 5°, the grain size of the Zn coating is only about 15 nm. At such a small glancing angle, only the top surface of the Zn coating contributes to the XRD pattern, implying the nanosize of the grains on the top surface layer of the Zn coating. The gradual increase of the grain size with glancing angle indicates a gradual increase of grain size with depth. This in fact is similar to the observations in cleaned surfaces indicating a similar effect of annealing.

The internal stress in the EPP-deposited Zn coatings was measured by a standard $d_{hkl}(\psi)$ versus $sin^2(\psi)$ method using XRD, where ψ is the angle between the diffraction plane and the sample surface and $d_{hkl}(\psi)$ is the lattice spacing measured at different ψ angle. By calculating the slope of the $(d_\psi - d_0)/d_0$ vs. $sin^2(\psi)$ plot, Figure 6.8, the internal stress in the Zn coating was determined to be +108 MPa. The positive sign indicates that the *tensile* nature of the stress in the Zn coatings, which is common for metallic films or coatings deposited by different techniques. The low stress value indicates a possible annealing effect during processing, a common phenomenon for low T_M metals (as seen in Chapter 5).

Table 6.6 Room temperature CTE values for different axis; units are in [μm/m*K].

Metal	Crystal structure	CTE “c” axis	CTE “a” axis
Zn	HCP	63.9	14.1

The coefficient of thermal expansion (CTE) varies significantly for Zn between the “c” axis and the “a” axis, as shown in Table 6.6. Reynolds and Hilty [125] suggested that this difference in CTE may explain the propensity for Zn coating to exhibit a preferred orientation. This anisotropic CTE behavior may result in the stress build up during thermal cycling [126], and in part explain the low stress value found above.

Figure 6.9 illustrates the cross sectional secondary electron image of the Zn coating. During sample preparation with FIB, due to large Zn coating thickness, the top of the coating was carved out in order to allow the lift-off procedure. At low magnification, Figure 6.9(a), it can be seen that the steel substrate consists of two zones: the top zone is influenced by the heat from

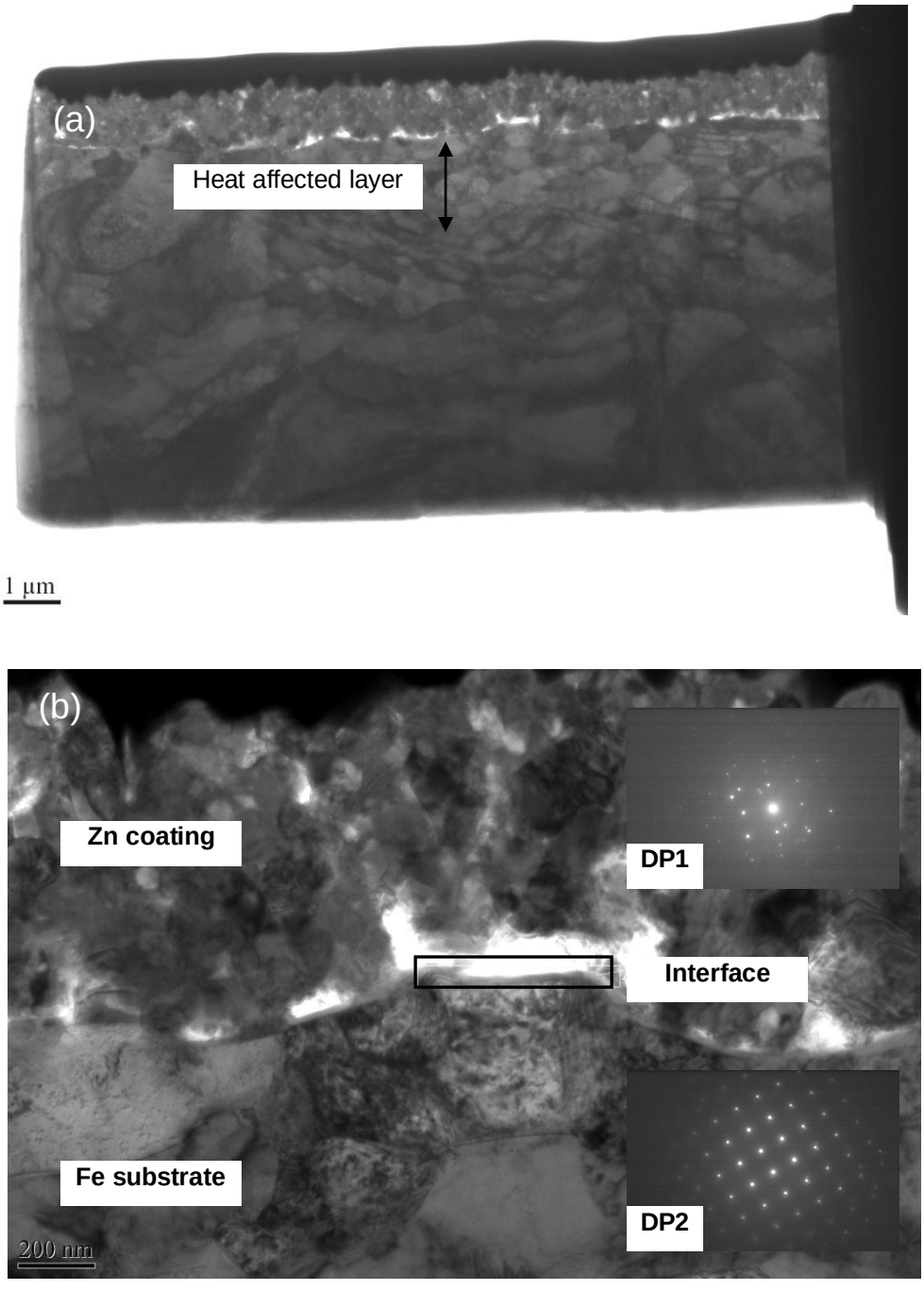

Figure 6.9 Typical cross sectional TEM images of EPP deposited Zn coating;
(a) overall view of the coating, including unaffected substrate bulk and;
(b) higher magnification with the interface layer; inset shows the corresponding selected area electron diffraction pattern from Zn coating and Fe substrate away from interface

the plasma and as expected, it will melt and solidify as presented previously in the “cleaning” process. The grain size in the heat affected layer is in the submicron range (~500-800 nm), Figure 6.9(b), while the bulk substrate remains in the micron range. As for the deposition of Zn, it can be observed that the interface formed is highly porous, with voids 50 – 200 nm, comparable in size with the subsequent deposition grains. The formation of this porous interface is expected to be the result of collapsing of the bubbles that entraps gases and forms “bridges” on top of these pockets. Subsequently, the fast deposition of Zn will entrap those pockets while the fast cooling action of the electrolyte will generate high nucleation rate of formation for Zn grains followed by a recovery that will be limited by the short processing time. The electrolyte will act as the cooling agent, and the heat transfer will be almost instantaneous and the coating will settle for the electrolyte bath temperature.

TEM was used to further explore the crystalline structure and microstructure of the Zn coatings. Figure 6.9(b) shows that the Zn coating consists of irregular shaped, almost compact grains with a size of about 20-100 nm. The insets in Figure 6.9(b) present the DP pattern of the Zn coating (DP1) and Fe substrate (DP2) respectively, away from the interface.

In Figure 6.10, the respective (hkl) of principal spots from the diffraction patterns are indexed and presented in detail. The diffraction spots in DP1 correspond to (100), (101) and (310) planes of Zn with hexagonal crystal structure and those in DP2 correspond to (110), (200) and (310) diffraction planes of body centered cubic Fe.

EPP process can be compared to the process of galvanizing. The steel substrate and the Zn coating are subject of melting/solidification while in contact through the interface, followed by annealing. It is well documented that during galvanizing of steel from molten Zn bath, depending on the annealing temperature, processing time and steel grade, as well as other parameters, various intermetallic Zn/Fe phases are formed at the interface [109, 122, 123]. As a result of the short processing time and high temperatures that are characteristic to EPP, it is expected that some similar reactions may occur.

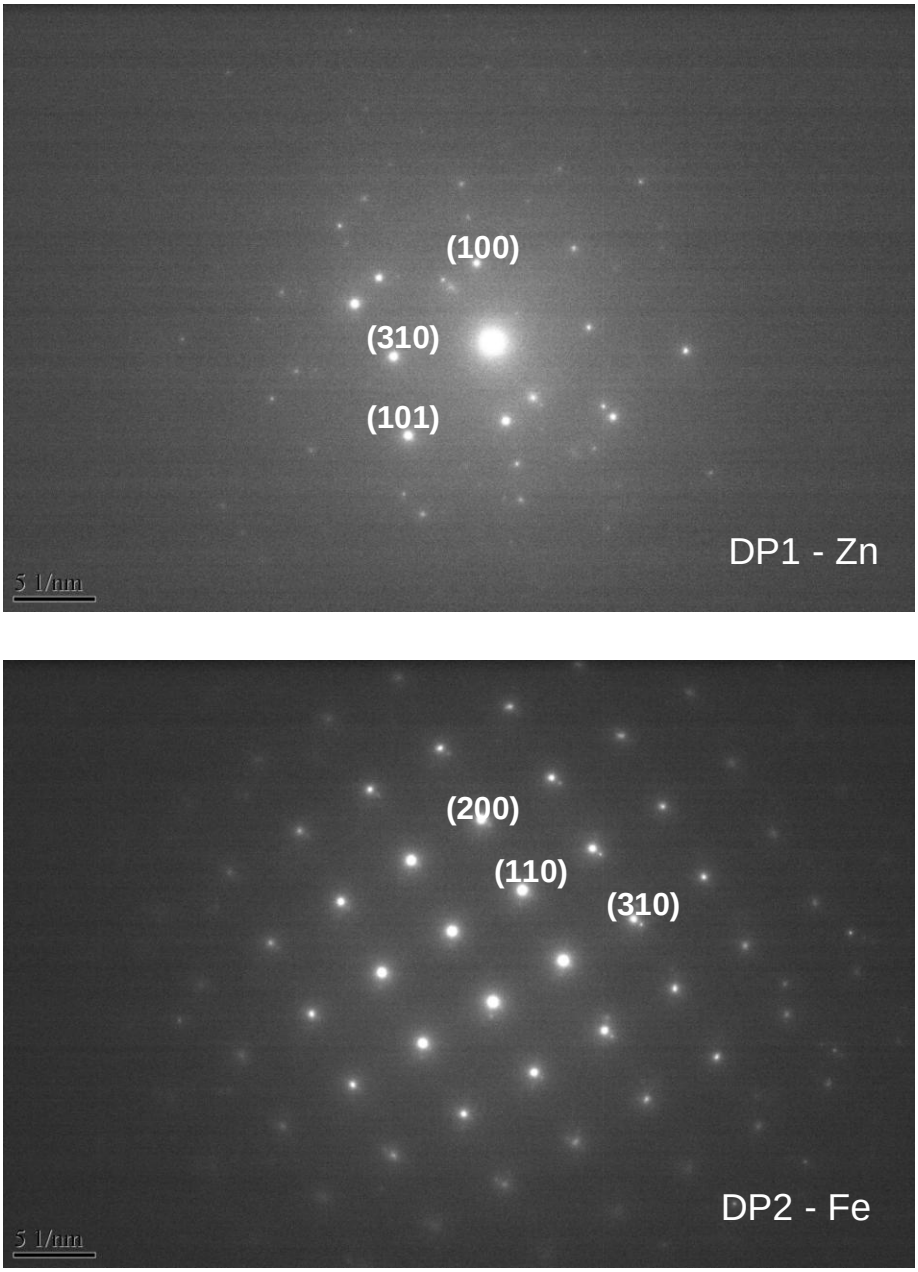

Figure 6.10 Indexed diffraction patterns for Zn coating and Fe substrate, away from the interface.

Table 6.7 Characteristics of Fe-Zn intermetallics [109].

Phase	Composition, at.% Zn	Crystal structure	Lattice parameters, Å
Γ (Fe_3Zn_{10})	68.5 – 82.5	bcc	a = 8.932
$Γ_1$ ($Fe_{11}Zn_{40}$)	75 - 81	bcc	a = 17.98
δ ($FeZn_{10}$)	86.5 – 91.8	hcp	a = 12.83 c = 57.72
ζ ($FeZn_{13}$)	92.8 - 94	monoclinic	a = 10.86, b = 7.608 c = 5.061, β = 127.3°

Table 6.7 presents the expectations based on thermodynamic equilibrium and previous work. In addition, the Fe-Zn phase diagram, Figure 6.11, can be utilized to assist the analysis of the EPP coating – substrate interface.

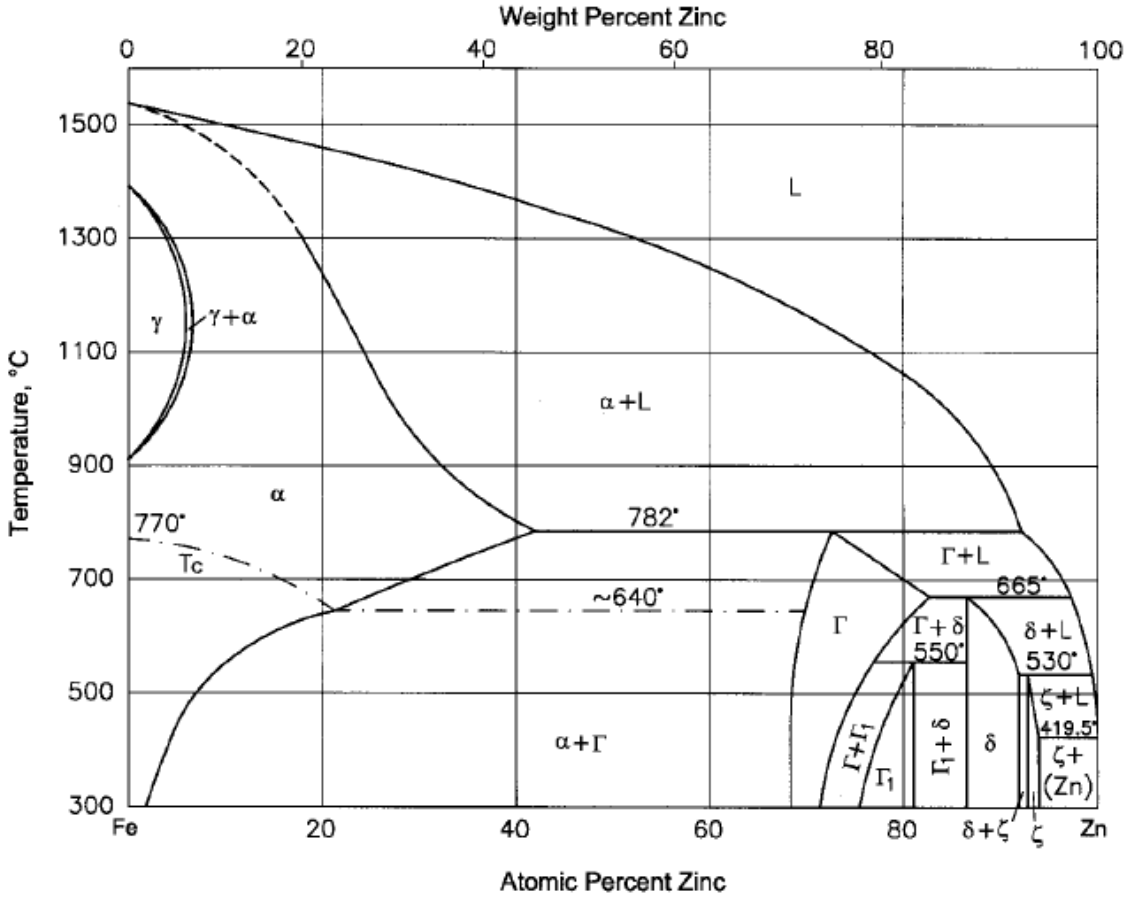

Figure 6.11 Fe-Zn phase diagram [128].

Figure 6.12(a) presents a TEM view of a cross-section of the coating specially prepared so that the interface between the substrate and coating can be distinguished with ease. At higher magnification, Figure 6.12(b), the interface layer thickness can be estimated at around 100 nm. Inset diffraction pattern in Figure 6.12(b) was taken from the interface.

Following the same procedure as for Zn and Fe, the diffraction patterns originating from the interface were indexed. A typical ED Pattern from the interface is shown in Figure 6.13. The Zn and Fe diffraction spots from the coating and substrate were first identified and eliminated from the analysis. The remaining EDP spots representing phases present at the interface were then indexed. The identification of the remaining d-spacing were compared with standards (Appendix1) and labeled accordingly. The results are shown in Table 6.8. The ED analysis suggested the presence of two phases at the interface, namely ζ and Γ_1. As shown in the phase diagram, both are Zn-rich phases with approximate stoichiometries $FeZn_{13}$ (ζ) and $Fe_{11}Zn_{40}$ (Γ_1).

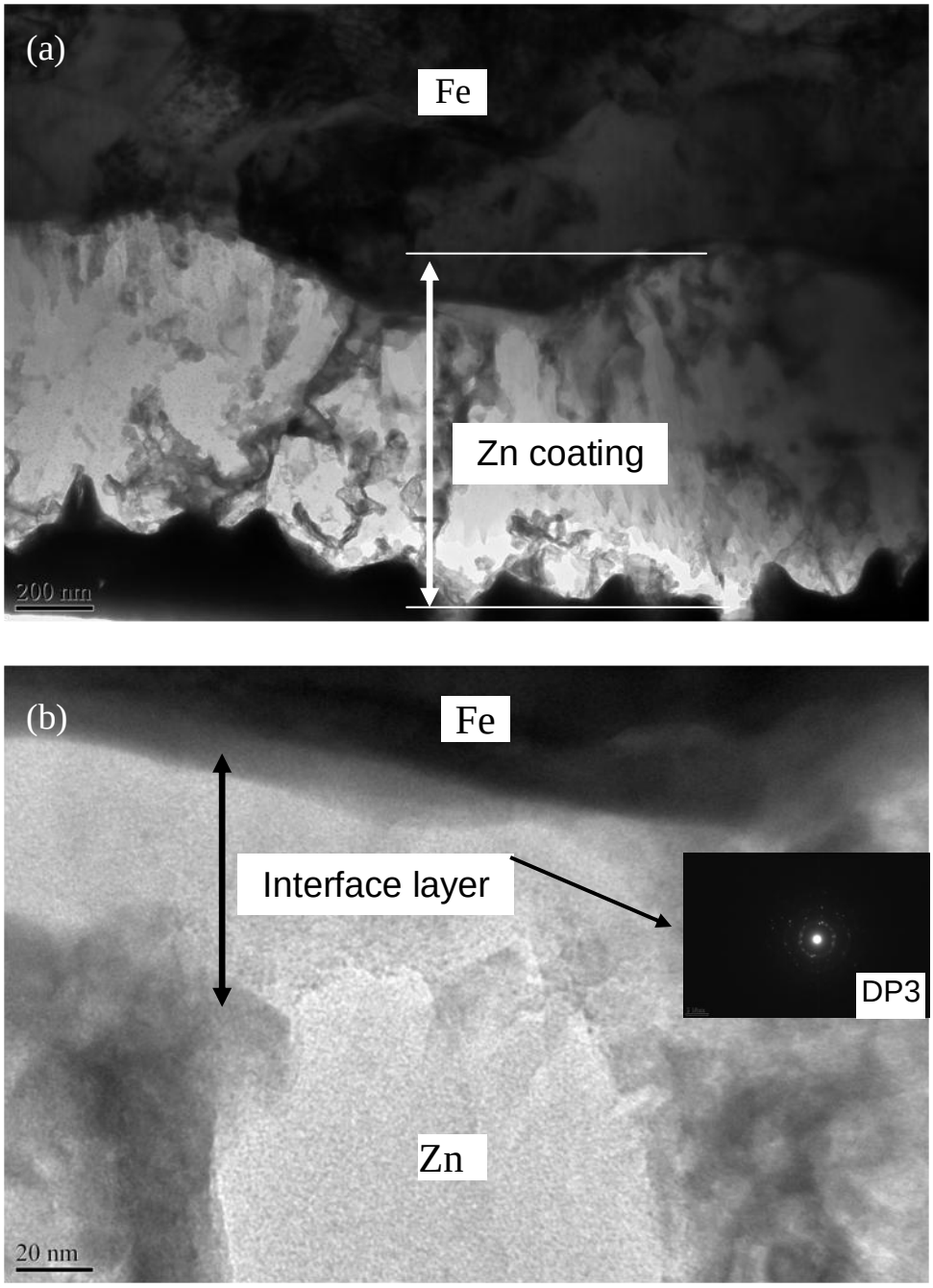

Figure 6.12 TEM images of Zn coating (a) Bright Field micrograph of the Zn coating and steel substrate, (b) higher magnification Bright Field micrograph of the interface layer; inset Diffraction Patterns of the interface layer.

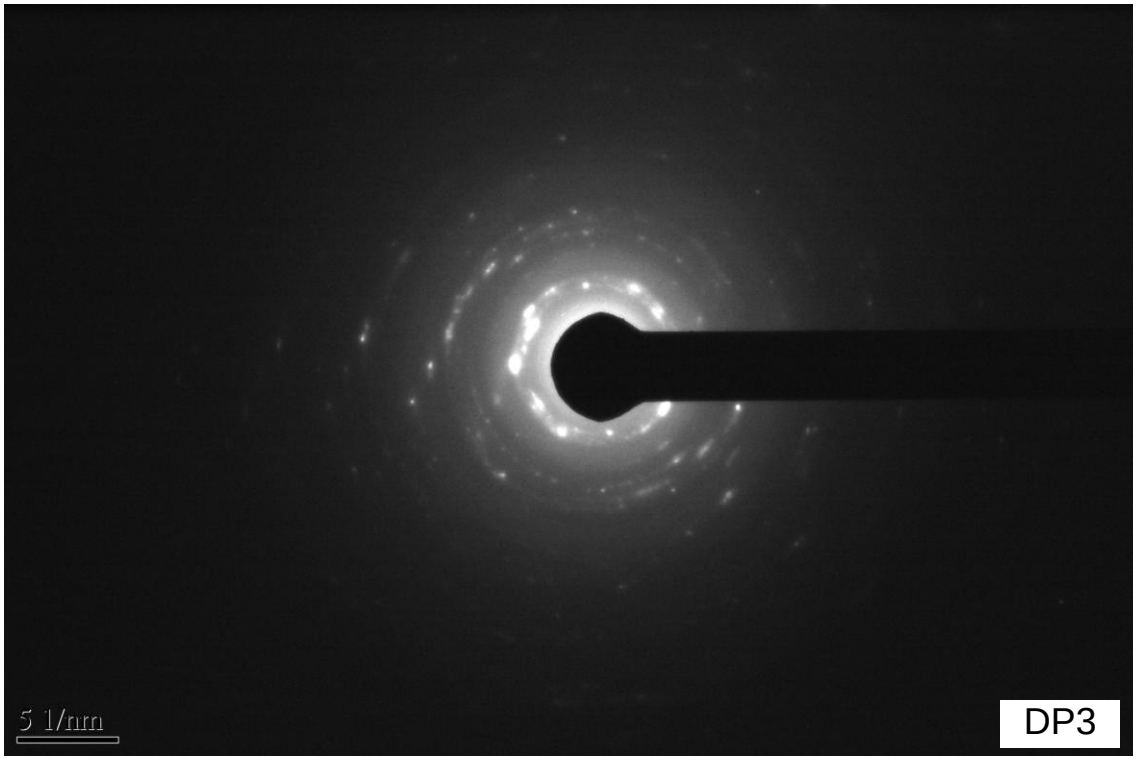

Figure 6.13 Diffraction pattern originating from the interface (DP3).

A more detailed study was conducted at the interface region. Several HRTEM images from the same area of the interface were acquired. The FFT function was applied to those and the resulting diffraction patterns were indexed. Phase identification was conducted by matching the d-spacing from FFT with standard “pdf files” for all known phases that appear in the Fe-Zn phase diagram. This is a database of diffraction peaks for each phase.

Two HRTEM images from the interface region are shown in figure 6.14. The FTT analysis for these two images produced a DP consistent with the ζ phase (DP4) and Γ_1 phase (DP5), respectively. Furthermore, the HRTEM images for these two phases show a grain size of about ~ 10 nm. Thus, the FFT result was a very good match with ζ and Γ_1 intermetallics, Table 6.8 and Appendix 1.

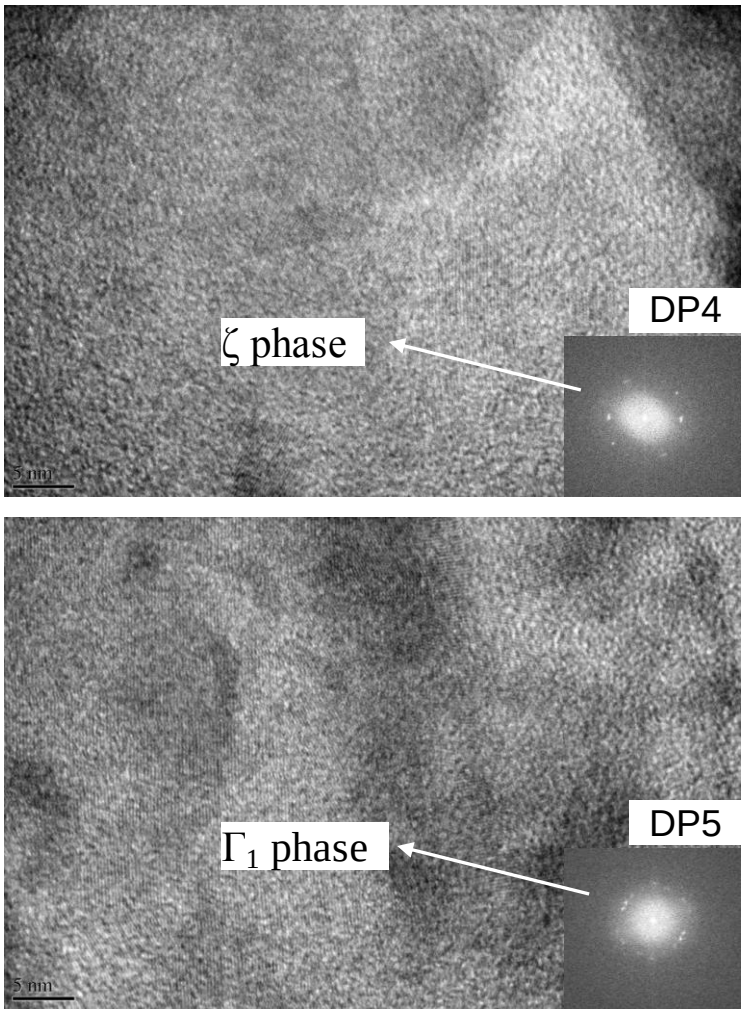

Figure 6.14 HRTEM images from the interface and FFT corresponding calculated diffraction patterns.

Table 6.8 Phase identification for interface diffractions patterns using standard d-spacing (appendix 1).

d-spacing	DP3 (interface) + identification		DP4 (HRTEM)	DP5 (HRTEM)
d1	2.704	**ζ or Γ_1**	2.783	2.821
d2	2.495	**ζ or Γ_1**	2.456	2.490
d3	1.831	**ζ or Γ_1**	2.483	2.437
d4	1.569	**ζ or Γ_1**		
d5	1.432	Fe		
d6	1.326	Zn		
d7	1.185	Fe		
d8	1.104	Zn		
d9	0.891	Fe		
Phase identification			**ζ**	**Γ_1**

A TEM/EDS analysis was also conducted in the interface layer. Table 6.9 summarizes the elemental composition in the vicinity of the interface. This can be viewed as a qualitative evaluation of the chemical composition around the interface layer, extending about 200 nm in both substrate (Fe) and coating (Zn) sides. It was found that about the same amount (at.%) of Fe and Zn are present in the respective layers. The interface elemental composition is ~ 16.8 at.% Fe. The two phases found at the interface have a large variation in Fe, between 8% - ζ to 20% - Γ_1. In view of the fact that the average interface contains ~ 17 at.% Fe, it is expected that the two phases were relatively equally distributed in the interface region.

Table 6.9 Composition of the interface mixing zone, ± 200 nm towards Zn coating and steel substrate.

Sampling location	Zn at.%	Fe at.%
Zn side interface	90.70	9.30
Interface	83.20	16.80
Fe side interface	10.0	90.0

Ni coating

Figure 6.15 is a scanning electron micrograph of Ni coating cross-section. The micrograph shows a dense structure, with low porosity and 3 μm thick uniform coating. The cross-section was carved and “polished” by FIB.

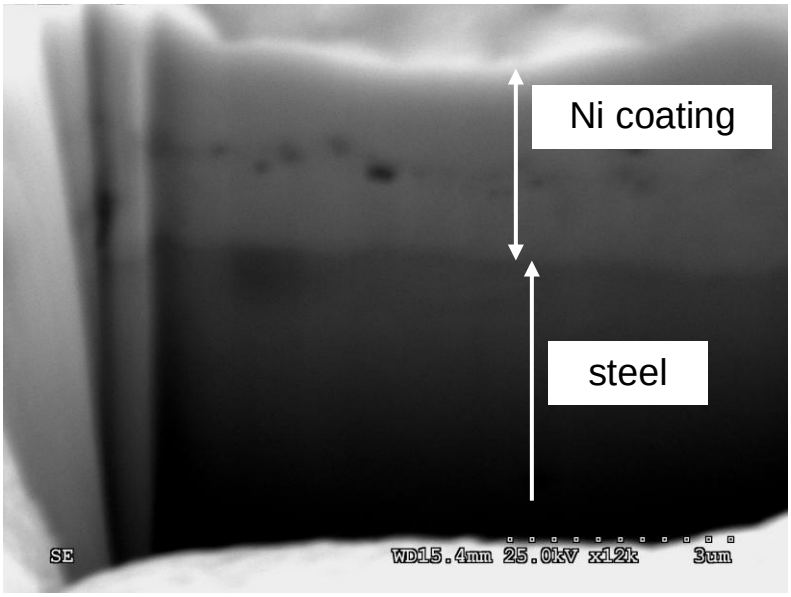

Figure 6.15 SEM micrograph of Ni coating deposited by EPP.

Standard XRD θ-2θ scan analysis was performed in the Ni coated substrate. Figure 6.16 depicts a typical XRD pattern of the Ni coating. The peaks were indexed to FCC Ni with characteristic peaks at (111), (200) and (220). No Fe peaks were found which suggest the mixing zone is limited to the near interface with the substrate. The lack of additional Fe peaks from the substrate (compared to Zn coating) may be the result of Ni high density and relatively low porosity compared to Zn coating.

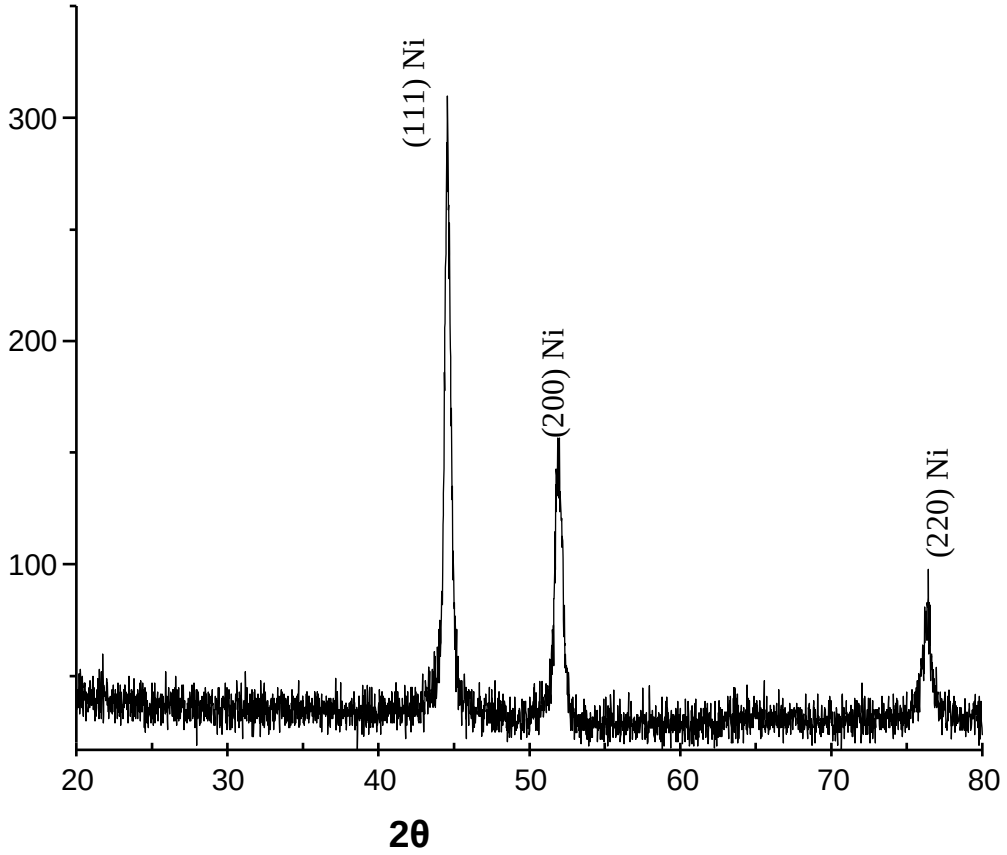

Figure 6.16 X-ray diffraction patterns of Ni coatings from a θ-2θ scan.

Cross-sectional TEM analysis, Figure 6.17(a) reveals the presence of several layers: an upper coating region which has limited porosity, and a lower coating layer close to the substrate (interface) that is uniform, with `0.5 μm grain size and 1μm thickness. Figure 6.16(b) shows the distinct interface region, ~ 800 nm thick.

To help identify the different phases present at the interface, TEM analysis was performed and representative diffraction patterns were acquired, figures 6.18 and 6.19, from the

area of interest: DP1 and DP2 – diffraction pattern from the interface only, and DP3, DP4 respectively, away from the interface, in two directions, toward Ni (coating) – DP3 and toward Fe (substrate) – DP4.

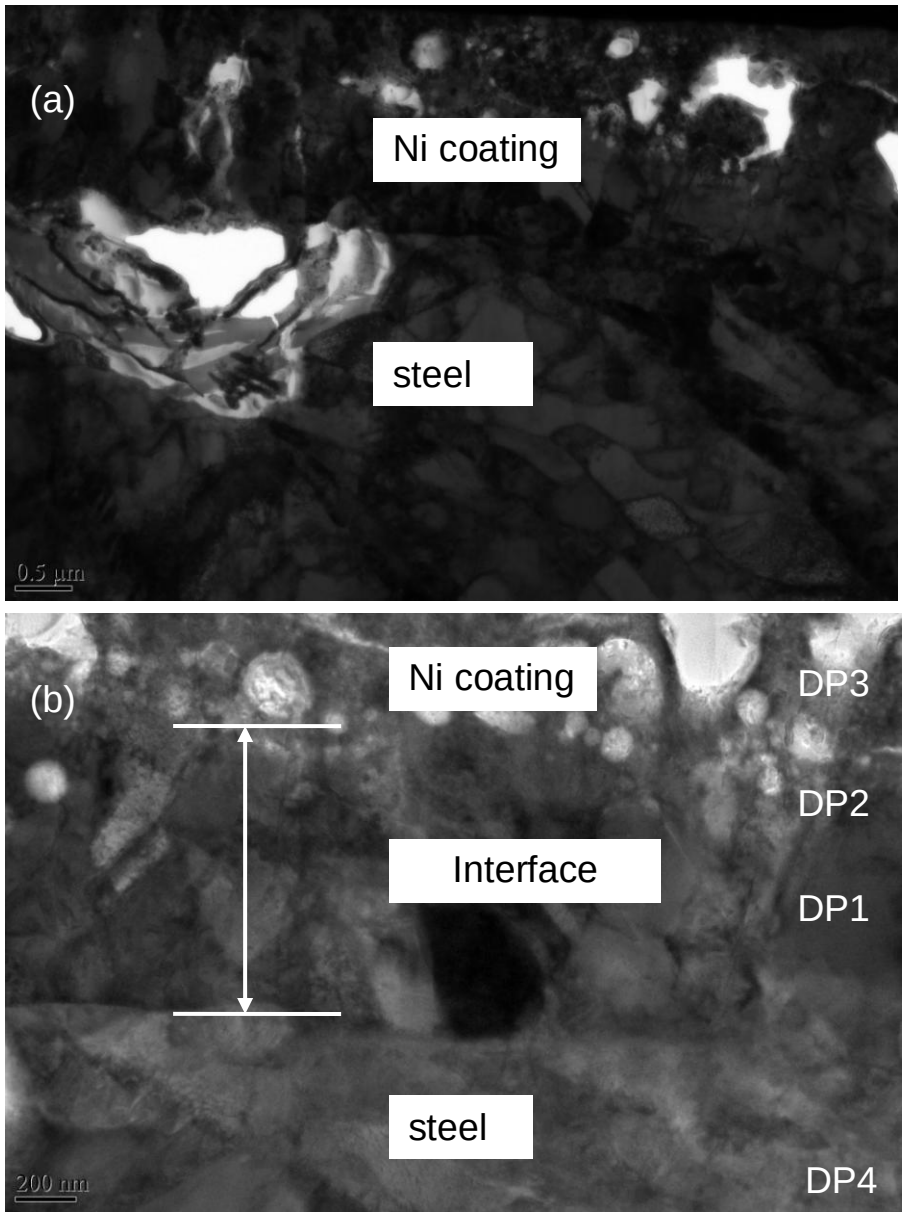

Figure 6.17 Cross-sectional TEM on Ni coating deposited with EPP, (a) showing an overall view of the coating and the substrate, (b) distinct layers, including the interface; Diffraction patterns positions are indicated by DP1, DP2 at the interface, DP3 inside Ni coating and DP4 inside Fe substrate respectively.

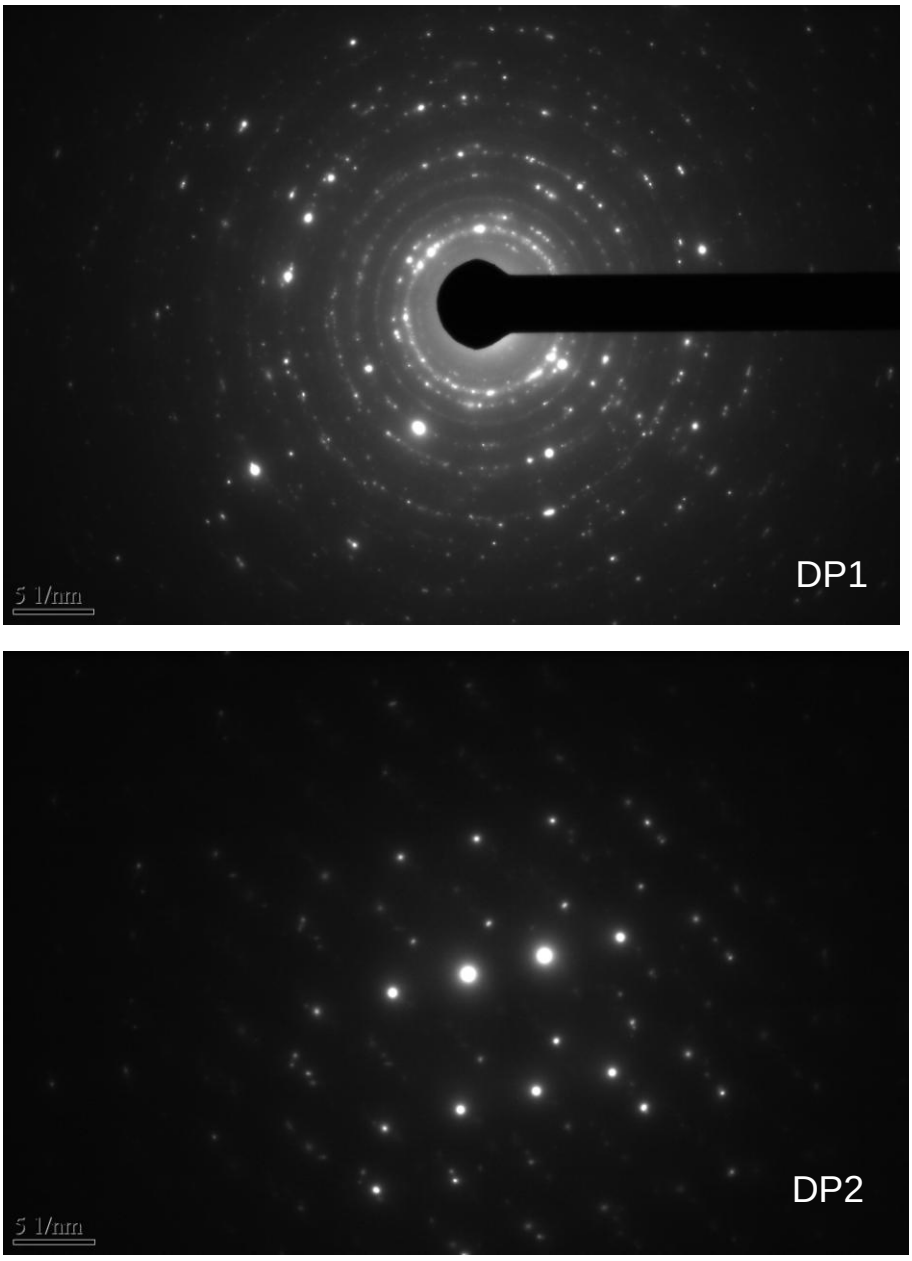

Figure 6.18 Diffraction patterns from the interface locations that are representative for the phase composition of the interface.

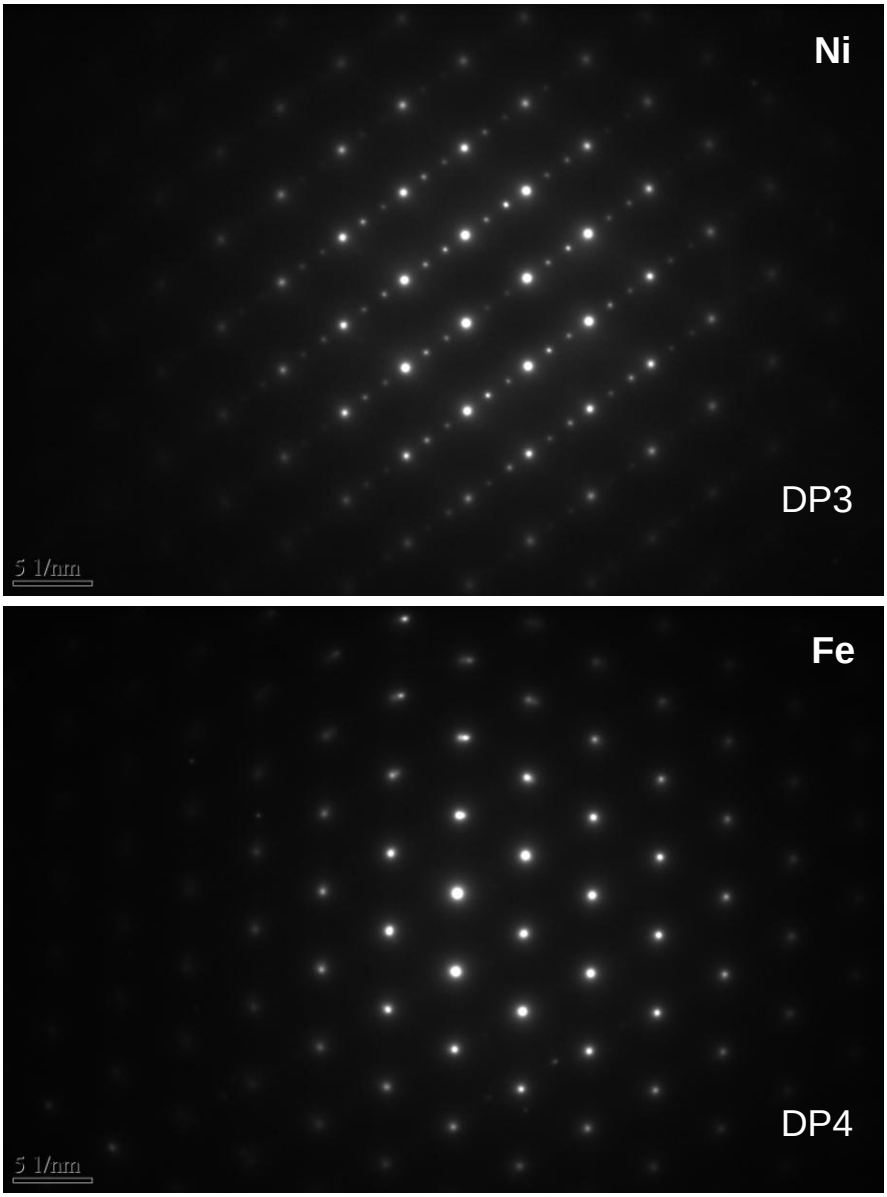

Figure 6.19 Diffraction patterns away from the interface, DP2 from Ni coating and DP3 from Fe substrate.

Table 6.10 d-spacing for DP 1 and DP2 and phase identification.

d-spacing	DP1 - interface	DP2 - interface	DP3 – Ni coating	DP4 – Fe substrate
d1	2.023 - Fe	2.949 – $FeNi_3$	2.037 – Ni	2.018 – Fe
d2	1.748 – Ni	2.494 – $FeNi_3$	1.760 - Ni	1.155 – Fe
d3	1.474 – Fe	2.066 – $FeNi_3$	1.254 - Ni	0.762 – Fe
d4	1.225 – Ni	1.470 – $FeNi_3$		0.559 – Fe
d5	1.044 – $Fe_{0.64}Ni_{0.36}$	1.378 – $FeNi_3$		
d6	0.793 - $Fe_{0.64}Ni_{0.36}$	1.195 – $FeNi_3$		
d7	0.708 - Ni			

The four diffraction patterns were indexed and the results are presented in Table 6.10. The interface (DP1 and DP2) is composed of two phases, one Ni rich phase - $FeNi_3$ and one Fe rich phase, $Fe_{0.64}Ni_{0.36}$. Ni and Fe diffractions are still present, as expected, since some limited X-ray diffraction will occur outside the interface into the Fe and Ni layers.

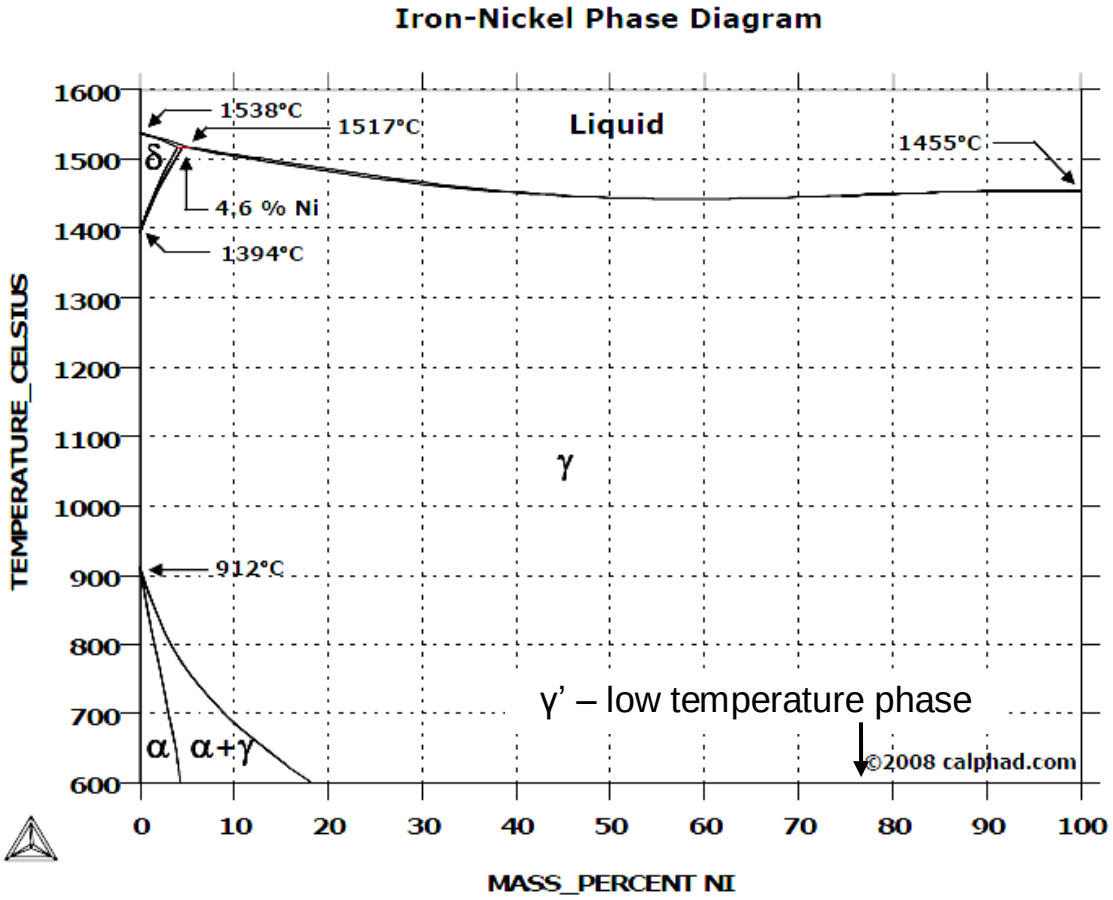

Figure 6.20 Fe-Ni phase diagram [128].

Figure 6.20 presents the Fe-Ni equilibrium phase diagram. The phase diagram shows complete solid solubility. The two phases identified at the interface are N—rich γ' phase (FCC) and Fe-rich γ phase (FCC). According to the phase diagram, Fe and Ni are soluble at high temperature. The result suggest that upon quenching, γ' forms close to the Ni side of the interface and metastable γ close to the substrate side (Fe). Since EPP creates the conditions for fast cooling rates, equilibrium will not be achieved at the interface, and the two phases will be both present.

TEM/EDS elemental analysis was performed at the interface. The extent of the mixing zone was found to be less than 1 µm, as observed in Figure 6.17(b). The EDS analysis results are presented in Table 6.11. The results show significantly more Ni (~ four times) is present in the substrate side of the interface than Fe in the coating side of the interface. This can be explained by the surface layer evolution. During deposition, the top layer of the Fe substrate melts and will form a mixing zone with the incoming Ni from the electrolyte. As coating deposition progresses, the melting surface layer moves away from the substrate and eventually forms the coating. Therefore, there will be less available Fe atoms into the melt. The solidified coating left behind will be a mixture of Fe and Ni, where Ni eventually takes over the molten top layer and deposits as Ni coating. It should be noted that this sequence of coating evolution is possible due to similar T_M points for the substrate and coating materials. This process of coating building explains why the diffraction pattern in Figure 6.16 shows Ni peaks only. Although Ni coating is not thick (~3 µm), the absorption coefficient for x-ray by Ni is high and the X-ray will not penetrate the coating to the Fe substrate.

Table 6.11 EDS composition of interface on both sides of a virtual median line crossing through the interface ±0.5 µm into the Ni coating and steel substrate.

EDS sampling location	Composition (at.%)	
	Ni	Fe
Coating side interface, Ni rich	94.00	6.00
Substrate side interface, Fe rich	26.10	73.90

Mo coating

Microstructural analysis of the Mo coating cross sections was carried out using SEM. Figure 6.21 presents a typical cross section of the Mo coating. Elemental composition was determined by EDS along the cross-section of the coating/substrate. The measurements were performed at equal intervals in the probing areas 1 to 6, as seen in Figure 6.21. One additional reading was taken along the interface (area 7).

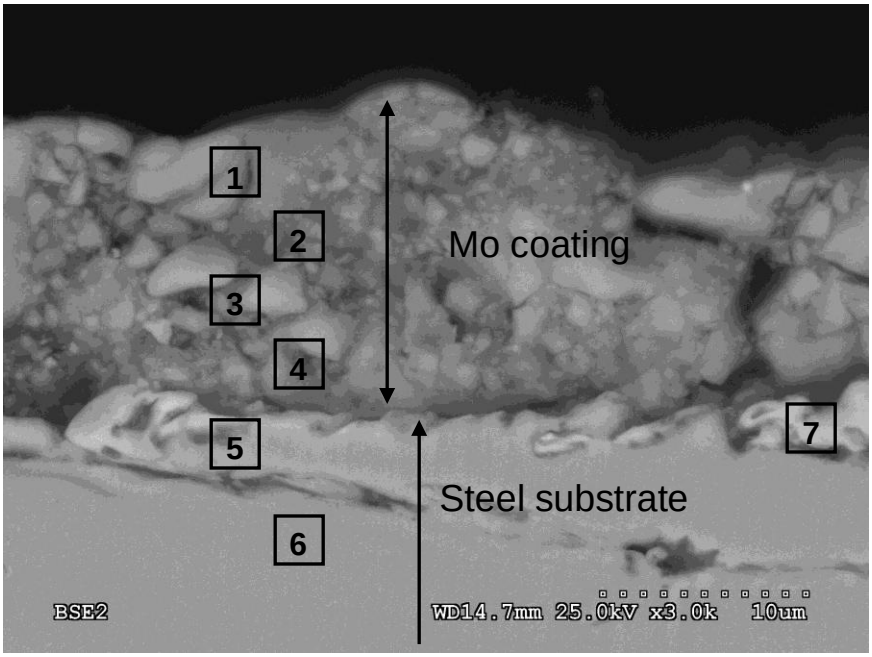

Figure 6.21 Backscattered electron (BSE) image of a cross-section EPP of Mo coating showing the location of the EDS probe location along the interface coating – substrate.

The EDS analysis results are presented in Table 6.12. It appears that extensive mixing of Mo and Fe occurs during processing. It is evident from the EDS results that the Mo coating has a relatively uniform composition, within 6 – 9 at.% Fe. There is also evidence of randomly dispersed higher Fe phases that can be related with known intermetallics from Fe-Mo phase diagram, Figure 6.22. Furthermore, probe 7 gives an indication on the nature of the upper most layer of the substrate. This layer was found to contain Fe and Mo at a 2:1 ratio suggesting the presence of the stoichiometric hexagonal Fe_2Mo phase (C14 type Laves phase) [130].

Table 6.12 EDS spectra and chemical composition analysis along the coating thickness and near-interface substrate based on Figure 6.21 EDS probing locations.

Probe location	Mo [at.%]	Fe [at.%]	Mo [wt.%]	Fe [wt.%]
[1]	93.5	6.5	96	4
[2]	91	9	94.3	5.7
[3]	66.3	33.7	77.2	22.8
[4]	91	9	94.5	5.5
[5]	14	86	22	78
[6]	0	100	0	100
[7]	35	65	48	52

The Fe-Mo phase diagram was assessed by [129] and updated by [130]. There are four intermediate phases in this system: σ, R, μ (Fe_7Mo_6), and the λ phase Fe_2Mo. The σ and R phases form through peritectic reactions and decompose through eutectoid reactions at or above 1200 °C. The μ and λ phases form in the solid state and are stable at low temperatures. The EDS results show that extensive mixing of Mo and Fe occurs during processing. It is evident that the Mo coating contains 6-9 at.% Fe throughout its thickness. There may also be randomly dispersed intermetallic phases as for example in probe 3. This region may be composed of α (Mo) and μ (Fe_3Mo_2) phases producing an average composition of about 66 at.% Mo.

The significant incorporation of Fe in the Mo coating may be attributed to its higher T_M compared to Fe. During processing, molten Fe is expected to be continuously present while Mo atoms arrive and deposit on a “floating” surface. This particular environment will tend to enhance Fe atom diffusion into the Mo rich regions (coating) impending in a sense the deposition of a pure Mo coating. Furthermore, the plasma action is expected to continuously melt the top layer further enhancing mixing and transport of Fe atoms to the upper surface layer. As more Mo atoms arrive at the surface with processing time while Fe interdiffusion continues, has as a result the formation of an extended interface instead of a pure Mo coating.

This seems to provide a plausible explanation for the observed cracking. A rough estimate shows that the volume fraction of the cracks is about 10% of the coating volume. A possibility is that the crack volume was filled with liquid Fe which finally diffused into the originally pure Mo regions resulting in an overall coating composition with about 6-9 at.% Fe.

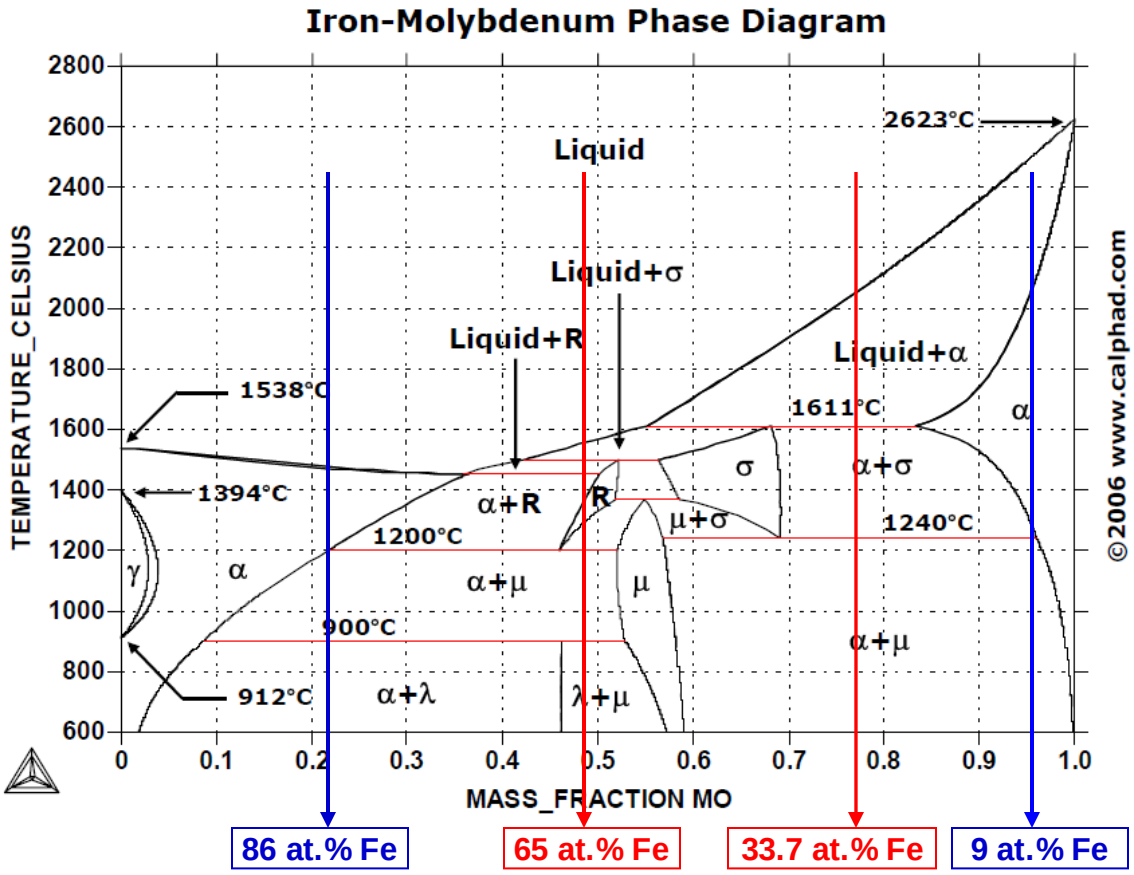

Figure 6.22 Fe - Mo phase diagram in wt.% and the location of the coating/substrate compositions based on EDS experimental data listed in Table 6.11 [128].

A standard X-ray diffraction θ-2θ scan was performed using a D8 system in Bragg-Brentano geometry with LynxEye detector, V6 variable divergence slit, 0.02º / step at 3sec / step. Phase identification was conducted with Eva software.

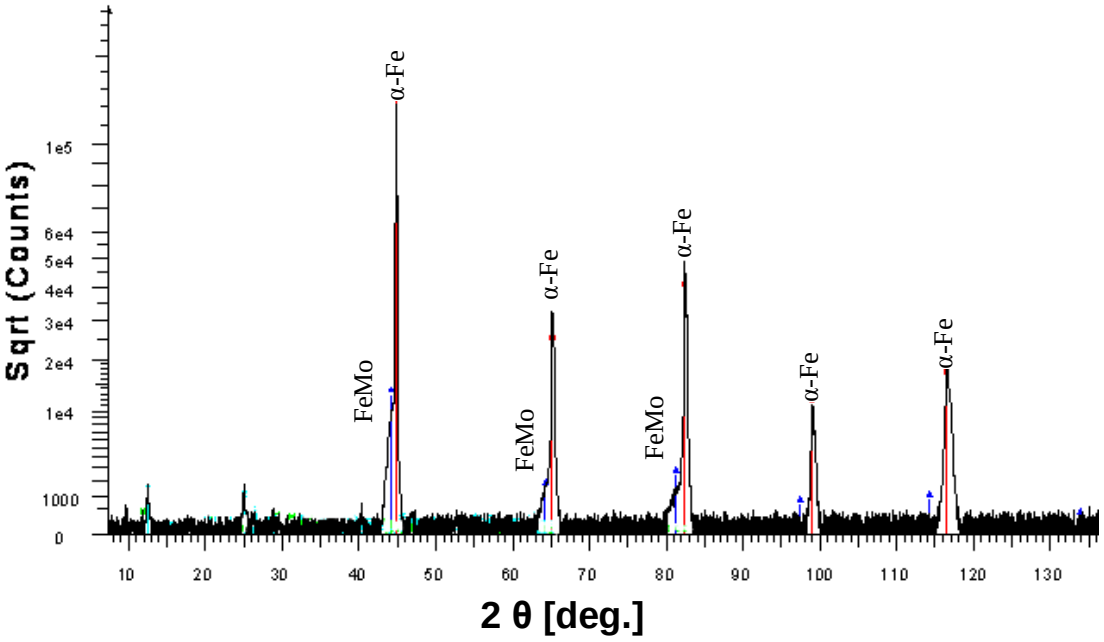

Figure 6.23 X-ray intensity peaks of top view Mo coating.

The XRD results are shown in Figure 6.23. The pattern shows strong diffraction peaks from the Fe substrate but a shoulder at lower diffraction angles from the coating is also present. Taken into account that both Fe and Mo have the same crystal structure (BCC) and the larger size of the Mo atoms compared to that of Fe, the shoulder indicates an alloy Fe-Mo with larger lattice parameter. As seen before, the coating is not pure Mo. The broadening of the peaks can be attributed to the small grain size of the Fe-Mo alloy in the coating. The SEM/EDS elemental analysis coupled with the above XRD results demonstrate that Mo will alloy with Fe substrate and deposit as an alloy.

6.3 Concluding Remarks

The three coatings investigated in the present work cover a wide range of T_M in relation with that of the Fe substrate. The substrate/coating interaction was approached from two angles: topography and interface evolution.

Zn possesses low surface energy and high nucleation rate, therefore, the topography exhibits large nodules composed of fine nano nodules produced by the fast nucleation rate. The large surface area generated by this formation is not of consideration given the low surface energy. At the same time, the fast deposition rates in conjunction with H_2 bubble formation results in relatively high porosity.

The mechanism of Zn coating formation by EPP presents two components that can be related to traditional deposition techniques, and those are galvanizing and electrodeposition. The well defined intermetallics interface was the result of liquid / liquid mixing following the Fe-Zn phase diagram evolution. Initially, high temperature of plasma bubble collapsing will superficially melt the Fe substrate and the incoming Zn atoms will mix with the thin Fe molten layer. Following the first solidification event, the resulting top layer will consist of rich Fe composition. Subsequent melting of the newly formed top layer will mix with new arriving Zn atoms and solidify with a new composition ratio of Fe and Zn that in time will move towards Zn rich phases. This transition occurs in the 100 nm interface layer, Figure 6.12. From that point forward, an "enhanced electrolysis" will drive the Zn coating deposition. The enhancement comes from the high voltage that will create the surplus of Zn in the electrolyte.

Table 6.13 Surface energy for the three coatings and the substrate.

Material	Surface energy [J/m^2]
Fe	2.45
Zn	0.99
Ni	2.42
Mo	2.95

Ni coating is characterized of relatively large nodules (without presence of finer nodules), due to large surface energy to minimize surface area. Deposition rate was considerably lower (10 times lower than Zn) allowing escape of H_2 bubble, leading to lower porosity (higher coating density).

The mechanism of Ni coating formation is somehow similar to that of Zn. Galvanizing and electrolysis are found to be the driving mechanisms present. The Fe-Ni interface layer thickness was ~ 800 nm, Figure 6.17, ~10 times larger compared with that of Fe-Zn. It can be inferred that

due to similar T_M of Fe and Ni, liquid/liquid mixing will occur with comparable molten volumes for the Fe substrate and the coating Ni. The extended interface is the result of a lower gradient of Fe depletion in the interface. Once the coating becomes pure Ni, electrolysis will be the driving mechanism for deposition.

The presence of a full intermetallic layer near the bulk substrate for Zn and Ni coating formation may be the result of the fast cooling rate of the mixing interface.

Aside of crack formation, Mo coating surface was flat resulting from nodule coalescence driven by high surface energy. No major porosity was present since the underlying Fe substrate is still in liquid phase and expected to fill in pores. This may contribute to the alloying process of the Mo nodules.

Mo coating formation is the result of galvanizing and electrolysis taking place simultaneously. Initial Mo atoms will mix with the liquid Fe substrate and form a Fe rich interface. With a lower T_M than the bulk substrate, Figure 6.22, this interface will remain liquid for most of the deposition process time and will migrate upward through the Mo rich deposited layers. Finally, high temperature enhanced diffusion of the Fe rich liquid into the bulk Mo coating will leave behind the observed cracks, Figure 6.3.

Two controlling parameters were found regarding substrate/coating interface evolution. These are difference in melting point between substrate and coating material and phase diagram characteristics. A coating with lower melting point (e.g., Zn) creates a limited interface due to massive built-up (excess) of the coating material on the substrate surface. Depending on the phase diagram, intermetallic formation is expected as observed experimentally in the Zn coatings (ζ and Γ_1).

A coating with comparable T_M with the substrate results in a liquid phase with both elements soluble and depending on the phase diagram characteristics, significant mixing can occur at the interface. In the Fe-Ni system, an 800 nm interface was produced with a Ni-rich and Fe-rich phases present at its end of the interface.

The formation of the Mo coating was found to be dominated by its large T_M compared to the substrate. The continuous presence of a liquid phase of the substrate material has as a result the extension of the interface into the coating. Depending on the phase diagram, intermetallics may form but such formation occurs in the coating side again due to the presence of substrate as a liquid phase.

In summary, the EPP deposited coatings morphology and structure are influenced by two mechanisms:

1. EPP-deposited coatings were found to exhibit a topography that can be attributed to coating material surface energy. Low surface energy coatings were found to deposit with high rates and to create porosity (i.e., Zn). Medium surface energy materials are expected to develop larger nodules (i.e., Ni). High surface energy results in nodule coalescence and flat surfaces (i.e., Mo).
2. The substrate/coating interface and its structure formation can be attributed to the T_M of the substrate and coating material. The substrate/coating interface for a low T_M coating material was found to develop intermetallics following the phase diagram. Coating material with comparable T_M with the substrate was found to present significant mixing at the interface. High T_M coatings would develop an extended interface with substrate material being present in liquid form and impeding uniform coating formation.
3. The coating structure at the top is composed of fine grains and presents similarities with the microstructure of top cleaned layer, and can be attributed to the fast cooling rates and plasma enhanced deposition.

CHAPTER 7

CONCLUSIONS

Besides the major conclusions noted earlier for EPP cleaning and coating, some similarities and differences are highlighted here.

The presence of a fine microstructure at the top of processed surfaces was found to be similar for both cleaning and coating. Very small grain size (nano-grains) were expected to be the result of the presence of fast cooling rates as well as undercooling effects for materials used in the present study, materials with a variation in T_M that cover most of the range.

A difference between these two processes (cleaning and coating) involves the source for the deposited material. In cleaning it is the result of melting and freezing (self deposition) of the substrate, while for coating is the liquid – liquid mixing resulting from the molten substrate and the incoming coating ions from the electrolyte. This difference can account for the observed differences in the surface topography.

EPP treated surfaces develop a unique surface morphology composed of hills and valleys in the EPP cleaning and nodules respectively for the EPP coating, depending on their surface energy.

The coating microstructure and composition may be tailored upon the substrate and coating properties. EPP deposited coatings are a result of two unique and well studied processes, galvanizing and electrolysis, which play key roles in the coating microstructure evolution.

Based on the present findings, coating deposition materials can be tailored depending on the substrate material and considering physical properties (T_M, surface energy, phase diagram, etc.) of both substrate and coating materials.

APPENDIX 1

PDF FILES OF FE-ZN AND FE DIFFRACTIONS

Fe

PDF#06-0696: QM=Star/Calculated; d=Other/Unknown; I=(Unknown)
Iron, syn
Fe
Radiation=CuKa1 Lambda=1.5406 Filter=
Calibration= d-Cutoff= I/Ic(RIR)=
Ref= Level-1 PDF

Cubic, Im-3m(229) Z=2 mp=
Cell=2.866x2.866x2.866<90x90x90> Pearson=
Density(c)=7.874 Density(m)= Mwt= Vol=
Ref= Ibid.

Strong Line: 2.03/X 1.17/3 1.43/2 0.91/1 1.01/1 0.83/1

d(A)	I(f)	I(v)	h	k	l	n^2	2-Theta	Theta	1/(2d)	2pi/d
2.026	100.0	100.0	1	1	0	2	44.673	22.337	0.2467	3.1001
1.433	20.0	28.0	2	0	0	4	65.021	32.511	0.3489	4.3840
1.170	30.0	52.0	2	1	1	6	82.333	41.166	0.4273	5.3693
1.013	10.0	20.0	2	2	0	8	98.945	49.473	0.4934	6.2001
0.906	12.0	27.0	3	1	0	10	116.385	58.192	0.5516	6.9320
0.827	6.0	15.0	2	2	2	12	137.136	68.568	0.6042	7.5930

Γ_1

PDF#32-0478: QM=Star/Calculated; d=Other/Unknown; I=(Unknown)
Iron Zinc
Fe11Zn40
Radiation=CuKa1 Lambda=1.5406 Filter=
Calibration= d-Cutoff= I/Ic(RIR)=
Ref= Level-1 PDF

Cubic, F-43m(216) Z=8 mp=
Cell=17.98x17.98x17.98<90x90x90> Pearson=
Density(c)=7.381 Density(m)= Mwt= Vol=
Ref= Ibid.

Strong Line: 2.12/X 2.18/8 2.08/8 2.34/6 2.40/6 2.20/6 2.06/4 1.97/4

d(A)	I(f)	I(v)	h	k	l	n^2	2-Theta	Theta	1/(2d)	2pi/d
2.998	10.0	7.0	6	0	0	36	29.776	14.888	0.1668	2.0958
2.845	10.0	7.0	6	2	0	40	31.418	15.709	0.1757	2.2085
2.742	10.0	8.0	5	3	3	43	32.630	16.315	0.1823	2.2915
2.598	30.0	24.0	4	4	4	48	34.494	17.247	0.1925	2.4185

2.519	30.0	25.0	5	5	1	51	35.611	17.806	0.1985	2.4943
2.493	10.0	9.0	6	4	0	52	35.995	17.998	0.2006	2.5203
2.404	60.0	53.0	6	4	2	56	37.376	18.688	0.2080	2.6136
2.343	60.0	54.0	7	3	1	59	38.387	19.193	0.2134	2.6817
2.197	60.0	58.0	7	3	3	67	41.049	20.524	0.2276	2.8599
2.183	80.0	78.0	8	2	0	68	41.324	20.662	0.2290	2.8782
2.120	100.0	100.0	6	6	0	72	42.611	21.305	0.2358	2.9638
2.078	80.0	82.0	7	5	1	75	43.516	21.758	0.2406	3.0237
2.064	40.0	41.0	6	6	2	76	43.826	21.913	0.2422	3.0442
1.974	40.0	43.0	9	1	1	83	45.935	22.968	0.2533	3.1830
1.962	30.0	32.0	8	4	2	84	46.233	23.116	0.2548	3.2024
1.918	30.0	33.0	6	6	4	88	47.357	23.679	0.2607	3.2759
1.887	30.0	34.0	9	3	1	91	48.184	24.092	0.2650	3.3297
1.836	30.0	35.0	8	4	4	96	49.611	24.806	0.2723	3.4222
1.808	10.0	12.0	9	3	3	99	50.433	25.216	0.2765	3.4752
1.764	20.0	24.0	10	2	0	104	51.783	25.891	0.2834	3.5619
1.731	20.0	24.0	10	2	2	108	52.846	26.423	0.2889	3.6298
1.671	5.0	6.0	10	4	0	116	54.899	27.450	0.2992	3.7601
1.644	5.0	6.0	10	4	2	120	55.879	27.940	0.3041	3.8219
1.624	5.0	7.0	11	1	1	123	56.629	28.314	0.3079	3.8690
1.590	5.0	7.0	8	8	0	128	57.953	28.977	0.3145	3.9517
1.572	5.0	7.0	11	3	1	131	58.681	29.341	0.3181	3.9969
1.527	5.0	7.0	9	7	3	139	60.588	30.294	0.3274	4.1147
1.500	5.0	7.0	12	0	0	144	61.797	30.899	0.3333	4.1888
1.479	5.0	7.0	12	2	0	148	62.773	31.387	0.3381	4.2483
1.460	5.0	7.0	12	2	2	152	63.685	31.843	0.3425	4.3036
1.377	10.0	15.0	11	7	1	171	68.027	34.014	0.3631	4.5630
1.356	10.0	16.0	12	4	4	176	69.229	34.615	0.3687	4.6336
1.344	10.0	16.0	13	3	1	179	69.937	34.968	0.3720	4.6750
1.326	10.0	16.0	12	6	2	184	71.028	35.514	0.3771	4.7385
1.315	20.0	32.0	13	3	3	187	71.714	35.857	0.3802	4.7781
1.298	20.0	33.0	8	8	8	192	72.802	36.401	0.3852	4.8407
1.285	10.0	16.0	14	0	0	196	73.660	36.830	0.3891	4.8896
1.272	40.0	67.0	10	10	0	200	74.539	37.270	0.3931	4.9396
1.262	30.0	50.0	13	5	3	203	75.232	37.616	0.3962	4.9788
1.238	5.0	9.0	11	9	3	211	76.954	38.477	0.4039	5.0753
1.224	40.0	69.0	14	4	2	216	77.999	39.000	0.4085	5.1333
1.215	10.0	17.0	13	5	5	219	78.688	39.344	0.4115	5.1713
1.191	30.0	53.0	14	4	4	228	80.594	40.297	0.4198	5.2756
1.153	30.0	55.0	15	3	3	243	83.836	41.918	0.4337	5.4494
1.141	5.0	9.0	12	10	2	248	84.923	42.461	0.4382	5.5067
1.106	10.0	19.0	16	2	2	264	88.287	44.143	0.4521	5.6810
1.091	20.0	39.0	16	4	0	272	89.826	44.913	0.4583	5.7591
1.084	20.0	39.0	15	5	5	275	90.491	45.246	0.4610	5.7926

ζ

PDF#65-1238: QM=Star/Calculated; d=Other/Unknown; I=(Unknown)
Iron Zinc
FeZn13
Radiation=CuKa1 Lambda=1.5406 Filter=
Calibration= d-Cutoff= I/Ic(RIR)=2.4
Ref= Level-1 PDF

Monoclinic, C2/m(12) Z=2 mp=
Cell=13.424x7.608x5.061<90x127.3x90> Pearson=
Density(c)=7.316 Density(m)= Mwt= Vol=
Ref= Ibid.

Strong Line: 2.17/X 2.12/8 2.15/6 2.06/5 2.11/4 2.08/4 1.26/4 2.19/4

d(A)	I(f)	I(v)	h	k	l	n^2	2-Theta	Theta	1/(2d)	2pi/d
6.196	7.2	2.5	1	1	0		14.282	7.141	0.0807	1.0140
5.339	0.4	0.2	2	0	0		16.590	8.295	0.0936	1.1768
4.975	0.1	0.0	-2	0	1		17.812	8.906	0.1005	1.2628
4.097	7.4	3.9	-1	1	1		21.669	10.835	0.1220	1.5333
4.025	1.5	0.8	0	0	1		22.061	11.031	0.1242	1.5607
3.804	0.1	0.1	0	2	0		23.365	11.683	0.1314	1.6517
3.692	7.7	4.5	-3	1	1		24.079	12.039	0.1354	1.7014
3.347	0.1	0.1	-4	0	1		26.608	13.304	0.1494	1.8770
3.224	0.1	0.1	3	1	0		27.645	13.823	0.1551	1.9488
3.098	0.1	0.1	2	2	0		28.793	14.396	0.1614	2.0281
3.022	2.4	1.7	-2	2	1		29.534	14.767	0.1655	2.0792
2.936	0.2	0.1	1	1	1		30.410	15.205	0.1702	2.1394
2.765	6.4	5.0	0	2	1		32.352	16.176	0.1808	2.2724
2.669	1.4	1.1	4	0	0		33.541	16.770	0.1873	2.3536
2.555	7.6	6.5	2	0	1		35.090	17.545	0.1957	2.4590
2.521	7.3	6.3	-5	1	1		35.572	17.786	0.1983	2.4916
2.513	24.0	20.8	-4	2	1		35.699	17.850	0.1990	2.5003
2.487	5.6	4.9	-4	0	2		36.073	18.037	0.2010	2.5256
2.467	3.2	2.8	1	3	0		36.382	18.191	0.2026	2.5465
2.431	13.0	11.6	-2	0	2		36.934	18.467	0.2056	2.5838
2.398	1.0	0.9	-3	1	2		37.467	18.734	0.2085	2.6198
2.248	9.9	9.6	-1	3	1		40.065	20.032	0.2224	2.7942
2.228	6.3	6.1	-5	1	2		40.446	20.223	0.2244	2.8197
2.191	35.9	35.6	-6	0	1		41.160	20.580	0.2282	2.8673
2.185	28.1	28.0	4	2	0		41.281	20.640	0.2288	2.8753
2.174	100.0	100.0	-3	3	1		41.498	20.749	0.2300	2.8899
2.149	61.4	62.1	-1	1	2		42.001	21.000	0.2326	2.9233
2.121	81.8	83.8	2	2	1		42.588	21.294	0.2357	2.9622
2.111	42.4	43.7	-6	0	2		42.781	21.391	0.2367	2.9751
2.082	41.6	43.4	-4	2	2		43.426	21.713	0.2401	3.0178
2.065	29.7	31.3	3	3	0		43.794	21.897	0.2421	3.0421
2.056	45.5	48.1	5	1	0		44.001	22.000	0.2432	3.0557
2.048	26.3	27.9	-2	2	2		44.166	22.083	0.2440	3.0666
2.030	2.0	2.1	3	1	1		44.581	22.290	0.2462	3.0940
2.012	2.9	3.1	0	0	2		44.997	22.499	0.2484	3.1214
1.983	12.1	13.3	1	3	1		45.701	22.850	0.2521	3.1676
1.902	14.9	17.0	0	4	0		47.780	23.890	0.2629	3.3035
1.898	11.7	13.4	-6	2	1		47.866	23.933	0.2633	3.3090
1.846	0.7	0.8	-6	2	2		49.312	24.656	0.2708	3.4028
1.839	1.0	1.2	-5	3	1		49.505	24.753	0.2718	3.4154
1.828	0.1	0.1	-7	1	2		49.829	24.915	0.2734	3.4363
1.791	4.4	5.3	2	4	0		50.924	25.462	0.2791	3.5068
1.782	8.2	10.0	4	0	1		51.211	25.605	0.2805	3.5252
1.779	4.8	5.9	0	2	2		51.308	25.654	0.2810	3.5315
1.742	0.5	0.6	1	1	2		52.460	26.230	0.2869	3.6052
1.719	3.9	4.9	0	4	1		53.219	26.610	0.2907	3.6536

1.716	1.9	2.4	-5	3	2	53.345	26.672	0.2914	3.6616
1.679	0.1	0.1	-1	3	2	54.611	27.305	0.2978	3.7419
1.673	2.2	2.9	-8	0	2	54.830	27.415	0.2989	3.7558
1.658	1.0	1.3	-6	0	3	55.347	27.674	0.3015	3.7884
1.653	0.7	0.9	-4	4	1	55.523	27.762	0.3024	3.7995
1.646	0.7	0.9	-5	1	3	55.791	27.896	0.3037	3.8164
1.633	0.1	0.1	5	3	0	56.267	28.134	0.3061	3.8463
1.620	0.1	0.1	3	3	1	56.753	28.377	0.3085	3.8767
1.612	0.8	1.1	4	2	1	57.088	28.544	0.3102	3.8977
1.591	0.2	0.3	2	0	2	57.880	28.940	0.3141	3.9471
1.585	1.4	1.9	-8	0	1	58.131	29.065	0.3153	3.9627
1.561	7.5	10.4	-7	1	3	59.125	29.562	0.3203	4.0244
1.549	0.2	0.3	4	4	0	59.638	29.819	0.3228	4.0562
1.540	2.3	3.2	-2	0	3	59.989	29.995	0.3245	4.0778
1.531	25.2	35.8	-8	2	2	60.396	30.198	0.3265	4.1029
1.525	6.4	9.1	2	4	1	60.645	30.322	0.3277	4.1182
1.520	1.2	1.7	-6	2	3	60.883	30.442	0.3289	4.1328
1.511	3.0	4.3	-7	3	2	61.299	30.650	0.3309	4.1583
1.507	5.2	7.5	-8	0	3	61.449	30.725	0.3316	4.1675
1.498	0.9	1.3	-2	4	2	61.881	30.940	0.3337	4.1939

APPENDIX 2

PDF FILES OF FE-NI AND NI DIFFRACTIONS

Ni

PDF#70-1849: QM=Star/Calculated; d=Other/Unknown; I=(Unknown)
Nickel
Ni
Radiation=CuKa1 Lambda=1.5406 Filter=
Calibration= d-Cutoff= I/Ic(RIR)=7.44
Ref= Level-1 PDF

Cubic, Fm-3m(225) Z=4 mp=
Cell=3.525x3.525x3.525<90x90x90> Pearson=
Density(c)=8.901 Density(m)= Mwt= Vol=
Ref= Ibid.

Strong Line: 2.04/X 1.76/4 1.25/2

d(A)	I(f)	I(v)	h	k	l	n^2	2-Theta	Theta	1/(2d)	2pi/d
2.035	100.0	100.0	1	1	1	3	44.480	22.240	0.2457	3.0873
1.762	41.9	48.4	2	0	0	4	51.830	25.915	0.2837	3.5649
1.246	16.1	26.3	2	2	0	8	76.350	38.175	0.4012	5.0416

$FeNi_3$

PDF#65-3244: QM=Star/Calculated; d=Other/Unknown; I=(Unknown)
Iron Nickel
FeNi3
Radiation=CuKa1 Lambda=1.5406 Filter=
Calibration= d-Cutoff= I/Ic(RIR)=7.99
Ref= Level-1 PDF

Cubic, Pm-3m(221) Z=1 mp=
Cell=3.552x3.552x3.552<90x90x90> Pearson=
Density(c)=8.592 Density(m)= Mwt= Vol=
Ref= Ibid.

Strong Line: 2.05/X 1.78/4 1.26/2 1.07/2 0.81/1

d(A)	I(f)	I(v)	h	k	l	n^2	2-Theta	Theta	1/(2d)	2pi/d
3.552	0.4	0.2	1	0	0	1	25.047	12.523	0.1408	1.7688
2.511	0.4	0.3	1	1	0	2	35.716	17.858	0.1991	2.5014
2.050	100.0	100.0	1	1	1	3	44.120	22.060	0.2438	3.0636
1.776	43.0	49.7	2	0	0	4	51.403	25.701	0.2815	3.5375
1.588	0.2	0.3	2	1	0	5	58.008	29.004	0.3147	3.9551
1.450	0.2	0.3	2	1	1	6	64.166	32.083	0.3448	4.3326
1.255	18.6	30.4	2	2	0	8	75.659	37.830	0.3981	5.0028

1.184 0.1 0.2 2 2 1 9 81.162 40.581 0.4223 5.3063
1.123 0.1 0.2 3 1 0 10 86.582 43.291 0.4451 5.5933
1.071 17.8 34.1 3 1 1 11 91.973 45.986 0.4668 5.8663
1.025 4.9 9.8 2 2 2 12 97.381 48.691 0.4876 6.1272
0.985 0.1 0.2 3 2 0 13 102.856 51.428 0.5075 6.3774
0.949 0.1 0.2 3 2 1 14 108.454 54.227 0.5267 6.6181
0.888 2.3 5.3 4 0 0 16 120.306 60.153 0.5630 7.0751
0.861 0.1 0.2 4 1 0 17 126.774 63.387 0.5803 7.2928
0.837 0.1 0.2 4 1 1 18 133.844 66.922 0.5972 7.5042
0.815 7.9 19.9 3 3 1 19 141.882 70.941 0.6135 7.7099

$Fe_{0.64}Ni_{0.36}$

PDF#47-1405: QM=Star/Calculated; d=Other/Unknown; I=(Unknown)
Iron Nickel
Fe0.64Ni0.36
Radiation=CuKa1 Lambda=1.5406 Filter=
Calibration= d-Cutoff= I/Ic(RIR)=
Ref= Level-1 PDF

Cubic, Fm3m(225) Z=4 mp=
Cell=3.592x3.592x3.592<90x90x90> Pearson=
Density(c)=8.15 Density(m)= Mwt= Vol=
Ref= Ibid.

Strong Line: 2.07/X 1.80/5 1.27/3 1.08/2 1.04/1

d(A) I(f) I(v) h k l n^2 2-Theta Theta 1/(2d) 2pi/d
2.074 100.0 100.0 1 1 1 3 43.604 21.802 0.2411 3.0295
1.796 49.0 57.0 2 0 0 4 50.794 25.397 0.2784 3.4984
1.270 25.0 41.0 2 2 0 8 74.677 37.338 0.3937 4.9474
1.083 20.0 38.0 3 1 1 11 90.630 45.315 0.4615 5.7995
1.037 7.0 14.0 2 2 2 12 95.904 47.952 0.4820 6.0573

REFERENCES

1. L. Ponsonnet, V. Comte, A. Othmane, C. Lagneau, M. Charbonnier, M. Lissac, and N. Jaffrezic, Effect of surface topography and chemistry on adhesion, orientation and growth of fibroblast on nickel-titanium substrates, Mater. Sci. Engin. C21, 157 (2002).
2. B. D. Boyan, T. W. Hummert, D. D. Dean, and Z. Schwartz, Role of material surfaces in regulating bone and cartilage cell response, Biomat. 17, 137 (1996).
3. N. Verdonschot, E. Tanck, and R. Huiskes, Effects of prosthesis surface roughness on the failure process of cemented hip implants after stem-cement debonding, J. Biomed. Mater. Res. 42, 554 (1998).
4. H. Zhao, J. Van Humbeeck, and I. De Scheerder, Surface conditioning of nickel-titanium alloy stents for improving biocompatibility, Surf. Engin. 17, 451 (2001).
5. J. Y. Martin, Z. Schwartz, et al., Effect of titanium surface roughness on chondrocyte proliferation, matrix production, and differentiation depends on the state of cell maturation, J. Biomed. Mater. Res. 29, 389 (1995).
6. Shihai Cui, Jianmin Han, Yongping Du, Weijing Li, Corrosion resistance and wear resistance of plasma electrolytic oxidation coatings on metal matrix composites, Surf. Coat. Tech., 201, 5306-5309 (2007).
7. M. Bigerelle, K. Anselme, B. Noël, I. Ruderman, P. Hardouin, A. Iost, Improvement in the morphology of Ti-based surfaces: a new process to increase in vitro human osteoblast response, Biomaterials, 23, 1563-1577 (2002).
8. O. Cisse, O. Savadogo, M. Wu, and L. Yahia, Effect of surface treatment of NiTi alloy on its corrosion behavior in Hanks' solution, J. Biomed. Mater. Res. 61, 339 (2002).
9. R.C. Barik, J.A. Wharton, R.J.K. Wood, K.R. Stokes, R.L. Jones, Corrosion, erosion and erosion–corrosion performance of plasma electrolytic oxidation (PEO) deposited Al_2O_3 coatings, Surf. Coat. Tech, 199, 158-167 (2005).

10. H.P Bonzel, The role of surface science experiments in understanding heterogeneous catalysis, Surface Science, 68, 236-258 (1977).

11. N. J. Hallab, K. J. Bundy, K. O'Connor, R. Clark, and R. L. Moses, Cell adhesion to biomaterials: Correlations between surface charge, surface roughness, adsorbed protein, and cell morphology, J. Long-Term Eff. Med. Implants 5, 209 (1995).

12. I. De Scheerder, J. Sohier, E. Verbeken, L. Froyen, and J. Van Humbeeck, Biocompatibility of coronary stent materials: Effect of electrochemical polishing, Materialwissenschaft Und Werkstofftechnik 32, 142 (2001).

13. M. Ye, J. L. Delplancke, G. Berton, L. Segers, R. Winand, Characterization and adhesion strength study of Zn coatings electrodeposited on steel substrates, Surf. and Coat. Tech., 105, Issues 1-2, 184-188 (1998).

14. A. F. Harris, A. Beevers, The effect of grit-blasting on surface properties for adhesion, Int. J. of Adhesion & Adhesives 19, 445-452, (1999).

15. Frank Hollstein, Petr Louda, Bio-compatible low reflective coatings for surgical tools using reactive d.c.-magnetron sputtering and arc evaporation - a comparison regarding steam sterilization resistance and nickel diffusion, Surf. Coat. Tech. 120-121, 672-681 (1999).

16. Z. W. Kowalski, Ion sputter induced surface morphology - biomedical implications, Vacuum, 63, 603-608 (2001).

17. Zbigniew W. Kowalski, Janusz Wilk, Janusz Martan, Surface morphology of steel and titanium induced by ion beam bombardment - Comprehensive Analysis, Vacuum, 83, S208-S213 (2009).

18. D. Landolt, Fundamental aspects of electropolishing, Electrochimica Acta, 32, 1-11 (1987).

19. S. Mohan, D. Kanagaraj, R. Sindhuja, S. Vijayalakshimi, and N. G. Renganathan, Electropolishing of stainless steel – a review, Trans. Inst. Metal Finish. 79, 140 (2001).

20. D. Aslanidis, G. Roebben, J. Bruninx, and W. Van Moorleghem, Electropolishing for medical devices: Relatively new … fascinatingly diverse, Mater. Sci. Forum 394, 911 (2001).
21. Jie Gong, G. Zangari, Electrodeposition of sacrificial tin-manganese alloy coatings, Mat. Sci. Eng. A344, 268-278 (2003).
22. Wojciech Simka, Dagmara Puszczyk, Ginter Nawrat, Electrodeposition of metals from non-aqueous solutions, Electrochimica Acta, Volume 54, 5307-5319 (2009).
23. Farid Hanna, Nabil Nassif, Factors affecting the quality of hot-dip-galvanized steel sheets, Surf. Tech., 21, Issue 1, 27-37 (1984)
24. N.P. Sluginov J. Russ. Phys. Chem. Soc. 12 1-2 (1980), p. 193.
25. A.L. Yerokhin, X. Nie, A. Leyland, A. Mathews, S.J. Downey – Plasma electrolysis for surface engineering, Surf. Coat. Tech. 122, 73-93 (1999).
26. J. A. Curran, Thermal and mechanical Properties of Plasma Electrolytic Oxide Coatings, PhD Dissertation, University of Cambridge, (2005).
27. E.I. Meletis, X. Nie, F.L. Wang, J.C. Jiang, Electrolytic plasma processing for cleaning and metal coating of steel surfaces, Surf. Coat. Tech. 150, 246-256 (2002).
28. R. Suryanarayanan – Plasma spraying: theory and applications, (1993).
29. S. Kuroda, J. Kawakita, M. Watanabe and H. Katanoda - Warm spraying - a novel coating process based on high-velocity impact of solid particles, Sci. Technol. Adv. Mater. 9 033002 (2008).
30. F. Leroux - Fluorocarbon nano-coating of polyester fabrics by atmospheric air plasma with aerosol. Appl. Surf. Sci. 254: 3902-3908, (2008).
31. J. Dufour, Jim - An Introduction to Metallurgy, Cameron, 5th ed., (2006).
32. J.B. Mohler, - Electroplating and Related Processes. Chemical Publishing Co.,(1969).
33. M. Ohring – Materials Science of Thin Films, Academic Press, (2002).
34. Dobkin and Zuraw - Principles of Chemical Vapor Deposition. Kluwer, (2003).

35. M.L. Hitchman, K.F. Jensen – Chemical Vapor Deposition, Principles and Applications, Academic Press, London, (1993).
36. M.J. Hampden-Smith, T.T. Kodas – The chemistry of metal CVD, VCH, Weinheim, (1994).
37. H.O. Pierson – Handbook of Chemical Vapor Deposition, Principles, Technologies and Applications, Noyes, (1992).
38. J.E. Mahan, - Physical Vapor Deposition of Thin Films. New York: John Wiley & Sons, (2000).
39. R.F. Bunshah - Handbook of Deposition Technologies for Films and Coatings: Science, Technology and Applications, Noyes Publications, (1994).
40. P. Gupta, G. Tenhundfeld, E.O. Daigle, P.J. Schilling, Synthesis and characterization of hard metal coatings by electro-plasma technology, Surf. Coat. Tech 200, 1587-1594 (2005).
41. P. Gupta and G. Tenhundfeld, Surface And Mechanical Properties Of Steel Cleaned By Electro-Plasma Technology, Plating and Surface Finishing, 92, 48-52 (2005).
42. P. Gupta, G. Tenhundfeld, E.O. Daigle, D. Ryabkov, and B. Calliham, Next Generation Cleaning & Surface Modification Technology, Wire & Cable Technology International, XXXI, 52 (2003).
43. P. Vanýsek, Petr (2007). - “Electrochemical Series”, in Handbook of Chemistry and Physics: 88th Edition, (2007).
44. www.saskschools.ca
45. http://farside.ph.utexas.edu/teaching/plasma/lectures/lectures.html
46. M.P. Brenner and D. Lohse – Dynamic equilibrium mechanism for surface nanobubble stabilization – Phys Rev Let., 101, 214505, (2008).
47. P.S. Epstein, M.S. Plesset – J. Chem. Phys. 18, 1505, (1950).
48. A. Luzar, D. Bratko – J. Phys. Chem. B 109, 22545, (2005).
49. X.H. Zhang, A. Khan, W.A. Ducker – Phys. Rev. Lett. 98, 136101, (2007).

50. A. Poynor et al. – Phys. Rev. Lett. 97, 266101, (2006).

51. L. Zhang et al. – Langmuir 22, 8109, (2006).

52. A.L. Yerokhin – Electrophysical & electrochemical treatment of materials, TulGU, Tula, 30, in Russian, (1996).

53. A. Hickling, M.D. Ingram, Glow-discharge electrolysis, J. of Elec. Chem., 8, Issue 1, 65-8, (1964).

54. S. K. Sengupta, The effect of electrolyte constituents on the onset and location of glow-discharge electrolysis, J. of Elec. Chem., 127, Issues 1-3, 263-265, (1981).

55. S. K. Sengupta, O. P. Singh, Contact glow discharge electrolysis: a study of its chemical yields in aqueous inert-type electrolytes, J. of Elec. Chem., Volume 369, Issues 1-2, 113-120, (1994).

56. B.S.R. Sastry, Characteristics of glow-discharge electrolysis in aqueous, non-aqueous and molten systems, J. of Elec. Chem., 10, Issue 3, 248-250, (1965).

57. J. Garbarz-Olivier, C. Guilpin, The origin of the electrode effect in various electrolytes, Journal of El. Chem., 91, Issue 1, 79-91, (1978).

58. A.J. Calandra, J.R. Zavatti, J. Thonstad, The effect of gas bubbles on the onset of the anode effect during fluoride ion discharge on carbon, Electrochimica Acta, 37, Issue 4, 711-717, (1992).

59. Yu. N. Tyurin and A. D. Pogrebnjak, Specific features of electrolytic-plasma quenching, Technical Physics, Volume 47, Number 11, 1463-1464, (2002).

60. A.L. Yerokhin, X. Nie, A. Leyland, A. Mathews, S.J. Downey – Plasma electrolysis for surface engineering, Surf. Coat. Tech. 122, 73-93 (1999).

61. J. A. Curran – Thermal and mechanical properties of plasma electrolytic oxide coatings, doctoral dissertation, Cambridge, (2005)

62. X. Nie, C. Tsotsos, A. Wilson, A. L. Yerokhin, A. Leyland, A. Matthews, Characteristics of a plasma electrolytic nitrocarburising treatment for stainless steels, Surf. Coat. Tech., 139, Issues 2-3, 135-142, (2001).

63. L. Yerokhin, A. Leyland, C. Tsotsos, A. D. Wilson, X. Nie, A. Matthews, Duplex surface treatments combining plasma electrolytic nitrocarburising and plasma-immersion ion-assisted deposition, Surf. Coat. Tech., 142-144, 1129-1136, (2001).

64. Xin-Mei Li, Yong Han, Mechanical properties of Ti(C0.7N0.3) film produced by plasma electrolytic carbonitriding of Ti6Al4V alloy, Appl. Surf. Sci., 254, Issue 20, 6350-6357, (2008).

65. Xin-Mei Li, Yong Han, Yin-Suo Li, Synthesis of nanocristalline Ti (CxN1-x) thick films on titanium by plasma electrolytic carbonitriding, Surf. Coat. Tech., 201, Issues 9-11, 5326-5329, (2007).

66. P.J. Schilling, P.D. Herrington, E.O. Daigle and E.I. Meletis, Surface characteristics of structural steel processed using electro-plasma techniques, J. Mater. Eng. Perform., 11, 26-31, (2002).

67. A. Yerokhin, A. Pilkington, A. Matthews, Pulse current plasma assisted electrolytic cleaning of AISI 4340 steel, J. of Mat. Proc. Tech., 210, Issue 1, 54-63, (2010).

68. M. Aliofkhazraei, A. Sabour Roohaghdam, A novel method for preparing aluminum diffusion coating by nanocrystalline plasma electrolysis, Electrochemistry Communications 9, 2686-2691 (2007).

69. Prabhu Ganesn, Swaminatha P. Kumaraguru, Branko N. Popov, Development of Zn-Ni-Cd coatings by pulse electrodeposition process - Surf. Coat. Tech. 201, 3658-3669 (2006).

70. P. Gupta, G. Tenhundfeld, E.O. Daigle, D. Ryabkov, Electrolytic plasma technology: Science and engineering - An overview, Surf. Coat. Tech. 201, 8746-8760 (2007).

71. S. K. Sengupta, A. K. Sfivastava, R. Singh, Contact glow discharge electrolysis: a study on its origin in the fight of the theory of hydrodynamic instabilities in local solvent vaporization by Joule heating during electrolysis, J. of El. Chem., 427, 23-27, (1997).

72. A. Hickling, Modern Aspects of Electrochemistry, vol. 6, Butterworths, London, 329, (1971).

73. Y.N. Tyurin and A.D. Pogrebnjak, Electric heating using a liquid electrode, Surf. Coat. Technol. 142–144, 293-299, (2001).

74. H. H. Kellogg, Anode Effect in Aqueous Electrolysis, J. Electrochem. Soc., Volume 97, Issue 4, 133-142, (1950).

75. B. Mazza, P. Pedeferri and G. Re, Hydrodynamic instabilities in electrolytic gas evolution, Electrochim. Acta 23, 87, (1978).

76. V.I. Belevantsev et al., Micro-plasma electrochemical processes, Prot. Met., 34, Issue 5, 416-430, (1998).

77. A.L. Yerokhin et al., Discharge characterization in plasma electrolytic oxidation of aluminium, J. Phys., D, Appl. Phys., 2110-2120, (2003).

78. Y.M. Chen, Cavitation Erosion, ASM Handbook vol. 11, Metals Park, Ohio, (2003).

79. S.D. Brown, K.J. Kuna, T.B. Van, Mechanism of anodic spark deposition, J. Am. Ceram. Soc. 54 (8), 384, (1971).

80. D.Yu. Kharitonov, E.I. Gutsevich, G.I. Novikov, A.A. Fridman, On Mechanism of Pulsed Electrolytic Spark Oxidation in Saturated Sulfuric Acid, TsNIIAtomInform, Moscow,(1988).

81. C.S. Dunleavy, I.O. Golosnoy, J.A. Curran, T.W. Clyne, Characterisation of discharge events during plasma electrolytic oxidation, Surf. Coat. Tech., 203, Issue 22, 3410-3419, (2009).

82. M. D. Klapkiv, Simulation of synthesis of oxide-ceramic coatings in discharge channels of a metal-electrolyte system, Mat. Sc., 35, no.2, 111-114, (1999).

83. Caber, P.J., Interferometric profiler for rough surfaces. Appl. Optics, 32(19), 3438-3441., (1993).

84. http://www.veeco.com

85. L.A. Giannuzzi and F.A. Stevens. Introduction to Focused Ion Beams: Instrumentation, Theory, Techniques and Practice. Springer Press, (2004).

86. J. Orloff, M. Utlaut and L. Swanson, High Resolution Focused Ion Beams: FIB and Its Applications. Springer Press,(2003).

87. Langford, J.I. and A.J.C. Wilson, Scherrer after sixty years: A survey and some new results in the determination of crystallite size. J. Appl. Cryst., 11, 102, (1978).

88. S. Zhang, H. Xie, X. Zeng, P. Hing, Residual stress characterization of diamond-like carbon coatings by an X-ray diffraction method, Surf. Coat. Tech., 122, Issues 2-3, 219-224, (1999).

89. D. Rafaja, V. Valvoda, R. Kuzel, A.J. Perry, J.R. Treglio, XRD characterization of ion-implanted TiN coatings, Surf. and Coat. Tech., 86-87, Part 1, 302, (1996).

90. Veeco Instruments - Wyko NT9100 Surface Profiler – Setup and Operation Guide, (2006)

91. Veeco Instruments - Wyko Surface Profiler – Technical Reference Manual, (2006)

92. E. E. Underwood and Kingshuk Banerji, Fractal analysis of Fracture Surfaces

93. J.R. Pickens and J. Gurland, Metallographic Characterization of Fracture Surface Profiles on Sectioning Planes, Proceedings of the 4th International Congress for Stereology, NBS 431, 269, (1976).

94. K. Banerji, - Quantitative Analisys of Fractire Surfaces using computer Aided Fractography, Ph.D. thesis, Georgia Institute of technology, June 1986

95. Mike Zecchino - Characterizing surface quality: why average roughness is not enough,

96. Mike Zecchino, Donald K. Cohen, Characterizing wear with 3D optical profiling, (2005)

97. L. Vitos, A.V. Ruban, H.L. Skriver, J. Kollar, The surface energy of metals, Surface Science 411,186, (1998).

98. M.J. Assael and al., Reference Data for the Density and Viscosity of Liquid Aluminum and Liquid Iron, J. Phys. Chem. Ref. Data, Vol. 35, No.1, (2006)

99. Q.S. Mei, K. Lu, Melting and superheating of crystalline solids: from bulk to nanocrystals - Progress in Materials Science 52, 1175-1262, (2007)

100. B.D. Cullity and S.R. Stock, Elements of x-ray diffraction, Prentice Hall, Upper Saddle River, NJ 07458, 399, (2001).

101. D. Rafaja, V. Valvoda, R. Kuzel, A.J. Perry, J.R. Treglio, Surf. Coat. Technol. 86, 302, (1999).

102. L.E. Murr, K.P. Staudhammer, M.A. Meyers, Metallurgical and Materials Applications of Shock-Wave and High-Strain-Rate Phenomena, Elsevier Science, 543, (1995).

103. Eckert et al., J. Mater. Res. 7, 1751, (1992).

104. H. Yoshioka, Y. Tada, K. Kunimine, T. Furuichi, Y. Hayashi - Heat and solidification processes of alloy melt with undercooling: I. Experimental results, Acta Materialia 54, 757, (2006).

105. H. Assadi, A.L. Greer – The interfacial undercooling in solidification, J. of Crystal Growth 172, 249, (1997).

106. W.B. Guan, Y-l. Gao, Q.J. Zhai, K.D. Xu – Undercooling of droplet solidification for molten pure aluminum, Mat. Lett. 59 p. 1701-1704, (2005).

107. H. Yoshioka, Y. Tada, K. Kunimine, T. Furuichi, Y. Hayashi – Heat and solidification processes of alloy melt with undercooling: II. Solidification model, Acta Materialia 54, 756, (2006).

108. J.B. Bajat, V.B. Miskovic-Stankovic et al – Electrochemical deposition and characterization of Zn-Fe alloys, J. Serb. Chem. Soc. 69 (10), 807, (2004).

109. S. Wienstroer, M. Fransen et al. – Zin-Iron phase transformation studies on galvanized steel coatings by X-ray diffraction – Advances in X-ray Analysis, volume 46, (2003).

110. G. Blanc, C. Gabrielli, M. Ksouri, R. Wiart – Experimental study of the relationships between the electrochemical noise and the structure of the electrodeposits of metals, Elchem. Acta, Volume 23, Issue 4, 337, (1978)

111. Y.H. Cheng, B.K. Tay , S.P. Lau , X. Shi, H. Kupfer, F. Richter, J. Vac. Sci. Technol. A, 21(5), 1605, (2003).

112. P. Gupta, G. Tenhundfeld, E.O. Daigle, R. Calliham and D. Ryabkov, Patent, Wire Cable Technol. Int. 31, 52, (2003).

113. P. Gupta, G. Tenhundfeld and E.O. Daigle, Patent, Wire J. Int. 38, 50, (2005).

114. J. Black, G. Hastings, Handbook of Biomaterial Properties, Chapman & Hall, London, 1998

115. R. Boyer, G. Welsch, E.W. Collings, Material Properties Handbook: Titanium Alloys, 1994

116. Yu. Lakhtin, Engineering Physical Metallurgy and Heat-Treatment, 1977.

117. T. Uda, T. H. Okabe, Y. Waseda, Y. Awakura, Electroplating of titanium on iron by galvanic contact deposition in NaCl-$TiCl_2$ molten salt, Sci. Tech. Adv. Mater. 7, 490, (2006).

118. E.W. Brooman, Corrosion performance of environmentally acceptable alternatives to cadmium and chromium coatings: Chromium—Part II, Metal Finishing, 98, Issue 8, 39, (2000).

119. G.E. Shahin, Alloys are promising as chromium or cadmium substitutes, Plating and Surface Finishing, 85(8), 8, (1998).

120. S. Usmani, S. Sampath, Time-dependent friction response of plasma-sprayed molybdenum, Wear 225– 229, 1131, (1999).

121. B. Uyulgan, H. Cetinel, I. Ozdemir, C. Tekmen, S.C. Okumus, E. Celik, Friction and wear properties of Mo coatings on cast-iron substrates, Surf. Coat. Technol. 174 – 175, 1082, (2003).

122. M.H. Hong and H. Saka – Transmission electron microscopy of the iron-zinc δ_1 intermetallic phase, Scripta Materialia, Vol. 36, No. 12, 1423, 1997).

123. Jae-Hwa Hong, Sei-Jin Oh, Soon Ju Kwon – Mőssbauer analysis of the iron-zinc intermetallic phases, Intermetallics11, 207, (2003).

124. B.P. Burton and P. Perrot – "Fe-Zn (Iron-Zinc)" in Phase Diagrams od binary iron alloys, ASM International, Materials Park, OH, 459, (1993).

125. H. L. Reynolds, R. Hilty – Investigations of Zinc (Zn) whiskers using FIB technology – IPC/JEDEC Lead Free Conference, Dec. 3, (2004).

126. R.W.K. Honeycombe – The plastic deformation of metals, 2nd ed., edited by E. Arnold.

127. J. Khedkar, A.S. Khanna, K.M. Gupta, Tribological behavior of plasma and laser coated steels, Wear 205, 220, (1997).

128. http://www.calphad.com

129. A.F. Guillermet: "The Fe-Mo (Iron-Molybdenum) System,"Bull. Alloy Phase Diagrams, 3(3), 359, (1982).

130. Andersson J.-O. – A thermodynamic evaluation of the FeMoC system, Calphad, 12 (1), 9, (1988).

BIOGRAPHICAL INFORMATION

Cristian Cionea earned a Bachelor in Mechanical Engineering at Polytechnic University in Bucharest, Romania in 1997.

In 2003 he received a Master of Science in Mechanical Engineering from Johns Hopkins University, under the supervision of Dr. Kevin Hemker.